Methods of ultra-fast laser contrast diagnostics and optimization

Max-Born-Institut
für Nichtlineare Optik
und Kurzzeitspektroskopie

Im Fachbereich Physik der Freien Universität Berlin eingereichte Dissertation

von

Nikita Khodakovskiy

ORCID: 0000-0003-1905-0887

Berlin, 2020

Erstgutachter: Prof. M.J.J. Marc Vrakking
Zweitgutachter: Prof. Dr. Eric Cormier
Tag der Disputation: 11 Februar 2020

Acknowledgement

This thesis is a result of my work during last few years and this work would be impossible without people working with me and those who supported me.

First, I want to thank my mentor Mikhail Kalashnikov for that unique experience which I got during working on PhD. I am thankful for knowledge and useful discussions on optics and physics in general. It was valuable and interesting for me to work with him in the laboratory.

I am grateful to Prof. M.J.J Marc Vrakking, for his time, patience, valuable comments and great attention to details. To Rodrigo Lopez-Martens and Laboratoire d'Optique Appliquée for productive collaboration during the work on the rotation of the polarization ellipse.

To Dr. Igor Vlasov and Dr. Elena Obraztsova for help with Raman measurements. I would like to thank Prof. Dr. Eric Cormier for the time he spent reviewing this thesis and Sergei Kühn for the help with translation of the abstract.

To Jens Glaesel for technical support. To everyone working at Max Born Institute and Forschungsverbund Berlin for professional competence and great working atmosphere. To Amplitude Technologies for experience at laser industry. Many thanks.

I gratefully acknowledge the Marie Skłodowska-Curie actions, Max Born Institute and LaserLab Europe for the funding which made this work possible.

Lastly, I thank my family and friends who helped and supported me on my way to being a scientist. I am grateful to Réka Eszter Szabó for her support during the final stage of my PhD.

Contents

Chapter 1

Introduction

1.1 Motivation

Ultra-fast lasers play an important role in the investigation of laser-matter interactions [1]. Modern, ultra-fast and high-peak power laser systems can deliver pulses with a duration of several tens of femtoseconds ($1\,\mathrm{fs} = 10^{-15}\,\mathrm{s}$) and with peak power of up to a Petawatt (peta = 10^{15}). At a lower power level, even shorter, down to few oscillations of the electro-magnetic field, optical pulses are available [2]. Current laser technologies allow ultra-short laser pulses to be converted by nonlinear processes taking place during laser-matter interaction in solids or gases into coherent pulses of attosecond ($1\,\mathrm{as} = 10^{-18}\,\mathrm{s}$) duration, or to high energy electrons, protons or ions [3, 4, 5]. These types of laser-driven sources are called secondary sources.

High peak power lasers (up to a PW level and above) are being used for investigations in the area of relativistic physics of ultra-high intensity [6, 7] and, in particular for the acceleration of particles [8]. In this way, GeV electron beams [3, 9] and proton/ion beams with energies of tens of MeV [4, 5] have been experimentally demonstrated. Moreover, the acceleration of electrons to the GeV level has been reached in an ultra-short distance of 3 cm. These results make compact table-top particle accelerators feasible.

Control of the pulse shape in the time domain is of great importance in particle accelerators using solid targets. Pre-pulses/pedestals preceding the main pulse may ionize the target surface long before the main pulse arrives and may even demolish the solid target. Different mechanisms of absorption are involved and these play important roles in techniques for particles acceleration. Light absorption, in turn, is impacted by the gradient of the density of electrons forming the plasma which is created on the surface of the solid target by the pre-pulses/pedestals preceding the main pulse. As a result, the plasma field accelerating the particles is significantly impacted for most of

the acceleration regimes. In the case of ultra-thin foils of several nanometres thickness, parasitic light creates a shock wave together with X-rays, which destroy the rear surface of the foil. This lowers the gradient of the electron density on the rear surface of the foil and decreases the energy of the accelerated protons [4, 10]. For relatively thick targets (tens of μm) the created plasma gradient may contribute positively to the ion acceleration process, because of the stronger absorption of the main pulse [11]. However, this positive impact is limited by certain parameters of the plasma and the temporal shape of the driving electromagnetic pulse also has to be strongly controlled.

Another important application of high peak power ultra-fast lasers is the generation of coherent pulses of attosecond duration in the extreme ultraviolet (XUV) and soft X-ray frequency ranges through the High-Harmonic Generation (HHG) process. In general, one can distinguish two ways to produce attosecond pulses [12]; gas high harmonics generation (GHHG), where an intense laser pulse interacts with a gas jet [13] and solid state high harmonics generation (SHHG), where the attosecond pulses are generated at the surface of a solid target illuminated by ultra-short laser pulses at high intensity [14, 15, 16]. Both techniques require precise control over the laser source parameters. However, for SHHG the temporal profile of the pulse plays a key role, determining the efficiency of the HHG process [16]. In addition, an improvement to the temporal properties of the ultra-intense pulses allows the different physical mechanisms leading to HHG to be distinguished when an optical pulse of relativistic intensity ($I\lambda_L^2 > 1.37 \times 10^{18}[\mathrm{Wcm}^{-2}\mu\mathrm{m}^2]$) interacts with a solid target [16]. The parasitic light preceding the main pulse destroys the entire process of the laser-matter interaction and dramatically decreases the efficiency of the secondary sources.

Most modern ultrafast lasers, especially ultra-high peak power ones, use the concept of Chirped Pulse Amplification (CPA), details of which are considered in section 1.4. Laser pulses in CPA systems experience many modifications during their propagation and amplification, beginning with temporal stretching and followed by amplification and re-compression back to their transform limit. Since the bandwidth of the amplified pulses is rather broad and a bandwidth-limited pulse duration at the laser exit is required, dispersion management in CPA lasers plays a key role.

In addition, in propagating through the optical elements of the laser chain, the laser pulse accumulates distortions caused by impurities in the optical media and nonlinear effects that take place during the amplification and propagation. As a result, the optical pulses generated by these ultra-fast lasers have a complicated temporal shape (the details are considered in 1.5). Some of the features appearing at the leading edge of CPA laser pulses have been previously considered in the literature and are well understood, however the temporal range of few tens of picoseconds around the pulse

peak and the intensity range below 10^{-7} of the peak intensity, are not, although this temporal and intensity region plays a very important role in laser-matter interactions.

In this thesis the quality of the temporal shape of the optical pulse (as well as that of the leading edge) is characterized by the intensity contrast, which is the ratio of the laser peak intensity I_{peak} to the intensity $I(t)$ at time t. Currently, Ti:Sapphire is the most popular material for high-power laser systems. Therefore the investigation of the temporal contrast is centered on this material. The problem of the temporal contrast of CPA lasers was identified more than fifteen years ago. Since then several techniques were developed (for a detailed analysis, see chapter 1.7) that allow this parameter to be significantly improved. Among these techniques, worthy of mention is (1) the double CPA concept (DCPA) [17] (see also 1.7.2) that allows suppression of the amplified spontaneous emission, and (2) the plasma mirror (PM) [18] that, installed at the laser exit, allows for an improvement in the temporal contrast of nearly 4 orders of magnitude. In the plasma mirror concept, the focused laser beam impacts on the surface of an anti-reflection-coated optical target and the reflected beam is used for the experiment. Since the target surface is of low reflectance, pre-pulses with an intensity that is not sufficient for ionization of the target surface experience a strong attenuation. At the moment when the intensity exceeds the ionization threshold, plasma appears on the target surface and starts to reflect the laser light. One can optimize the laser parameters to reach a high reflection efficiency and contrast improvement of close to 4 orders of magnitude simultaneously. Unfortunately, this technique leads to the destruction of the target surface, thus the number of shots available with one target is limited. As a result, this technique works well for high repetition rate laser systems with laser energy levels of around a mJ, which with a target of a reasonable size ($\sim$ 10 cm diameter) allows the system to run for several minutes. A high peak power laser with a substantially higher output energy (hundreds of mJ, or even Joules) requires the surface of the plasma mirror to be in the mm range. Taking into account the formation of debris and the deposition of ablated material on the target surface, a few mm distance between shots is necessary. In this case one can use the plasma mirror in a single shot regime only.

Despite the fact that the plasma mirror is an effective tool for improving the temporal contrast of laser pulses it has disadvantages. First, the typical efficiency does not exceed 80%, and second, there is no plasma mirror solution for laser systems that combine high peak and high average power. The latter is especially important, since current laser developments are moving towards the combination of high peak and high average power [19]. Thus, it is very important to seek a solution for the problem of the temporal contrast making the laser pulse temporally “clean” without using additional

devices, such as a plasma mirror. This requires the pulse shape be intensively investigated in the temporal range of a few tens of picoseconds around the pulse peak, and the identification of the processes that lead to pulse degradation. In fact, the currently available methods for contrast improvement (DCPA and PM) solve most of the temporal contrast problems for low energy laser systems and those running at high peak power with a low repetition rate. This is the reason that, during the last decade, practically no efforts have been made to analyse the reasons for the pulse shape degradation in the range of few tens of picoseconds around the pulse peak.

The major objective of this thesis is to fill the gap concerning the lack of information available on the processes that degrade the temporal contrast of pulses generated in Ti:Sapphire CPA lasers in the poorly investigated temporal range of few tens of picoseconds around the main pulse. The work aims to improve the understanding of these processes to the level required for a laser-matter interaction without the generation of a pre-plasma. This requires the development of diagnostics for pulse characterization in the dynamic range of intensity $\sim 10^{10}$ and the development of new methods for temporal contrast improvement.

1.1.1 Thesis organisation

The introductory chapter starts with a description of the propagation of ultra-short pulses in a homogeneous dispersive medium 1.3. This is followed by the description of major nonlinear effects such as the optical Kerr effect (1.2.1), the self-focusing (1.2.2) and self-phase modulation (1.2.3). After that the amplification in a gain medium (1.3) as well as principles of the CPA concept (1.4) and the formation of the temporal shape of laser pulses in CPA systems (1.5) are considered. Then a milli-Joule energy level Ti:Sapphire laser system used for the experiments is presented (1.6). The introductory chapter is ended with an overview of methods for temporal contrast enhancement (1.7). In particular, nonlinear filtering techniques for temporal contrast enhancement, such as the plasma mirror (1.7.1), the generation of a cross-polarized wave (1.7.2) and rotation of the polarization ellipse (1.7.3) are discussed.

The introduction is followed by four experimental chapters (2 – 5). First, the methods of the temporal contrast characterization are discussed (chapter 2). After that diagnostics for the high dynamic range characterization of re-compressed pulses are considered. It includes an experimental investigation of the reliability of the commercially available Sequoia device (2.5.1) and considers specific issues appearing in the measured temporal traces (2.5.2).

Chapter 3 is dedicated to an investigation of the temporal contrast on the picosecond time scale. It starts with a discussion about spectral clippings (3.2) which may occur in

a stretcher or a compressor and may cause degradation of the temporal contrast. Then experimental results on the comparison of different stretcher/compressor combinations are presented (3.3). This is followed by the consideration of the temporal contrast degradation in high-power cascades of Ti:Sapphire lasers (3.4).

In chapter 4 a new method of diagnostics of coherent/uncoherent parts of the pulse shape is developed and presented (4.2). This technique is used to show that the parasitic long pre-pedestal is generated from the post-pedestal lying behind the main pulse and thus the question of the pulse shape improvement in front of the main pulse is redirected to the post-pedestal (4.4). The latter is investigated in the following and a plausible theory for its nature and origin is presented (4.4.5). The analysis of the temporal contrast of a home-made 100 TW laser system is presented at the end of the chapter (4.5).

The last chapter 5 presents a method for improvement of the temporal contrast based on nonlinear rotation of the polarization ellipse (NER) in noble gases in a differentially pumped hollow core fibre. This allows the temporal contrast of a Ti:Sapphire-based front-end to be improved with internal efficiency $\sim 50\,\%$ comparable with the generation of a cross-polarized wave $\sim 25\,\%$. In addition, the method demonstrates significant spectral broadening of the output pulses. Moreover, the shape of the spectral intensity supports a high-quality post-compression with a clean temporal profile of the resulting pulses. It makes NER filtering suitable for the temporal contrast improvement of fibre- and thin-disk-based laser systems with a comparably long pulse duration of hundreds of femtoseconds.

1.2 Propagation of ultra-short pulses in homogeneous dispersive media

The propagation of a plane wave in a non-magnetic, non-conductive homogeneous dispersive medium is described by the wave equation that follows from the Maxwell equations:

$$\nabla^2 E - \frac{1}{c^2}\frac{\partial^2 E}{\partial t^2} = \frac{1}{\varepsilon_0 c^2}\frac{\partial^2 P}{\partial t^2} \tag{1.1}$$

where ε_0 is the permittivity of free space or the electric constant and $c = 1/\sqrt{\varepsilon_0 \mu_0}$ is the speed of light. The international system of units (SI) is used in this thesis unless otherwise stated. The wave is assumed to be linearly polarized and for simplicity is

described by the scalar equation (1.1). The polarization term P can be expressed as:

$$P(t) = \varepsilon_0 \chi^{(1)} E(t) + P_{NL}(t) \tag{1.2a}$$

$$P_{NL}(t) = \varepsilon_0 \chi^{(2)} E(t)^2 + \varepsilon_0 \chi^{(3)} E(t)^3 + \dots \tag{1.2b}$$

where P_{NL} refers to the nonlinear part of the polarization response to the electric field E. The parameters $\chi^{(1)}$, $\chi^{(2)}$ and $\chi^{(3)}$ are the linear susceptibility, and the second- and third-order susceptibility of the medium respectively. $E(t)$ is the electric field strength.

The propagation of an ultrashort laser pulse can be described as a plane wave $E(t, z)$ propagating in the z direction. Thus, ∇^2 in (1.1) can be replaced by $\partial^2/\partial z^2$. Considering (1.2), the wave equation (1.1) can be rewritten in the form:

$$\frac{\partial^2 E}{\partial z^2} - \frac{n^2}{c^2}\frac{\partial^2 E}{\partial t^2} = \frac{1}{\varepsilon_0 c^2}\frac{\partial^2 P_{NL}}{\partial t^2} \tag{1.3}$$

where n is the refractive index of the medium $n = \sqrt{\varepsilon}$, and ε is the dielectric permittivity of the medium.

$E(t, z)$ can be represented by its spectral components using the Fourier transformation:

$$E(t, z) = \int_{-\infty}^{\infty} E(\omega) e^{i(kz - \omega t)} \mathrm{d}\omega \tag{1.4}$$

where $E(\omega)$ is the amplitude of the electric field of the spectral component ω and $k(\omega)$ is the wave vector:

$$k(\omega) = \frac{\omega}{c}\sqrt{\varepsilon(\omega)} = \frac{\omega n(\omega)}{c} \tag{1.5}$$

In the case of negligible absorption the spectral components can be represented as:

$$\tilde{E}(\omega, z) = E(\omega) e^{ik(\omega)z} = E(\omega) e^{i\phi(\omega, z)} \tag{1.6}$$

where $\phi(\omega, z)$ is the spectral phase.

Usually, the wave equation (1.3) is solved using the Slowly Varying Envelope Approximation (SVEA) and the resulting solution to (1.3) can be found in the following form:

$$E(t, z) = A(t, z) e^{i\varphi(t, z)} + A(t, z) e^{-i\varphi(t, z)} \tag{1.7}$$

where $A(t, z)$ is a slowly varying envelope in space and time, and $\varphi(t, z) = k_0 z - \omega_0 t$ is the temporal phase.

The SVEA allows for a Taylor expansion of the wave vector k in the vicinity of the

central frequency ω_0 to be considered:

$$k(\omega) = k_0 + k_1(\omega_0) \cdot (\omega - \omega_0) + \frac{1}{2}k_2(\omega_0) \cdot (\omega - \omega_0)^2 + \frac{1}{6}k_3(\omega_0) \cdot (\omega - \omega_0)^3 + \dots \quad (1.8)$$

where

$$k_m(\omega_0) = \left(\frac{\mathrm{d}^m(\omega/c \cdot \sqrt{\varepsilon(\omega)})}{\mathrm{d}\omega^m} \right)_{\omega=\omega_0} \quad (m = 0, 1, 2, \dots) \quad (1.9)$$

Here $\phi(\omega, z) = k(\omega)z$ characterizes the spectral phase and thus the Taylor expansion of $k(\omega)$ is the Taylor expansion of the spectral phase. The k_m coefficients reflect the dispersion properties of the medium: k_1 characterizes the group velocity $v_g = 1/k_1$, k_2 characterizes the Group Velocity Dispersion (GVD), k_3 characterizes the Third Order Dispersion (TOD), etc. The m terms of the Taylor series of $k(\omega)$ determine the order of the approximation in which the ultrafast pulse propagation is considered. In the second-order approximation, only k_1 and k_2 are considered and $k_m = 0$ for m > 2.

A Gaussian shape is usually considered for the pulse envelope A of the electric field:

$$A(t) = E_0 \cdot e^{-t^2/\tau_0^2} \quad (1.10)$$

where τ_0 defines the pulse duration as the half-width at the level $1/e$ of the maximum. Figure 1.1 shows the electric field of an optical pulse at a central wavelength of $\lambda_0 = 800\,\mathrm{nm}$ and of duration $\tau_0 = 6\,\mathrm{fs}$.

If the intensity is considered, the envelope will be:

$$I(t) = E_0^2 \cdot e^{-2t^2/\tau_0^2} \quad (1.11)$$

where τ_0 is the half-width at the level $1/e^2$ of the intensity envelope.

It is also practical to define a pulse duration τ_{fwhm} of the intensity envelope as the full-width at half-maximum (FWHM):

$$\tau_{\mathrm{fwhm}} = \sqrt{2\ln 2} \cdot \tau_0 \quad (1.12)$$

In the following, the definition used will be indicated by the subscript (τ_0 or τ_{fwhm}).

The SVEA approximation can be applied only when the pulse duration is significantly longer than the period of a single optical cycle T_0 at the central frequency ω_0:

$$\tau_0 \gg T_0 = 2\pi/\omega_0 = \lambda_0 n(\omega_0)/c \quad (1.13)$$

Thus, for a Ti:Sapphire laser system ($T_{800\mathrm{nm}} \approx 2.67$ fs), the SVEA works well with $\tau_{\mathrm{fwhm}} > 25\,\mathrm{fs}$.

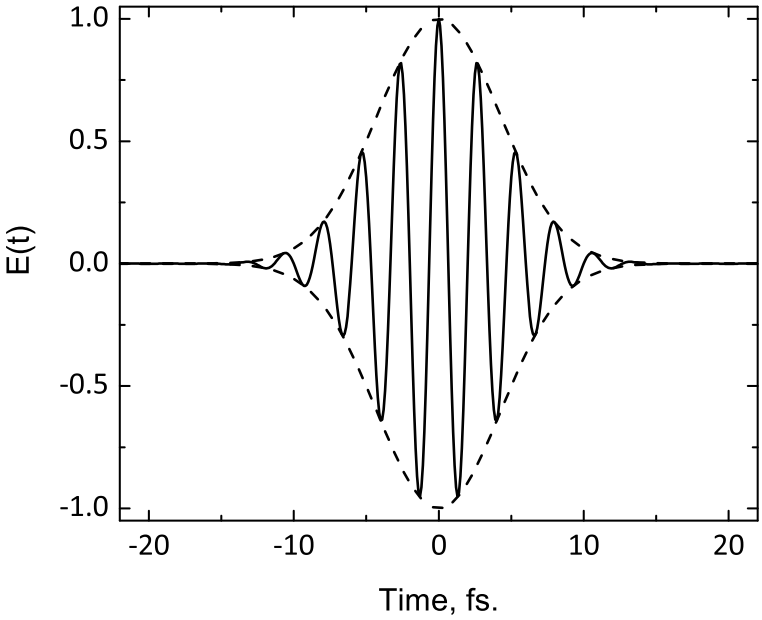

Figure 1.1: Electric field of an optical pulse (solid line) and the envelope (dashed lines) in case of $\lambda_0 = 800\,\mathrm{nm}$ $E_0 = 1$, $\tau_0 = 6\,\mathrm{fs}$

A transform-limited pulse is an optical pulse with the pulse duration defined by the reciprocal value of the spectral bandwidth. These pulses correspond to the situation when $\varphi(t) \equiv 0$. In the case of a transform-limited pulse of Gaussian shape in the time domain, the spectral envelope will also have a Gaussian shape. According to the Fourier transform:

$$I(\omega) = |E_0|^2 \cdot \exp\left(-2\frac{(\omega - \omega_0)^2}{\Delta\omega_0^2}\right) \tag{1.14}$$

where $\Delta\omega_0$ is the half-width of the spectral intensity profile at the level of $1/\mathrm{e}^2$ from the maximum. The spectral width $\Delta\omega_0$ and the temporal pulse duration τ_0 for the Gaussian shape are related as:

$$\tau_0 \cdot \Delta\omega_0 = 2 \tag{1.15}$$

Therefore, the same ratio can be expressed for the FWHM values as:

$$\tau_{\mathrm{fwhm}} \cdot \Delta\omega_{\mathrm{fwhm}} = 4\ln 2 \tag{1.16}$$

Where $\Delta\omega_{\mathrm{fwhm}}$ is defined for the intensity profile of spectrum in the frequency domain the same way as τ_{fwhm} is defined for the intensity profile in the time domain:

$$\Delta\omega_{\mathrm{fwhm}} = \sqrt{2\ln 2} \cdot \Delta\omega_0 \tag{1.17}$$

Equations (1.15) and (1.16) are only correct for a Gaussian shape of the envelope. For other shapes, the coefficient on the right-hand side of equation (1.15) has a different value.

However, it is more useful to have equation (1.16) in a form containing the spectral width in the wavelength domain. Since $\omega = 2\pi c/\lambda$, then $\Delta\omega = 2\pi c \cdot \Delta\lambda/\lambda_0^2$ and the equation for the wavelength is:

$$\tau_{\text{fwhm}} \cdot \Delta\lambda_{\text{fwhm}} = \frac{2\ln 2}{\pi c}\lambda_0^2 \tag{1.18}$$

where c is speed of light. For instance, a transform-limited pulse with $\Delta\lambda \approx 94\,\text{nm}$ at a central wavelength $\lambda_0 = 800\,\text{nm}$ corresponds to a pulse duration of $\tau_{\text{fwhm}} \approx 10\,\text{fs}$.

The spectral phase $\phi(\omega)$ plays a key role in the determination of the temporal parameters of the optical pulse. The shape of the temporal envelope significantly depends on the spectral phase and, thus, the k_m coefficients determine the envelope in the time domain. The optical elements of the laser system change the spectral phase leading to changes in the pulse duration. Minimization of k_m is required to keep the pulse duration short. Usually, it is enough to minimize k_m up to m = 4 to reach an output pulse duration of 10 – 20 fs.

Taking into account k_2 and k_3, the pulse duration in the third-order approximation can be expressed as [20]:

$$\tau = \tau_0\sqrt{1 + \left(\frac{2k_2 z}{\tau_0^2}\right)^2 + \left(\frac{\sqrt{2}k_3 z}{\tau_0^3}\right)^2} \tag{1.19}$$

where τ_0 is the half-width at the level $1/e^2$ of the intensity profile in the time domain.

1.2.1 Kerr effect

A high intensity can be reached during ultrashort pulse propagation, which leads to nonlinear effects. In particular, the refractive index starts to depend on the intensity [21]:

$$n(\lambda) = n_0(\lambda) + n_2 I(\lambda) \tag{1.20}$$

The term I in equation (1.20) is the cycle-averaged intensity of the electromagnetic field $I(\lambda) = 2n_0\varepsilon_0 c|E(\lambda)|^2$. The Kerr effect is related to the third-order optical susceptibility $\chi^{(3)}$ and described by the nonlinear polarization term:

$$P_i^{(3)}(\omega) = 3\varepsilon_0 \sum_{jkl} \chi_{ijkl}^{(3)}(\omega = \omega + \omega - \omega)E_j(\omega)E_k(\omega)E_l^*(\omega) \tag{1.21}$$

where the negative frequency is introduced through the convention $E^*(\omega) \equiv E(-\omega)$ and $\chi^{(3)}_{ijkl}$ is the fourth-rank tensor of the third-order nonlinear susceptibility which in the general case has 81 independent elements which can be nonzero. However, for media of various spatial symmetries, the number of independent elements in the tensor $\chi^{(3)}_{ijkl}$ can be significantly reduced. For isotropic media, $\chi^{(3)}_{ijkl}$ has 21 nonzero components and only 3 of them are independent:

$$\chi^{(3)}_{xxxx} = \chi^{(3)}_{xxyy} + \chi^{(3)}_{xyxy} + \chi^{(3)}_{xyyx} \tag{1.22}$$

The nonlinear refractive index can be considered as a $\omega = \omega + \omega - \omega$ process. In this case, the intrinsic permutation symmetry leads to the expression [21]:

$$\chi^{(3)}_{xxyy} = \chi^{(3)}_{xyxy} = \chi^{(3)}_{xyyx} = \frac{1}{3}\chi^{(3)}_{xxxx} \tag{1.23}$$

The n_2 coefficient can be calculated directly from the third-order nonlinear susceptibility (1.24) [21]

$$n_2[\mathrm{m}^2/\mathrm{W}] = \frac{3}{4n_0^2\varepsilon_0 c}\chi^{(3)} \approx \frac{283}{n_0^2}\chi^{(3)}[\mathrm{m}^2/\mathrm{V}^2] \tag{1.24}$$

I these expressions $\chi^{(3)}$ equals the effective third-order susceptibility $\chi^{(3)}_{\text{eff}}(\theta)$, which is a function of the medium symmetry and orientation [22]. In the case of isotropic media, $\chi^{(3)} = \chi^{(3)}_{xxxx}$.

The refractive index dependence on the light intensity was first considered in detail by Maker [23, 24]. It plays an important role in nonlinear optics as the nonlinear part of the refractive index leads to many nonlinear effects. The most valuable are the self-focusing and self-phase modulation effects which are considered in sections 1.2.2 and 1.2.3. In addition, the nonlinear part of the refractive index leads to an additional nonlinear phase shift, when intense light propagates through a medium. At high intensities, this leads to significant phase shifts and wavefront distortions.

The accumulated nonlinear phase φ_{NL} can be introduced to assess the impact of the nonlinear phase shift:

$$\varphi_{NL} = \int_0^L \gamma P(z)\mathrm{d}z \tag{1.25a}$$

$$\gamma = \frac{n_2\omega_0}{A_{\text{eff}}c} \tag{1.25b}$$

where P is the pulse power, ω_0 is the central optical frequency, c is the speed of light, L is the length of the medium, γ is the nonlinear parameter, and A_{eff} is the effective

mode area characterizing the beam size:

$$A_{\text{eff}} = \frac{\left(\int |E|^2 \mathrm{d}A\right)^2}{\int |E|^4 \mathrm{d}A} = \frac{\left(\int I \mathrm{d}A\right)^2}{\int I^2 \mathrm{d}A} \tag{1.26}$$

where E and I are the amplitude and the intensity of the electric field respectively, and A is the area of integration. For a Gaussian beam profile this can be expressed as

$$A_{\text{eff,Gaussian}} = \frac{\left(2\pi \int_0^\infty e^{-2r^2/\sigma^2} r \mathrm{d}r\right)^2}{2\pi \int_0^\infty e^{-4r^2/\sigma^2} r \mathrm{d}r} = \pi\sigma^2 \tag{1.27}$$

where σ is the beam radius at the level of $1/e^2$ of the peak intensity.

The *"breakup"*-integral parameter, known also as the B-integral [25] is often used to characterize the nonlinear phase shift caused by the nonlinear polarization term. It is equivalent to the accumulated nonlinear phase expressed in equation (1.25):

$$B = \frac{2\pi}{\lambda} \int_0^L n_2 I_0(z) dz \tag{1.28}$$

where λ is the wavelength, L is the length of the medium, and I is the peak intensity. The n_2 term in (1.28) is measured in [cm^2/W]. Values of n_2 in electrostatic units (esu) can be found in the literature and in these cases, the B-integral can be calculated using equation (1.29) [26]:

$$B = \frac{80\pi^2}{\lambda c} \int_0^L \frac{n_2 I_0(z)}{n_0} dz \tag{1.29}$$

Or, via a unit conversion:

$$n_2[\text{m}^2/\text{W}] = \frac{40\pi}{c} \frac{n_2[\text{esu}]}{n_0} \tag{1.30}$$

In both equations (1.28) and (1.29), the intensity term, I, is in units of [W/cm^2].

It is important to take into account the losses in lossy media. The attenuation of the light introduced by a medium can be calculated according to the Beer-Lambert law, expressed in the equation

$$I(\lambda) = I_0 e^{-\alpha z} \tag{1.31}$$

where α is a coefficient characterizing losses of the medium and I_0 is the input intensity.

In the case where n_2 does not depend on the coordinate z, one can substitute the

nonlinear length of interaction L by L_{eff} in equation (1.28):

$$L_{\text{eff}} = \frac{1 - e^{-\alpha L}}{\alpha} \tag{1.32}$$

1.2.2 Self-focusing

Self-focusing is one of the most important nonlinear effects in high-power laser systems. The intensity-dependent refractive index and the spatial intensity beam profile lead to a radial dependence of the refractive index. As a result, assuming the beam profile to be a smooth Gaussian function with relatively high intensity, the wavefront is distorted in a manner similar to the wavefront distortion caused by a focusing lens. In this case, the intensity-dependent refractive index leads to beam focusing. This is also called Kerr-lensing. The beam focusing increases the local intensity and leads to an even stronger focusing. The higher intensity creates a lens with a shorter focal length. This results in an optical breakdown of the medium or a filamentation regime which destroys the beam [27].

Self-focusing occurs when the peak power of the optical beam exceeds the critical power for self-focusing:

$$P > P_{cr} = \frac{\alpha \lambda_0^2}{4\pi n_0 n_2} \tag{1.33}$$

where λ_0 is the central wavelength, n_0 and n_2 are the linear and nonlinear refractive indices of the medium respectively, and α is a coefficient depending on the spatial beam profile. For a Gaussian beam shape $\alpha = 1.8962$ [28].

The spatial intensity distribution of a real laser beam is not perfect because of diffraction from the apertures of optical elements, media impurities, etc. Diffraction effects lead to a local increase of the intensity that may happen on a spatial scale of microns to millimetres. At high power this results in a local self-focusing (small-scale self-focusing) of the beam leading to a local degradation of the wavefront.

1.2.3 Self-phase modulation (SPM)

The second important nonlinear effect caused by the intensity is self-phase modulation (SPM) and this effect occurs in the temporal domain. Here, the intensity and temporal profile of the beam lead to a temporal phase distortion:

$$\varphi(t) = \omega_0 t - \frac{\omega_0}{c} n(t) L = \omega_0 t - \frac{\omega_0}{c} n_0 L - \frac{\omega_0}{c} n_2 I(t) L \tag{1.34}$$

Where L is the propagation distance. The instantaneous frequency changes according to:

$$\omega(t) = \frac{\mathrm{d}}{\mathrm{d}t}\varphi(t) = \omega_0 - \frac{\omega_0 n_2 L}{c}\frac{\mathrm{d}I(t)}{\mathrm{d}t} = \omega_0 - \frac{\mathrm{d}}{\mathrm{d}t}\varphi_{NL}(t) \tag{1.35}$$

where $\varphi_{NL}(t)$ is the nonlinear phase shift. Thus, the instantaneous frequency changes according to the first derivative of the intensity profile in the temporal domain. Assuming a positive n_2 value results in a red-shifting of the frequencies at the leading front ($\mathrm{d}I(t)/\mathrm{d}t > 0$) of the pulse while the trailing front ($\mathrm{d}I(t)/\mathrm{d}t < 0$) is blue-shifted. The red-shifting means that the spectral components have a lower frequency, while the blue-shifting corresponds to an increase in frequency. Thus, SPM leads to chirping of a transform-limited pulse. Figure 1.2 illustrates these phase changes for a Gaussian pulse.

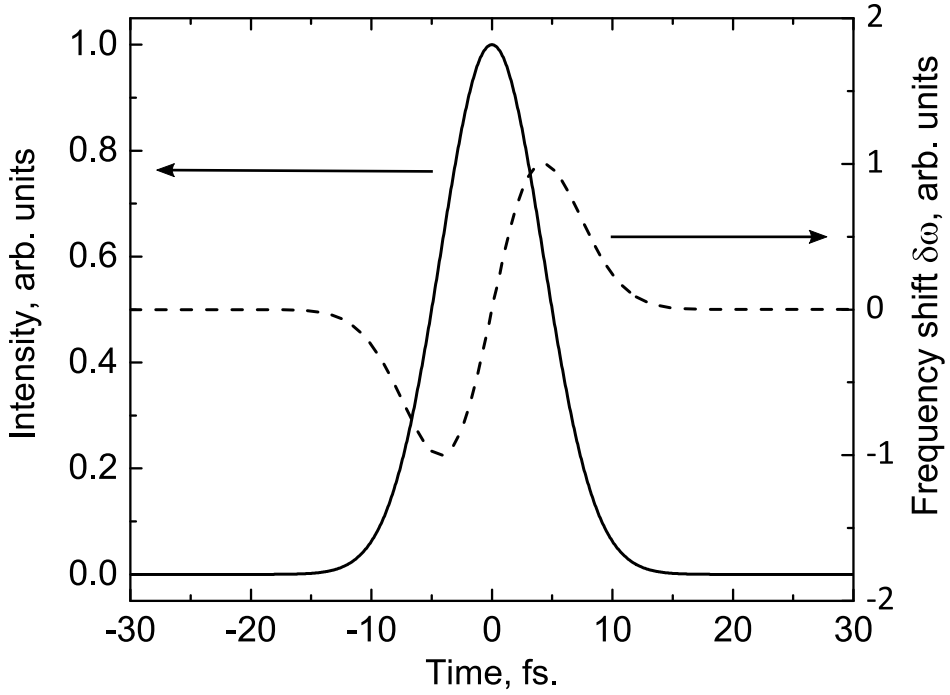

Figure 1.2: Temporal intensity profile of an optical pulse (black solid curve) and the relative frequency shift caused by SPM (dashed curve)

The maximal frequency shift caused by SPM can be estimated as:

$$\delta\omega_{\max} \propto \frac{\varphi_{NL}^{\max}}{\tau_0} \tag{1.36}$$

The duration of a transform-limited pulse is a reciprocal function of the spectral width, as previously discussed in (1.2). The spectrum broadens when the maximal frequency shift $\delta\omega_{\max}$ exceeds the spectral width of the pulse and thus, the initial transform-limited pulse is first chirped and then spectrally broadened once a certain nonlinear

phase is reached. It is worth mentioning that the pulse duration does not change due to SPM while the spectrum broadens, it instead changes due to the dispersion of the medium, as discussed in section 1.2.

1.3 Amplification of ultra-short pulses

The theory of pulse propagation in a homogeneously broadened laser gain medium with a fluorescence lifetime much longer than the pulse duration was developed by L.M. Frantz and J.S. Nodvik. They developed a formalism [29, 30] describing the amplification process in a gain medium:

$$J_{out} = J_{sat}[\ln(1 + g_0(e^{J_{in}/J_{sat}} - 1))](1 - L) \tag{1.37}$$

where J_{in} and J_{out} are the input and output fluence respectively, L represents losses, g_0 is the small signal gain obtained by one pass through the gain medium and J_{sat} is the so-called saturation fluence:

$$g_0 = e^{J_p/J_{sat}} \tag{1.38}$$

$$J_{sat}(\lambda) = \frac{hc}{\lambda_0 \sigma_g(\lambda)} \tag{1.39}$$

J_p is the fluence stored in the gain medium, λ_0 is the transition wavelength corresponding to the transition frequency $\omega_0 = 2\pi c/\lambda_0$, h is Planck's constant and $\sigma_g(\lambda)$ is the gain cross-section.

An illustration of equation (1.39) is shown in Fig. 1.3. The left side characterized by high gain is called the small-signal gain regime while the right side of the graph is the gain saturation regime. The regime of the small-signal gain is characterized by a low efficiency of the amplification while in the saturation regime of the amplification is more efficient.

The gain cross-section in Ti:Sapphire is spectrally dependent and it is shown below in Fig. 1.4. This fact, together with large gain factors, leads to spectral narrowing during amplification [30, 31]. This physical phenomenon changes the spectral shape and the pulse duration. In addition to the narrowing, the amplifying spectrum can also undergo a spectral shift, the direction and value of which depend on the initial spectrum position, the gain factor and other parameters [31, 32].

The excited active medium can also spontaneously emit light in the process of amplification and this can be considered as light noise.

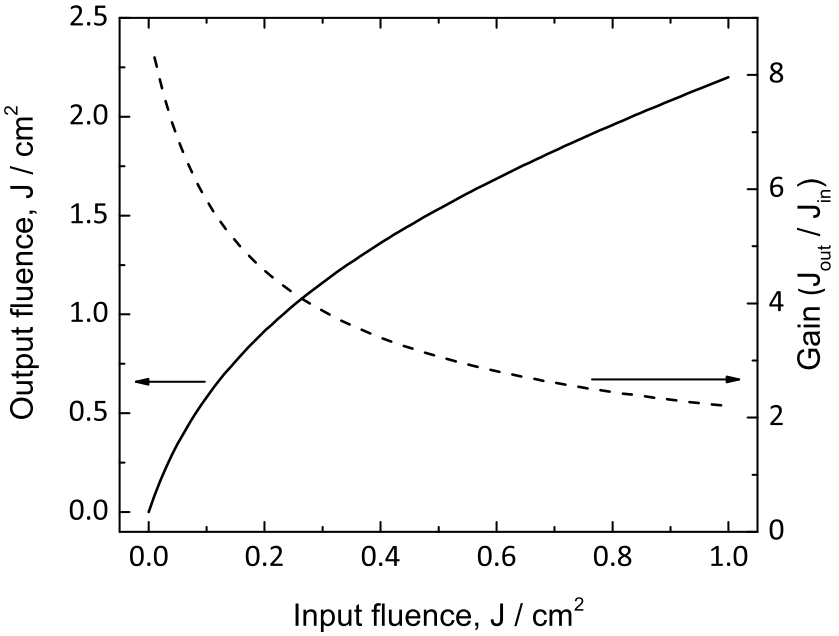

Figure 1.3: Gain saturation effect. The dependence of the output fluence on the input fluence of the seed is shown as a solid line while the corresponding gain is shown as a dashed line

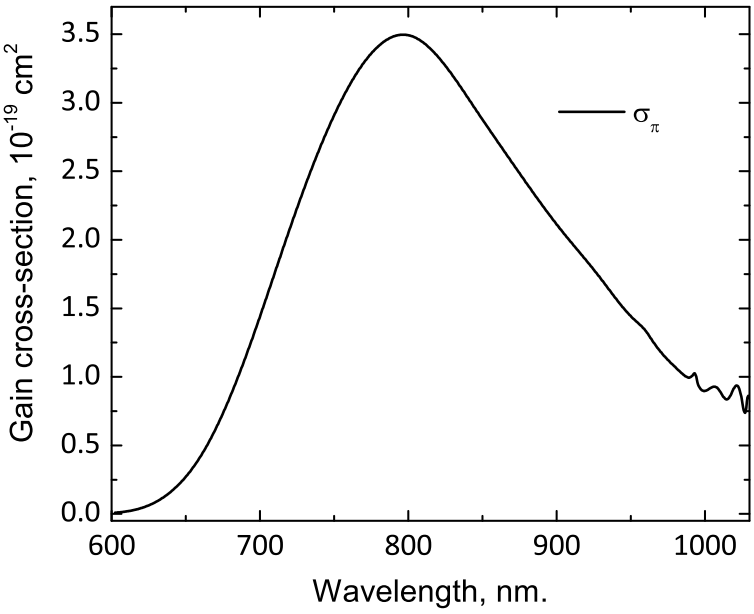

Figure 1.4: Gain cross-section of Ti:Sapphire at 300 K

1.4 Chirped pulse amplification

Chirped pulse amplification (CPA) [31] is the basic concept of modern ultra-fast lasers. It was developed in the mid-1980s [33, 34] and pushes laser systems to higher peak power. It is obvious that reaching a high peak power is preferably achieved by shortening the pulse duration, rather than by increasing the laser pulse energy. CPA was widely integrated in laser systems in the 1990s and currently enables pulses with a duration of a few oscillations.

During the amplification of short pulses, their intensity rapidly increases, reaching the level at which nonlinear effects start to become important. Amplification of beams subjected to self-focusing leads to a fast degradation of the spatial phase and intensity profile finally leading to beam destruction. The local intensity also increases, reaching the damage threshold of the optical elements used in the laser system. The CPA concept overcomes this problem by making the optical pulses longer or "stretching" them in the time domain before amplification, thus reducing the intensity and impact of the nonlinear effects during amplification. In CPA the intensity is decreased by changing the time duration of the pulse, since a change of the beam size S would change the fluence and this impacts the efficiency of the amplification (see 1.3).

$$I = \frac{E}{\tau S} \tag{1.40}$$

An optical pulse can be stretched temporally by dispersion if the initial pulse has a defined spectral phase i.e., is not chaotic/noisy. After amplification, the laser pulse can be temporally re-compressed back to close to the transform-limited duration by passing through a dispersive medium introducing dispersion of the opposite sign from that which is introduced by the stretcher. In the 1980s, it was proposed that pulses be stretched and re-compressed via a combination of two diffraction gratings [35, 36]. This technique supports compensation of the dispersion up to the third order. A simple combination of two parallel diffraction gratings makes a negatively chirped pulse where the blue part (light of higher frequency) of the pulse comes first. Adding a telescope between the diffraction gratings changes the sign of the dispersion [36]. This combination of stretcher and compressor allows the pulse to be stretched and re-compressed back to the transform limit. The telescope introduces additional losses and typically has space-dependent aberrations that impact the spectral phase, thus its aperture has to be minimized. This is why a set of diffraction gratings with a telescope, making a positive chirp, is typically used for the pulse stretching, while a set of two parallel diffraction gratings is used as the compressor.

After being stretched, the optical pulses can be safely amplified without unwanted

nonlinear processes and damage risk to the optics. The theory that was developed for Nd:glass lasers a long time ago [25] states that avoidance of the strong impact of small-scale self-focusing is possible when the accumulated B-integral does not exceed the value of ~ 1 radian [37]. Upon reaching the required energy, the pulses can be re-compressed back to their transform limit (determined by their spectral bandwidth that may be also modified during amplification). Figure 1.5 schematically demonstrates the principles of the CPA concept. In most modern laser systems, both the stretcher and compressor use diffraction gratings, although in different configurations. This technique allows for temporal stretching factors of few tens of thousands without substantial degradation of the pulse shape. Other stretcher/compressor combinations are considered in section 1.6.

It is worth noting that one of the first implementations of a full scale CPA-based laser with a stretcher/compressor configuration based only on diffraction gratings was accomplished at the Max-Born Institute [38].

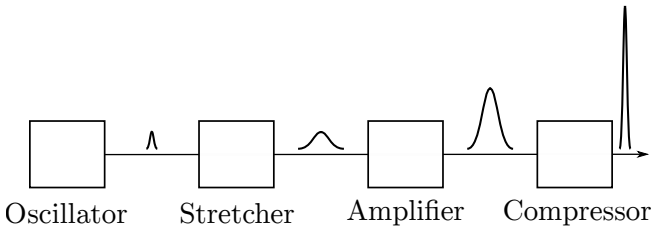

Figure 1.5: Principles of the CPA concept: an ultra-short pulse of a low energy is stretched to a longer duration in the stretcher, amplified in the amplifier and then re-compressed down to its original duration in the compressor

The CPA concept requires a laser pulse with a well-defined phase, preferably a transform-limited pulse, as the seed. In CPA laser systems, a master oscillator that delivers pulses with a duration close to the transform limit plays the role of an optical source. In a Ti:Sapphire master oscillator, the active medium undergoes population inversion as a result of energy deposition by a pump laser running typically in continuous (CW) mode. The intra-cavity modes are then amplified by stimulated emission. The cavity, formed by two or more mirrors, plays the role of positive feedback.

To reach ultra-short pulse durations, mode-locking is applied to the joint phases of the cavity eigenmodes. The constructive interference of cavity modes with joint phases form an ultra-short pulse leaking through one of the flat mirrors. Ti:Sapphire-based ultra-fast oscillators use a Kerr lens mode-locking mechanism where the mode locking is reached using the Kerr-effect and an aperture creating conditions that are favourable for ultra-short pulses.

The active medium and other optical elements of the cavity are dispersive. Their

dispersion must be compensated in order to make one round trip path equivalent for all cavity modes involved in the generation of the ultra-short pulses. Usually, a set of prisms or chirped mirrors perform this task. Figure 1.6 shows the typical scheme of a master oscillator with dispersion compensation using prisms [39].

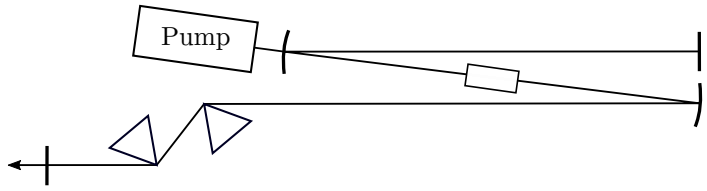

Figure 1.6: Scheme of an oscillator with prisms: a laser pump injects energy into the crystal that is located inside a cavity formed by two flat and two concave mirrors. The latter focus the cavity eigenmodes in the active medium to reach the high intensity for the Kerr effect. Two prisms compensate the dispersion of the crystal

Modern CPA systems may have different types of optical amplifiers. These can be laser-gain medium based, or Optical Parametric Amplification based. Because on the high emission cross-section of this gain medium, Ti:Sapphire lasers use multi-pass schemes of amplification where the laser pulse passes through the inverted medium several times. These are used in particular in the preliminary stages of amplification. Optical Parametric Chirped Pulse Amplification (OPCPA) [40] and Non-collinear Optical Parametric Chirped Pulse Amplification (NOPCPA) are based on parametric processes used for amplification in a collinear and non-collinear geometry, respectively.

This work only considers laser amplifiers, and in particular systems with a Ti:Sapphire active medium. Amplifiers can be split into two groups: regenerative amplifiers and multi-pass amplifiers. A typical scheme for the first type is shown in Fig. 1.7 and includes a cavity and an active medium with a pump. The seed is injected into the cavity by a Pockels cell and, after several passes through the active medium, is ejected out of the cavity. The ejection is usually accomplished by a Pockels cell. The regenerative amplifier has a closed cavity. The major advantages of this type of amplifier are its good spatial mode and energy stability. The extinction factor of Pockels cells is limited and as a result, the laser pulses amplified in the cavity "leak" through the Pockels cell, producing a train of pre-pulses preceding the main pulse. This is the major disadvantage of this type of amplifier.

A multi-pass amplifier does not have a closed cavity. Here, the spatial mode is determined by the quality of the seed and the energy distribution of the pump in the active medium. The amplified pulse passes through the inverted medium several times (up to 10 times), and multipassing can be accomplished via a set of plane mirrors (Fig. 1.8a) as well as by a small number of concave mirrors forming an open cavity, as shown

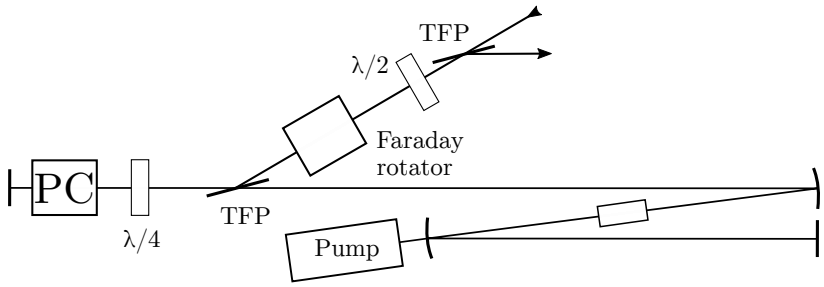

Figure 1.7: Schemes of a regenerative amplifier. The seed pulse is injected inside a cavity with a pumped active medium for the amplification and then ejected from the cavity using active and passive optical elements changing the polarization state. The focusing of the seed pulse is softer than in the case of an oscillator in order to avoid unwanted contributions from the Kerr effect

in Fig. 1.8b.

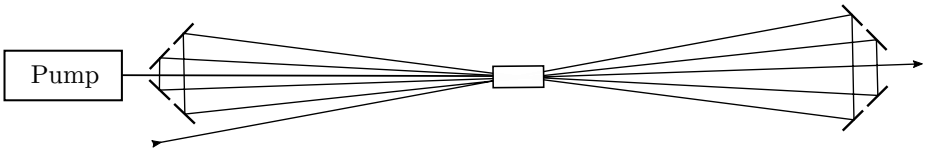

(a) "Butterfly" configuration. A collimated seed is amplified

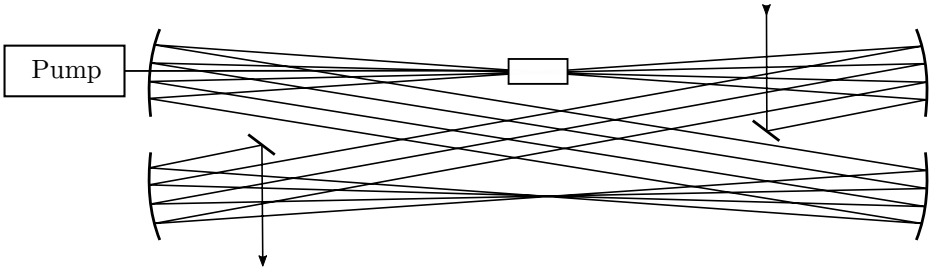

(b) Cavity-based configuration. The scheme relay images the laser beam to the crystal surface between passes. This type of design is mainly used at low energy of the seed pulse

Figure 1.8: Common schemes of multi-pass amplifiers

The amplification scheme of a typical laser consists of a successive set of amplifiers with a gradually increasing beam aperture. Power amplifiers usually use the scheme shown in Fig. 1.8a because of the large size of the seed beam while the preliminary stages use both schemes shown in Fig. 1.8.

A particular implementation of a CPA laser system used in the thesis will be further discussed in detail in section 1.6.

1.5 Temporal shape of CPA laser pulses (temporal contrast)

The focus of this thesis is the investigation of the temporal shapes of laser pulses in the vicinity of the main peak of the pulse. This can be characterized by the temporal contrast and the work thus starts with the definition of this parameter. Figure 1.9 illustrates a typical experimentally measured temporal shape of an advanced high-power Ti:Sapphire CPA laser pulse for the case where the laser system has a low ASE level (see 1.4). The presented data were obtained at a high-power laser system in Japan [41].

Two types of temporal contrast, related to energy and intensity, can be distinguished. The energy contrast is the ratio of the energy in the main peak to the energy of the preceding noise. The intensity contrast at a certain moment in time is determined by the ratio of the peak intensity of the main peak to the intensity at time t, $I_{\mathrm{pre-pulse}}(t)$ i.e. $K(t) = I_{\mathrm{peak}}/I_{\mathrm{pre-pulse}}(t)$. Thus, the intensity contrast is a time-dependent parameter, defined by the reciprocal of the intensity at the time that is considered. This work focuses on the intensity contrast and, for simplicity, this is termed the temporal contrast in the following.

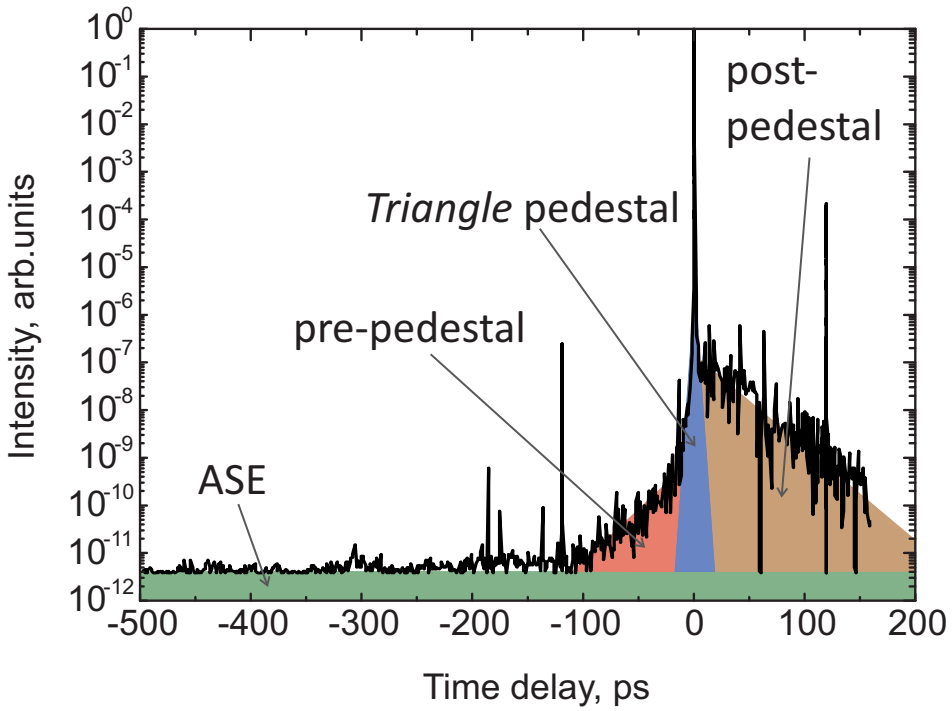

Figure 1.9: Typical temporal shape of optical pulses generated by a high-power laser system [41], presented on a logarithmic scale. The measurement shows the main pulse, amplified spontaneous emission (green), and a set of minor pulses and other pedestals (red, blue and brown) in the vicinity of the main pulse

The temporal trace shown in Fig. 1.9 is split into several parts. The ratio between the main peak maximum to the almost constant noise level forms the nanosecond contrast for $t < -200\,\text{ps}$ (green region, Fig. 1.9). This is the temporal contrast related to Amplified Spontaneous Emission (ASE). This part is well known and it will be discussed in the following section. In addition to the ASE the temporal trace shows long pre- and post- pedestals which are marked by red and brown colors, respectively. The pre-pedestal in the re-compressed pulse typically starts at around -100 ps before the main peak and the post-pedestal lasts at least a few hundreds of picoseconds. These pedestals grow to a level of $\sim 10^{-8} - 10^{-7}$ of the main pulse in its vicinity and are usually characterized by a ragged structure. These two ragged pedestals will be discussed in great detail in chapter 4. The main peak sits on a triangular pedestal (marked in blue). This feature, depending on the system, typically starts at intensity levels of $\sim 10^{-3} - 10^{-4}$ of the intensity of the main peak. The ragged and triangular pedestals are distinguished by their structures and the steepnesses of their shapes. Their origin and causes will be discussed in chapter 3. Usually, the boundary between them is clearly visible in the measured temporal trace, although the ragged pre-pedestal is not visible in some temporal traces. It is necessary to separate these parts of the leading front due to their different natures. In addition, sets of pre- and post-pulses of different peak intensities are present in a pulse shape.

The mentioned features are the scope of the current work. In some cases, filtering methods are used to improve the temporal contrast and, as a result, some of these features do not appear in the measured traces. In the case of a conventional Ti:sapphire laser that does not use special techniques to improve the temporal contrast, the ASE level is around 10^{-7}, rendering the ragged pedestals (Fig. 1.9) and some of the pre-pulses invisible. Despite playing a key role in laser-matter interactions [42, 43, 4], the above-mentioned artefacts, and especially the shape of the leading front of the re-compressed pulses, are poorly investigated and understood.

1.5.1 Amplified Spontaneous Emission (ASE)

It is well-known that an excited electron can relax to a lower energy state spontaneously or through the process of stimulated emission:

$$\frac{\partial N(t)}{\partial t} = -A_{21} N \tag{1.41}$$

where $N(t)$ is the number of electrons in the excited state of the lasing transition at time moment t, and A_{21} is the rate of spontaneous emission from the upper to the lower levels. The rate A_{21} is inversely proportional to the radiative lifetime: $A_{21} \propto \tau_{\text{rad}}^{-1}$.

Spontaneous emission in laser amplifiers is a parasitic process which occurs in a pumped active medium. In our case, spontaneous emission within the Ti:Sapphire gain medium emits radiation in all directions (4π radians) and adds noise to the amplified pulse by the light spontaneously emitted in the direction of the seed pulse propagation. Under normal conditions, the relaxation time of a Ti:Sapphire crystal is approximately $\tau_{\text{rad}} \approx 3.2\,\mu\text{s}$ at 300 K [44] and this relaxation time increases with a decreasing temperature of the crystal. Passing through the pumped active medium spontaneous emission gets amplified in the same way, as the seed. This leads to an amplified spontaneous emission (ASE) background. Usually the pump comes a bit earlier than the seed. As the result, the spontaneous emission precedes the amplified seed, overlays it and lasts longer. The spontaneous emission of a pumped medium and thus the ASE can be decreased by extracting the energy from the crystal by stimulated emission and the amplification process. ASE can be also decreased by reducing the gain, since at lower gain the added part will be lower. However, it cannot be cancelled completely, as it is a fundamental process.

The ASE forms a constant background in the time domain. The amplifier not only amplifies but also contributes to the background by adding the spontaneous emission generated by the crystal in the amplifier [45, 46]. Since the process of spontaneous emission is stochastic, the created background or pedestal is not coherent to the amplifying seed pulse.

Unfortunately, there is no theory of ASE formation in an oscillator, however the theory of ASE formation in an amplifier is intensively developing. There are several models and according to one of them [46] the ASE level introduced by an amplifier can be described by the following equations:

$$\frac{I_{\text{ASE}}}{I_{\text{pulse}}} = \frac{P_{\text{ASE}}}{P_{\text{pulse}}} = I_{\text{sat}} K_{\Delta\Omega} K_p K_{\Delta\nu} \gamma(g_0, L) \frac{\tau_{\text{pulse}}}{E_{\text{seed}}} \tag{1.42a}$$

$$\gamma(g_0, L) = \frac{\ln\left(g_0/(1-L)\right)}{g_0 - 1} \tag{1.42b}$$

I_{sat} is the saturation intensity, $\gamma(g_0, L)$ is a function describing the dependence of the ASE contrast on the small signal gain, g_0 is the small signal gain, L is the optical path length in the amplifying media, $K_{\Delta\nu}$ and K_p are the spectral and polarization acceptance respectively, $K_{\Delta\Omega}$ is the spatio-angular acceptance of the optical scheme, E_{seed} is the seed energy, and τ_{pulse} is the pulse duration.

The saturation intensity I_{sat} can be expressed as:

$$I_{\text{sat}} = \frac{hc}{\lambda(\sigma_e + \sigma_a)\tau_{\text{rad}}} \tag{1.43}$$

where σ_e and σ_a are the emission and absorption cross-sections, and τ_{rad} is the radiative lifetime of the material.

An amplifier is made of optics having a spectral selectivity and thus only a part of the emission spectrum can be transmitted and amplified in a certain implementation of an amplifier. The spectral acceptance $K_{\Delta\nu}$ is the fraction of light which can be amplified out of the total fluorescence spectrum and thus it depends on the implementation. Decrease of the spectral acceptance of the amplifier without spectral clipping of the amplified pulse leads to an ASE contrast improvement. The polarization acceptance K_p reflects the probability that the active medium emits a photon of the same polarization as the amplified light. It is obvious that this coefficient is different depending on whether the amplifier is sensitive/insensitive to the polarization state and whether the linear/complex polarization is being amplified.

The third acceptance coefficient $K_{\Delta\Omega}$ describes the spatial parameters of the amplifier.

$$K_{\Delta\Omega} = A \cdot \Delta\Omega/4\pi \tag{1.44}$$

where $\Delta\Omega$ is the acceptance solid angle, and A is the size of the pumped area. The lowest level of the ASE can be achieved if an amplifier supports the TEM_{00} mode only [46]. This corresponds to a regenerative amplifier which is based on a cavity configuration. In this type of amplifier the fluorescence acceptance is independent of the size of the pumped area

$$K^{\text{R}}_{\Delta\Omega} = \frac{\lambda^2}{4\pi} \tag{1.45}$$

The story is different when a multi-pass amplifier is used. Even when focusing optics is used, the optical scheme supports not only the TEM_{00} mode. There are a few factors which impact the spatial acceptance $K_{\Delta\Omega}$ of a multi-pass amplifier such as the geometry of the amplifier, the presence of focusing optics, the geometry of the crystal and other factors. ASE has a bigger emission angle than the seed and therefore, if the spatial mode of the pump beam is larger than the mode of the seed, ASE contributes even if it does not overlap the optical path of the seed. Since the seed extracts the energy on its optical path it is obvious to decrease the spatial mode of the pump beam down to the size of the seed beam. A good matching between the pump and the seed modes allows a minimum level of ASE to be reached in a multi-pass amplifier.

1.5.2 Requirements for the temporal contrast

Obviously, the requirements for the temporal contrast depend on the application. It is common to use laser radiation as a driver for the generation of attosecond pulses, or particles (electrons, protons, ions). The latter are called laser-driven secondary

sources. The physics involved in the secondary source determines the requirements for the primary source. For instance, the generation of attosecond pulses from the surfaces of solid targets and shooting on ultra-thin (a few nm thick) targets for the acceleration of particles demand that the primary source (the laser) delivers optical pulses with a very steep leading front which is free of substantial pre-pulses. A target irradiation before the main pulse causes a shock wave to propagate through the target and heating by X-rays can then destroy the rear surface of the foil. This impacts the electron density scale on the rear side and prevents the acceleration of the particles.

The requirements for the temporal contrast will be different for different parts of the laser pulse shape because of the significant difference in the durations and energies of the temporal features. In [47] it was shown that the temporal contrast limits for short pre-pulses are less stringent than those for ASE. An intensity level of $10^{10}\,\mathrm{W/cm^2}$ is considered as the point when ionization starts to play an important role in absorbing targets. Many secondary sources (acceleration of protons, for instance) degrade if a substantial pre-plasma appears on the target surface preceding the arrival of the main pulse. Reaching the ionization threshold may not be sufficient to produce an expending plasma because of a low energy of short pulses. The threshold for ablation or melting needs to be exceeded to create substantial plasma expanding from the target surface. Contrary to ionization, both ablation and melting processes are fluence-dependent rather than intensity-dependent. A fluence of $0.5\,\mathrm{J/cm^2}$ absorbed by a target can be considered as the threshold for ablation and melting [47]. The thresholds for ablation/melting create duration-dependent requirements for the short pre-pulses and the leading front of the main pulse. These limits for the temporal contrast are presented in Fig. 1.10. It is evident that, because of its long duration, ASE is the most important feature from the point of view of the temporal contrast.

Modern high-power laser systems can deliver an intensity of approx $\sim 10^{22}\,\mathrm{W/cm^2}$. Let us consider this case. The duration of the pre-pulses can never be shorter than the duration of the main pulse. According to Fig. 1.10 (see the green curves) if the duration of the main pulse and thus the duration of pre-pulses is longer than 30 fs, their temporal contrast must be better than 10^9. Concerning the long pre-pedestals, their duration is longer than a few picoseconds thus the contrast of these pedestals must be better than 10^{12}.

The process of high-harmonic generation in gases is limited by the ionization and the peak intensity itself. Thus, HHG in gases is not that sensitive to the temporal contrast and the parameters of existing laser systems are sufficient for this type of HHG.

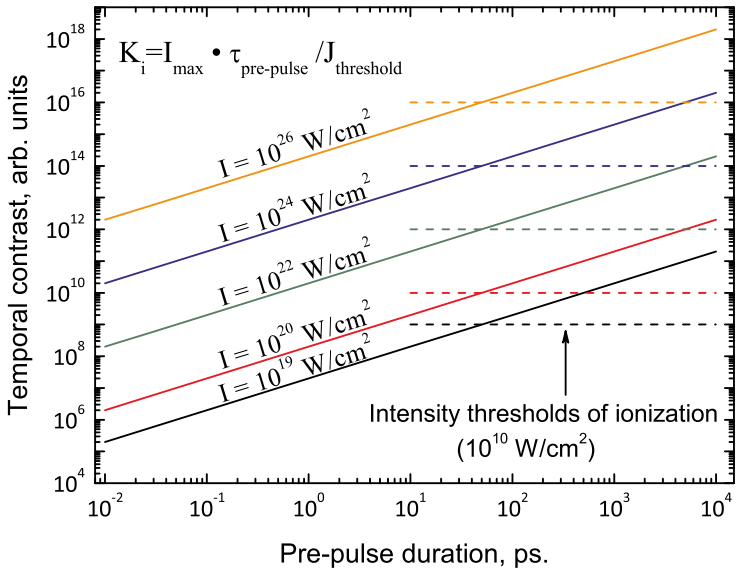

Figure 1.10: Dependence of the temporal contrast requirements on the duration of a feature in the time domain. The solid lines correspond to the threshold associated with ablation/melting (fluence $J_{th} = 0.5\,\mathrm{J/cm^2}$ [47]). The dashed lines indicate the requirements for staying below the ionization threshold (intensity $I_p = 10^{10}\,\mathrm{W/cm^2}$).

1.5.3 Design of a low ASE level Ti:Sapphire-based laser system

The initial seed beam of a master oscillator, with a very low energy level in the range of nanojoules, must be efficiently pre-amplified before entering the intermediate and power stages of amplification. There is a worldwide practice of using amplifiers where the energy of the seed pulses ($\sim$nJ) reaches the millijoule energy level. This cascade, together with the master oscillator and the stretcher, is usually called the front-end.

Ti:Sapphire amplifiers, because of the comparably high emission cross-section of the crystal, are able to reach amplification factors of up to 6 orders of magnitude in a single stage. Thus this cascade determines the major properties of the amplified beam. This is supported by the theory presented in 1.5.1 and in the literature. In particular, the front-end determines the spectral content – the bandwidth, its subsequent reduction by gain narrowing [30] and the temporal contrast in the nanosecond time range (ASE). The subsequent amplification cascades of a Petawatt laser system have a lower net gain and they run in a saturated regime of amplification [30]. They contribute to the level of ASE [46]; however, the front-end plays the most important role in the formation of the ASE level as it is the part with the highest gain.

In Ti:Sapphire CPA lasers, the stretched seed has an extremely low energy level of a

few nanojoules. It was shown in [48] that the ASE temporal contrast of re-compressed pulses in Ti:Sapphire lasers grows linearly with the seed energy injected in the amplifier. This is a result of the fact that a higher total gain is required at lower seed energy. Since the pre-amplifiers work in the high gain regime below the gain saturation, they are not very efficient and require more energy stored in the active medium. The stored energy which is not extracted by the seed contributes to the ASE. So, it is important to increase the seed energy injected into the amplifier and thus a higher output power of a master oscillator leads to higher ASE contrast assuming that the temporal contrast of the master oscillator is constant.

The efficiency of an amplifier grows and the gain decreases with the number of passes according to the Franz-Nodvik formalism (see Fig. 1.3). As a result, the energy losses of the seed during the primary passes are more detrimental for the ASE level than those during the last passes. This creates a recommendation to reduce the energy losses when the pulse energy is low.

The ASE can be shortened in time using a Pockels cell with an optical window that equals the duration of the stretched pulse $\tau_{\text{stretched}}$ plus the switching time of the Pockels cell τ_{pc}. However, the switching time of a Pockels cell is usually limited to a few nanoseconds and in extreme cases it cannot be any shorter than a few hundred picoseconds. This limits the time window of the transmission and thus other methods to reduce the ASE level must be used within this window.

1.6 Laser system for temporal contrast investigation

Most of the investigations presented in this work were performed on available experimental instruments at the Max Born Institute [17]. A low energy front-end was mainly used for the investigations since, as it was discussed in 1.5.3, this is one of the major components of a high-power laser system. In addition, a 100 TW MBI high-field laser system was also investigated to clarify how nonlinear filtering and high-power cascades of amplification may impact the temporal contrast. In this section, the front-end is discussed in detail.

So far the laser community mainly investigated the impact of amplifiers on the ASE level. However, the roles of the oscillator, stretcher and compressor in the formation of the temporal contrast are not clear. Their design can impact the picosecond contrast and the laser community just started to discover the role of a stretcher/compressor design. Unfortunately, there is no theory for the formation of the temporal contrast in these parts of a CPA system. Thus, their impact must be clarified experimentally

which can be done by a comparison of different designs of those parts of a CPA laser. Two different types of master oscillator, as well as three different stretcher/compressor configurations, were used together with a multi-pass amplifier with the aim of determining their impact on the shape of the re-compressed pulse. The principal scheme of the laser system is shown in Fig. 1.11.

The seed lasers comprise two Kerr lens mode-locked master oscillators with different dispersion compensation schemes: a commercial master oscillator (Femtolasers) with chirped mirrors [51] and a home-made oscillator employing dispersive prisms [52, 39]. The difference in the dispersion compensation may clarify the role of the coatings of chirped mirrors in determining the temporal contrast. Both oscillators deliver ultrashort pulses with a similar duration of about $\tau \approx 20\,\mathrm{fs}$.

After the master oscillator, the laser pulse is temporally stretched using one of three different stretchers. These include prisms, transmission diffraction gratings and reflection diffraction gratings. Different stretcher schemes based on different dispersive elements are needed to investigate how the stretching technology acts on the temporal contrast. The results of this comparison will be presented in section 3.3.

The first and the third stretchers are based on transmission and reflection diffraction gratings respectively. Both types of stretchers use the angular dispersion property of a diffraction grating: an incident spectral component with wavelength λ gets diffracted on the grooves of the grating resulting in several waves dispersed at angles depending on the wavelength. Each spectral component α will be diffracted with a different efficiency at a discrete number of angles corresponding to different diffraction orders. This is illustrated in Fig. 1.12.

The diffraction law is expressed by the grating equation

$$m\frac{2\pi c}{\omega} = m\lambda = d(\sin\alpha + \sin\beta) \tag{1.46}$$

where α and β are the angles of the incident and the diffracted light, λ is the wavelength of the spectral component, d is the groove spacing, also called pitch, and m is the diffraction order for which $|m\lambda/d| < 2$ correspond to the physically realizable diffraction orders. A diffraction grating is characterized by the number of grooves per mm $G = 1/d$. Fig 1.12 illustrates the diffraction for transmission (left graph) and reflective (right graph) diffraction gratings.

A polychromatic incident light results in sets of angularly distributed spectral components $\beta(\omega)$ of different orders m:

$$\beta(\omega) = \arcsin\left(\frac{2\pi cm}{\omega d} - \sin\alpha\right) \tag{1.47}$$

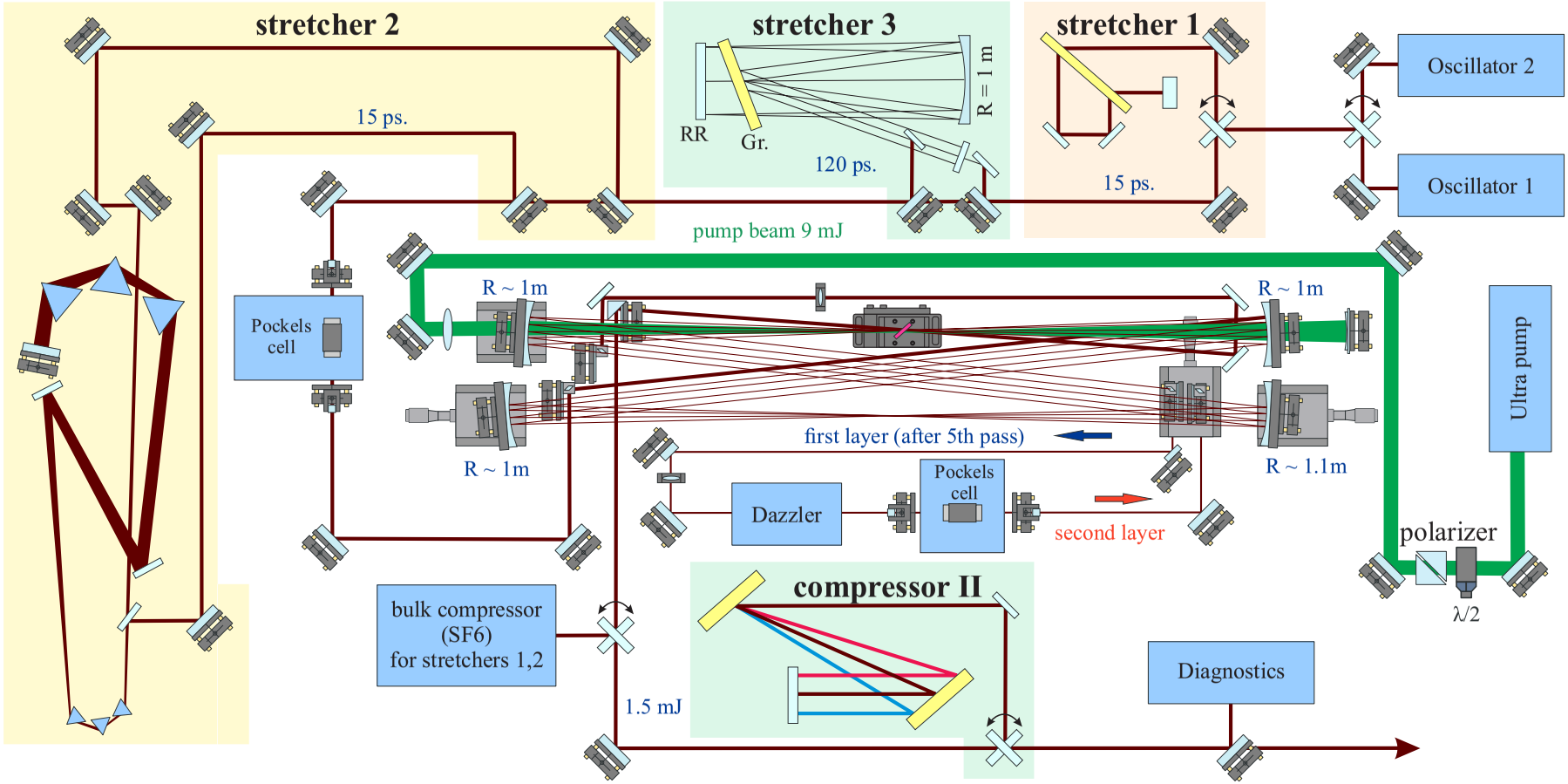

Figure 1.11: Principal scheme of the configurable front-end laser system. It consists of two master oscillators: one with chirped mirrors and one with prisms to compensate the dispersion. Stretcher 1 implements a scheme with a transmission diffraction grating. Stretcher 2 is based on the most commonly used scheme with an Offner triplet [49] and a reflection diffraction grating. Stretcher 3 is based on 6 equilateral triangular prisms. After stretching, the seed is amplified in the multi-pass amplifier with the Dazzler and re-compressed by a compressor. Compressor 1 is based on bulk glass and compressor 2 implements the commonly used Treacy-compressor [50] with two parallel diffraction gratings. Only one combination of stretcher and compressor can be simultaneously used

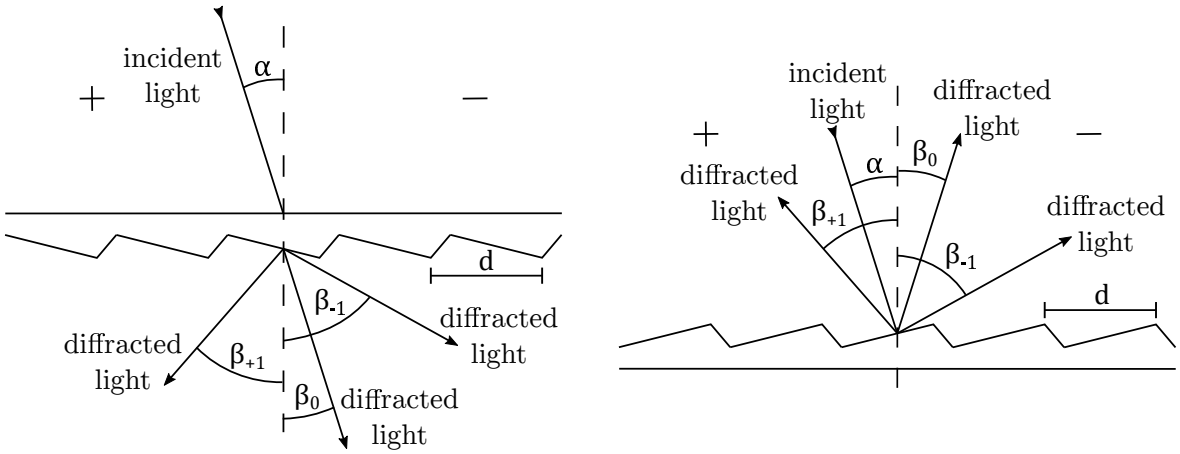

Figure 1.12: Illustration of angular dispersion of a transmission diffraction grating (left) and a reflective diffraction grating (right). The subscript indicates the diffraction order m (see equation (1.46))

When $m = 0$ the reflection diffraction grating acts as a mirror. This is called the zero order. Using equation (1.47) one can express the angular dispersion of the grating:

$$\frac{\partial\beta}{\partial\omega} = \frac{-2\pi cm}{\omega^2 d\cos\beta} = -\frac{\sin\alpha + \sin\beta}{\omega\cos\beta} \tag{1.48}$$

or

$$\frac{\partial\beta}{\partial\omega} = -\frac{2\pi cm}{\omega^2 d}\left(1 - \left(\frac{2\pi cm}{\omega d} - \sin\alpha\right)^2\right)^{-1/2} \tag{1.49}$$

The angular dispersion of the grating causes changes of the spectral phase $\phi(\omega)$. These phase changes depend on the distance after the dispersive element. Diffraction on a second diffraction grating allows the angular spectral distribution to be transformed to a spatial distribution (see Fig. 1.13b). Then, a mirror reflects the pulse for a second pass through the optical scheme. The resulting output pulse gets stretched because of the different phase shift obtained by the spectral components while propagating along a different path length.

In the experimental setup the stretcher with transmission diffraction grating uses a single diffraction grating from Wasatch Photonics with 600 grooves per mm and a size of $30 \times 60 \times 6\,\mathrm{mm}^3$. The seed beam is directed onto the diffraction grating at an angle of incidence of approximately $\alpha \approx 14°$. It is subsequently reflected by two mirrors and goes for a second pass through the diffraction grating. The length of the optical path which the beam goes through between the two diffraction passes is approximately $\approx 14.5\,\mathrm{cm}$. It is then horizontally and vertically flipped and injected back for a second pass.

One can notice that the caption of Fig. 1.13b says that a compressor is shown

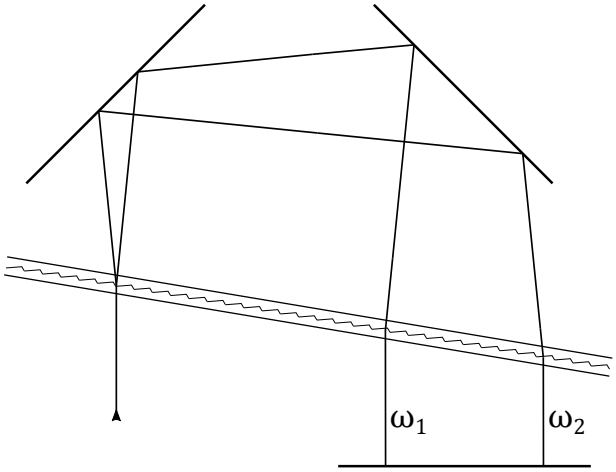

(a) A scheme of a stretcher using the angular dispersion of a transmission diffraction grating

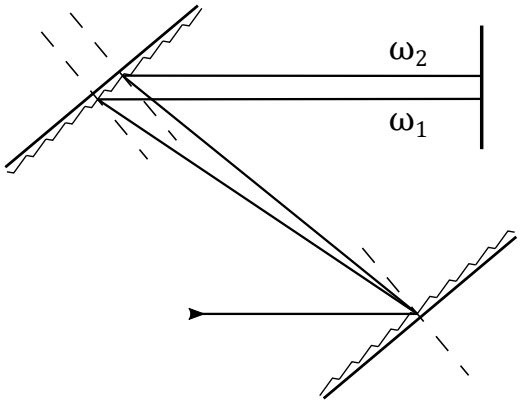

(b) Treacy compressor using the angular dispersion of a reflective diffraction grating [50]

Figure 1.13: Commonly used schemes of a stretcher with a transmission diffraction grating and the Treacy compressor with reflection diffraction grating [50]. The pulse chirp is introduced or compensated by a double pass through one of the scheme. The optical path of spectral components is different leading to temporal dispersion

instead of a stretcher. This is associated with the fact that a different scheme with a reflective diffraction grating is usually used as a stretcher. It usually includes one reflective diffraction grating and a telescope. The latter aims to invert the sign of the orders of introduced dispersion with respect to the dispersion introduced by the scheme from Fig. 1.13b. At first glance, it is not clear why a scheme with a telescope is stretching the pulse and one without the telescope is re-compressing the pulses. This is associated with the telescope, used optics and its position in the laser system. In the compressor the energy of the beam is significantly higher compared with the energy of the seed in front of the stretcher. This requires the beam to be expanded before the compressor in order to not damage the optics. A larger beam would cause higher aberrations in a telescope and makes the alignment complicated. Thus, a pair of reflective diffraction gratings is used to re-compress the pulse which was stretched using a scheme with a telescope.

A single Spectragon reflective diffraction grating with 1400.2 lines per mm is used in the configuration with the Offner triplet [49, 53] in the third stretcher. It is using the same physical principles as the stretcher with the transmission grating. In addition, this type of stretcher requires a telescope which can be a source of optical aberrations. The latter are unwanted because they introduce wavefront distortions and lead to an incomplete re-compression at the exit of the laser system. To avoid this, a modified scheme of the commonly used Offner imaging scheme is used [53]. It minimizes the

aberrations in the stretcher. The stretcher includes a spherical mirror with a radius of curvature $R \approx 100\,\text{cm}$ and a flat mirror located in its focus. The angle of incidence on the diffraction grating is $\alpha \approx 41^\circ$. A double-pass is also employed in our stretcher.

The stretcher marked as stretcher 2 in Fig. 1.11 uses prisms as the central element. A prism can be used as a dispersive optical element using refraction to split the spectral components in space [54, 55]. The refraction of a monochromatic beam is described by Snell's law

$$n_1 \sin\theta_1 = n_2 \sin\theta_2 \tag{1.50}$$

where θ_1 and θ_2 are the angles of incidence and refraction, n_1 and n_2 are the refractive indices of the corresponding media. The dispersion property of media expressed by the dependence of the refractive index on the wavelength $n(\omega)$ is well known. Refraction of broadband incident light on an interface of a dispersive medium results in an angular distribution of the spectral components ($\theta_2(\omega)$). A prism geometry and double refraction increases the difference in the angles of refraction and as a result the optical path of the spectral components. The angular dispersion of prisms is used in a way similar to the one described for diffraction gratings. A set of prisms allows ultra-short pulses to be stretched in time [56]. In addition, the material of prisms has its own dispersion and together with the different optical path of the spectral components caused by the geometry of the prism they contribute to the total dispersion. Fig. 1.14 shows a simple stretcher using two prisms.

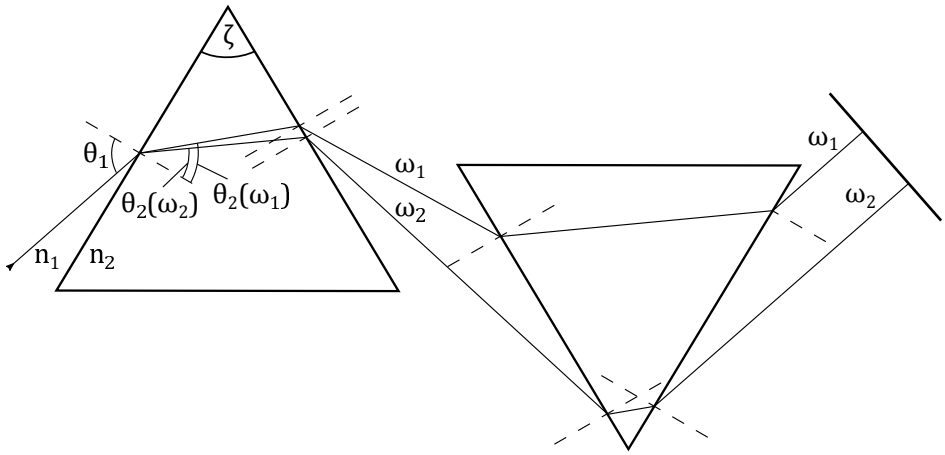

Figure 1.14: Illustration of angular dispersion of a prism with an apex angle ζ and a simple stretcher using two prisms. Light with an incident angle of θ_1 gets refracted on the interfaces of the prisms resulting in angular light dispersion $\partial\theta_2(\lambda)/\partial\omega$. The angular dispersion is used in a double prism configuration with the second prism rotated by π with respect to the first one. A double pass through the optical scheme causes stretching of the pulses

The prism-based stretcher uses six SLAL-59 OHARA glass prisms cut from one

piece of bulk glass and it is based on the dispersion of prisms [57, 55, 56]. Six equilateral triangular prisms form two groups of prisms with a gap (of approximately $\approx 187\,\text{cm}$) to increase the optical path length and, as a result, the stretching factor. The length of the edges of the triangles forming the basis of the small and large prisms is 2 and 10 cm respectively. The beam, after passing through all prisms, is flipped in the vertical direction and back reflected for a second pass through the stretcher. The complexity of a scheme of this type grows significantly with the introduced stretching factor due to the low value of the second-order dispersion delivered by glass prisms. The stretching factor can be increased by using a larger distance between the groups of prisms or increasing their number. This makes the overall scheme larger and the alignment more complicated when compared to schemes based on diffraction gratings.

It is worth mentioning, that ray tracing is often used for designing and analysing stretcher/compressor schemes. The length of the path for certain wavelengths may be derived from a simulation. The difference of the path lengths for different wavelengths delivers information about the dispersion introduced by a certain scheme [58].

Pulses of $\Delta\lambda \approx 50\,\text{nm}$ are stretched to 10 or 100 ps, depending on the stretcher. Stretchers with prisms and transmission diffraction gratings enable the same stretching factor, resulting in a $\sim 10\,\text{ps}$ pulse duration while reflective diffraction gratings support $\sim 100\,\text{ps}$ pulses. The stretched seed pulse is launched into a ten-pass amplifier.

The multi-pass amplifier [59] for the front-end was developed to have a good temporal contrast of $> 10^9$, especially in relation to the ASE, so that features that appear on a picosecond time scale are visible. This amplifier was also designed so that it would have a minimal impact on the temporal contrast. To achieve this, the spatial modes of the pump and seed are well-matched in the Ti:Sapphire crystal, and the amplifier works efficiently (at $\sim 12\,\%$) compared to similar systems. It is important to mention that the amplifier works below the saturation regime. The millijoule multi-pass amplifier is similar to the one used as the front-end of the 100 TW high-field MBI laser system [17].

A Brewster cut Ti:Sapphire crystal (Crystal Systems) with a Figure-Of-Merit(FOM) > 200 is used for the amplifier. The FOM is defined as the ratio of the absorption coefficients at the pump and lasing wavelengths. In Ti:Sapphire, Ti^{3+} ions are responsible for emission at $\lambda \approx 800\,\text{nm}$ and absorption in the green wavelength range ($\lambda \approx 532\,\text{nm}$). The absorption at the lasing wavelength is determined by Ti^{4+} atoms which are not involved in the amplification process. This absorption is unwanted because it reduces the lasing efficiency of the crystal. The FOM characterizes the ratio of these two kinds of ions and thus it reflects the performance of the laser crystal. The optical path in the crystal is $\approx 5\,\text{mm}$. The energy of the transmitted pump beam is recycled back by

a concave mirror with a focal length ≈ 50 cm. The total pump absorption amounts to ≈ 80 %. Careful mode matching of the seed and pump beams enables an ASE contrast of ∼ 10^{10} with an energy efficiency exceeding 12 % (1 mJ of output energy at 9 mJ of pump energy).

Acousto-optic programmable dispersive filters

The task to re-compress stretched pulses is challenging. Even an accurate design of the stretcher/compressor pair does not allow to compensate completely high order dispersion introduced by the stretcher and other optical elements. Modern laser systems use active optical modulators or acousto-optic tunable filters [60] which allows the pulse dispersion to be fine tuned and can provide a good re-compression.

In the present system this filter is based on diffraction of an optical wave on strain-induced changes of the refractive index because of an acoustic wave propagating in an anisotropic medium [61]. Under certain conditions, an acoustic wave propagating near collinearly with a linearly polarized optical wave induces diffraction of this optical wave into a cross-polarized optical wave.

The acousto-optic interaction is provided by the photoelastic effect and characterized as anisotropic Bragg diffraction. The diffracted cross-polarized wave is formed by the product of the optical seed and the quasi-collinearly propagating acoustic wave

$$E_2(\omega)e^{i(\omega_2 t - k_2 z)} = E_1(\omega)e^{i(\omega_1 t - k_1 z)} \otimes S(\omega)e^{i(\Omega t - K z)} \tag{1.51}$$

were E_1 and E_2 are the complex spectral amplitude of the incident and the diffracted waves respectively, ω_1, ω_2, k_1 and k_2 are the related frequencies and wave vectors. S, Ω and K are the amplitude, the frequency and the wave vector of the acoustic wave, and $\otimes$ is the convolution operator.

The energy transfer between the optical waves is only possible in the vicinity of phase-matching:

$$\omega_2 = \omega_1 + \Omega \tag{1.52a}$$

$$k_2 = k_1 + K \tag{1.52b}$$

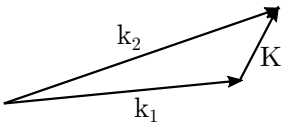

Figure 1.15: Phase matching conditions for the acousto-optic interaction

Changing the frequency of the acoustic wave one can choose with high accuracy the frequency of the diffracted light. This physical principle can be used to create a tunable filter [60]. One can generate an acoustic wave with the amplitude and frequency varying in time. While propagating in a photoelastic medium the wave creates a diffraction grating with spatially varying parameters. The frequencies of the stretched incident light

diffracts on the corresponding parts of this diffraction grating forming a diffracted cross-polarized wave with changed dispersion. In other words, the programmable acoustic wave propagating in a photoelastic medium allows the dispersion of the incident light to be changed [62, 63, 64].

The Dazzler [62, 64] and Mazzler [65] are commercially available acousto-optic programmable dispersive filters (AO-PDF) based in these physical principles. Their difference is dictated by their applications. The Dazzler is designed for single pass filtering aiming to shape the spectral amplitude and phase of the filtered wave while the Mazzler is designed to be used in multi-pass regenerative amplifiers.

Let us now get back to the laser system. According to the goal of minimizing losses at the low energy of the seed, the Dazzler and the second Pockels cell are located in the middle of the optical path (after 5 passes) of the amplifier. This is an optimal position for the Dazzler to support a good temporal contrast with comfortable operational parameters. In this position, the energy of the pulses is not very low but at the same time not high enough to cause optical damage to the crystal inside the Dazzler.

The pulse, after exiting the amplifier, is re-compressed by four passes through a $\approx 10\,\text{cm}$ thick SF6 glass block for the prism-based or the transmission grating-based stretchers. The glass-based compressor uses the dispersion of a material:

$$\phi(\omega) = \frac{\omega}{c} n(\omega) L \tag{1.53}$$

where L is the optical path in the material and $n(\omega)$ is the refractive index usually known from the Sellmeier formula.

To minimize accumulation of the nonlinear phase due to the high pulse intensity and long path in the glass, the beam diameter is increased up to 4 cm. This is also done to obtain a good temporal contrast. The impact of the accumulated nonlinear phase will be discussed in section 4.2. For the reflective grating-based stretcher, the same gratings (1400.2 grooves per mm, Spectrogon) have to be used in the Treacy compressor [50] shown in Fig. 1.11. It is formed by two parallel reflective diffraction gratings and a back reflector. Grating parallelism in the compressor was aligned to an accuracy of 0.001 degrees using electronic encoders. All stretcher/compressor configurations enabled pulse re-compression close to the Fourier transform limit of $\tau \approx 25\,\text{fs}$.

The compressor compensates for the dispersion introduced by the stretcher. This is a challenging task, even when using the Dazzler [62, 64] and Mazzler [65]. These devices allow the dispersion to be compensated up to 4 orders and are mainly used to cover the difference in dispersion introduced by all parts of the laser system.

The difference in the optical paths among the three schemes is minimized. The switching between stretcher/compressor combinations takes a minimum of time, at

approximately a half an hour. Different optical elements in the stretchers and compressors lead to their different efficiencies in term of energy, which are manifested in the transmission coefficient of the stretcher. With the same seed energy of the master oscillator, a slightly different amplification factor is then required to reach the same output energy. The bulk glass in the compressor is anti-reflection coated on both sides and as a result its losses are minimal. The compressor with two diffraction gratings incurs $\sim 40\,\%$ losses. In all cases, the energy after the re-compression was kept at a level of approximately 0.5-1 mJ to fit the requirements of the cross-correlators used for the pulse characterization.

Only broadband dielectric mirrors (Layertec # 101287, $\sim 200\,\mathrm{nm}$) and protected silver mirrors (Thorlabs) were used in the laser system to exclude possible spectral clipping and the impact of different optical coatings. The system delivers optical pulses of approximately $\Delta\lambda_{\mathrm{fwhm}} \approx 35\,\mathrm{nm}$ spectral bandwidth.

Both compressors and the stretchers with prisms and the reflective diffraction grating were designed together with a colleague from the Max Born Institute and the optical schemes were implemented by the author of this thesis.

1.7 Methods for temporal contrast enhancement

The problem of temporal contrast of ultra-short laser pulses was initially identified more than fifteen years ago. One of the joint European projects (LaserLab JRA, SHARP [66]) was especially dedicated to the characterization and improvement of temporal contrast. To this end, several new technologies were developed. In this section I am going to discuss the major filtering techniques which are widely used. In particular, I am going to describe the Double chirped pulse amplification concept (DCPA) [17] (1.7.2), and methods for nonlinear pulse filtering such as Cross-polarized Waveform Generation (XPW) [67] (see 1.7.2), nonlinear rotation of the polarization ellipse (NER) (1.7.3) and plasma mirrors (1.7.1).

Before starting with those techniques it is worth mentioning the temporal contrast filtering using a saturable absorber [68]. A saturable absorber material can be used to reduce the duration of an ASE pedestal. Since ASE arrives much earlier than the main pulse, the saturable absorber absorbs the ASE and gets transparent when the main pulse arrives. This simple method allows the ASE pedestal to be shortened.

1.7.1 Plasma mirror (PM)

A neutral plasma is a gas of free electrons and ions which is characterized by the electron density parameter n_e. The critical density, where the plasma frequency equals

the frequency of the incident light is n_c:

$$n_c = m_e \varepsilon_0 \omega_0^2 / e^2 \tag{1.54}$$

where m_e and e are the electron mass and charge, ε is the vacuum dielectric constant and ω_0 is the laser frequency. When the electron density n_e exceeds n_c, the plasma changes its optical properties and becomes reflective for light. This principle is the basis of the plasma mirror technique for temporal contrast improvement [69, 70].

The technique uses transparent targets with an anti-reflection coating on the front surface. The reflectivity of the coated target defines the improvement of the temporal contrast. Low intense light preceding an ultra-short pulse goes through such a target with minimal reflections, however, when a certain intensity is reached on the leading edge of the pulse, the target becomes ionized and switches on its reflectivity for the intense part of the pulse. The ionization process can be considered to be instantaneous on the femtosecond scale. Thus, the plasma mirror, changes its reflectivity almost immediately while interacting with intense optical pulse. The plasma expands with a speed that does not exceed 10^7 cm/s. Assuming that the expansion time of the created plasma is much longer than the optical pulse duration, the plasma mirror conserves its properties for the most intense part of the laser pulse. Thus, the main peak is reflected from the plasma mirror.

For Ti:Sapphire-based lasers with a pulse duration of $\tau < 100$ fs, this technology requires a fluence of about $50\,\mathrm{J/cm^2}$ [69, 18]. Depending on the temporal contrast and the pulse energy requirements, two plasma mirrors can be used [71]. This technique requires high fluence, thus it is usually applied at the laser exit and directly in front of the beam injection into the delivery system.

The main trends in the current development of high peak power laser systems are the shortening of the pulse duration and increase of the repetition rate. Plasma mirrors can suppress the level of practically all features preceding the main pulse by 3-4 orders of magnitude. They work well in a single shot regime but there is currently no reliable implementation of plasma mirror filtering technology for high peak power systems working at high repetition rates (> 1 Hz). An implementation of the plasma mirror technology for PW level laser systems may encounter issues due to the pulse intensity. In particular, it is necessary to increase the area where the plasma mirror is formed because of the requirements of the fluence. The plasma parameters are mainly determined by the parameters of the driving pulse and the spatial plasma parameters are strongly linked to the spatial beam and wavefront. Thus, it might be difficult to provide the required flatness and homogeneity of the plasma mirror surface for a large diameter, which for multi-PW laser systems can reach 1 cm. This potentially creates

a large problem to which cancelling of the sources of the parasitic light in the laser system may be a good solution.

1.7.2 Cross-polarized wave generation (XPW)

The generation of a cross-polarized wave (XPW) is a widely used method for temporal filtering of short pulses [67] required for subtraction of the ASE pedestal. Cross-polarized wave generation is a particular case of a degenerate four-wave mixing process (1.55), which arises from the third-order optical nonlinearity in solid crystals and is described by $\chi^{(3)}$.

$$\omega^{(\perp)} = \omega^{(\parallel)} + \omega^{(\parallel)} - \omega^{(\parallel)} \tag{1.55}$$

Since it is a third-order nonlinear process, it is described by the nonlinear optical polarization $P^{(3)}(\omega)$ (1.21). As was mentioned above the tensor of the third-order susceptibility has three independent coefficients $\chi^{(3)}_{xxyy}$, $\chi^{(3)}_{xyxy}$ and $\chi^{(3)}_{xyyx}$ (1.22). Since the frequencies are degenerate ($\omega^{(\perp)} = \omega^{(\parallel)}$), frequencies permutation symmetry dictates that $\chi^{(3)}_{xyyx} = \chi^{(3)}_{xyxy}$ [72]. Let us introduce an anisotropy coefficient of the tensor $\chi^{(3)}$:

$$\sigma = \frac{\chi^{(3)}_{xxxx} - 2\chi^{(3)}_{xyyx} - \chi^{(3)}_{xxyy}}{\chi^{(3)}_{xxxx}} \tag{1.56}$$

The coupled wave equations describing third-order nonlinear processes in the SVEA and plane-wave approximations for cubic crystals for the orthogonal field components $E_x = A$ and $E_y = B$ can be expressed as:

$$\frac{\mathrm{d}A}{\mathrm{d}z} = i\gamma_1|A|^2A - i\gamma_2\left(|B|^2B - A^2B^* - 2|A|^2B\right) + i\gamma_3\left(2|B|^2A + B^2A^*\right) \tag{1.57a}$$

$$\frac{\mathrm{d}B}{\mathrm{d}z} = i\gamma_1|B|^2B + i\gamma_2\left(|A|^2A - B^2A^* - 2|B|^2A\right) + i\gamma_3\left(2|A|^2B + A^2B^*\right) \tag{1.57b}$$

where

$$\gamma_1 = \gamma_0[1-(\sigma/2)\sin^2(2\beta)] \tag{1.58a}$$

$$\gamma_2 = -\gamma_0(\sigma/4)\sin(4\beta) \tag{1.58b}$$

$$\gamma_3 = \gamma_0(\sigma/2)\sin^2(2\beta) + \frac{1-\sigma}{3} \tag{1.58c}$$

$$\gamma_0 = \frac{3\pi}{4\lambda n}\chi^{(3)}_{xxxx} \tag{1.58d}$$

where β is the angle between the input polarization and the [100] axis of the crystal [73]. The z axis is along the [001] axis of the crystal.

The $i\gamma_2|A|^2A$ term in (1.57b) is responsible for the generation of the cross-polarized

wave, the $i\gamma_2|B|^2B$ term in (1.57a) determines the depletion of the initial beam, the $i\gamma_1|A|^2A$ term is responsible for self-phase modulation of the seed beam, and $i\gamma_3 2|B|^2A$ and $i\gamma_3 2|B|^2A$ describe the cross-phase modulation. The XPW process (1.55) is possible only in media with an anisotropy of the third-order susceptibility tensor $\chi^{(3)}$ [74]. Thus, crystals of a specific symmetry ($\sigma \neq 0$), such as cubic ($m3m$) or tetragonal ($4/mmm$) crystals are needed.

To get an analytic solution and understand the effect, the equations (1.57) must be simplified, which can be done by neglecting the depletion of the seed, the SPM of the B wave, and other nonlinear effects such as the cross-phase modulation, and assuming $|B| \ll |A|$. The neglect is fair for low efficiency of the XPW process. This simplifies the equations to

$$\frac{\mathrm{d}A}{\mathrm{d}z} = i\gamma_1|A|^2A \tag{1.59a}$$

$$\frac{\mathrm{d}B}{\mathrm{d}z} = i\gamma_2|A|^2A \tag{1.59b}$$

The solution of the (1.59) is:

$$A = A_0 e^{-i\gamma_1 A_0^2 L} \tag{1.60a}$$

$$B = A_0(\gamma_2/\gamma_1)\left[e^{-i\gamma_1 A_0^2 L} - 1\right] \tag{1.60b}$$

$\gamma_1 A_0^2 L$ is simply the nonlinear phase φ_A^{NL} accumulated by the seed wave A. For cubic crystals, the efficiency can be expressed [73] as:

$$\eta = \left|\frac{B}{A}\right|^2 = 4\left(\frac{\gamma_2}{\gamma_1}\right)^2 \sin^2(\varphi_A^{NL}/2) \tag{1.61}$$

One can see from (1.58b) and (1.61) that the efficiency depends on the anisotropy σ of $\chi^{(3)}$ and the maximum of the efficiency at high intensity corresponds to the case when $\varphi_A^{NL} = \pi$ and $\beta = \pi/8$ (22.5°). In addition, B-integral has to be accumulated in the XPW crystal. In general, according to (1.57), the energy transfer processes work in both directions and the energy of the XPW signal can be transferred back to the initial pulse. This limits the maximal efficiency of the XPW process.

Various crystals such as CaF_2, BaF_2, YVO_4, GaAs can be used for the XPW process. However, the barium fluoride (BaF_2) cubic crystal has the highest value of the anisotropy σ of the $\chi^{(3)}$ tensor. Thus, it allows to reach a higher efficiency, which is usually about 25 %.

Experimentally, the crystal is located in a telescope providing the required intensity to accumulate the B-integral in the crystal. Two crossed polarizers are used to select

the XPW signal. Since the resulting photon is a combination of three seed photons,

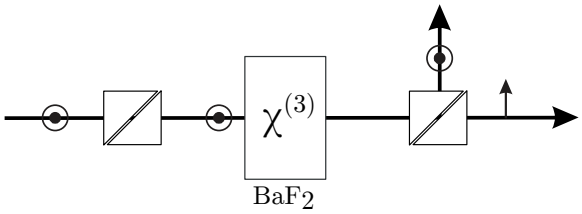

Figure 1.16: Principles of the temporal filtering for contrast improvement based on XPW mechanism. The linearity of the polarization of the input beam is verified by the input polarizer. Then, XPW wave with the orthogonal polarization is generated in the nonlinear crystal. The second polarizer blocks the residual part of the input beam and transmit the XPW pulse which are characterized by improved temporal contrast

the output temporal contrast or temporal shape will be the seeds temporal shape to the third power. On the other hand, the transmitted and XPW waves are separated by polarizers, which limits the maximum achievable contrast improvement. The extinction coefficient of the crossed polarizers defines the highest temporal filtering ratio that is possible, and the suppression coefficient of the temporal artefacts, such as the ASE and others. For commercially available polarizers this usually does not exceed 10^4.

The major advantage of the XPW process is that it conserves the wavelength of the seed wave. The method has also a positive side effect – in case of a transform limited duration of the seed pulse, the XPW pulse is $\sqrt{3}$ times shorter than the seed [75]. In addition the high intensity in the crystal leads to the SPM broadening which can easily reach a factor of 2-3, supporting substantially shorter pulses as the seed.

Application of the XPW filtering technique is deeply linked with the Double Chirped Pulse Amplification (DCPA) concept [76]. The idea of DCPA is the implementation of intermediate re-compression of the optical pulses after a pre-amplification CPA stage, followed by nonlinear filtering of the most intense part of the re-compressed pulse [17]. This allows for subtraction of the ASE background and seeds an already temporally *"clean"* laser pulse into the following CPA laser system. The second stretching of the pulse occurs together with its amplification in power cascades, with subsequent re-compression. Thus, a high-power system appears to be split into two CPA stage with a nonlinear temporal filtering stage between them.

A large stretching factor must be applied in the second CPA stage due to the high energies and, thus, high intensity in the power cascades. To support this large stretching, a scheme based on reflective diffraction gratings is required. The stretcher in this case (in particular the damage threshold of the diffraction gratings) limits the input pulse energy to a few millijoules and, as a result, sets an upper limit for the XPW energy range. Typically, this nonlinear filtering technique cleans ultra-short pulses of

a millijoule or hundreds of μJ.

A combination of the DCPA and XPW techniques represents a practical solution for the elimination of ASE and supports an ASE contrast of 10^{11}-10^{12} even at a PW power level [76]. An additional plasma mirror at the end of the laser system can reduce the ASE level by an additional 3-4 orders of magnitude.

1.7.3 Nonlinear rotation of polarization ellipse (NER)

The nonlinear temporal filtering technique based on the nonlinear rotation of the polarization ellipse has been intensively investigated in the past [77, 78, 79, 80, 81] and the physics of the process is well-known [21, 82]. The physical process of NER is based on the optical Kerr effect.

Let us start with a description of the polarization state. An elliptical polarization can be considered as a linear combination of two counter-rotating circularly polarized waves E_- and E_+ [21, 83] (see Fig. 1.17)

$$\mathbf{E} = E_+\sigma_+ + E_-\sigma_- \tag{1.62}$$

$$\sigma_\pm = (\mathbf{x} \pm i\mathbf{y})/\sqrt{2} \tag{1.63}$$

where σ_- and σ_+ correspond to left-hand and right-hand circular polarization unit vectors respectively, and E_+ and E_- are the amplitudes of these circular components, $\mathbf{x}$ and $\mathbf{y}$ are Cartesian coordinates. Thus, if $E_- = 0$ we get right-hand circularly polarized light, if $E_+ = E_-$ the light is linearly polarized and when $E_+ \neq E_-$, the light is elliptically polarized.

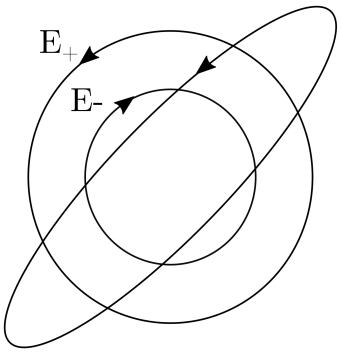

Figure 1.17: Elliptical polarization viewed as a combination of two counter-rotating circular waves

The nonlinear polarization induced by these components of the electric field in an isotropic medium with only an instantaneous electronic response ($\chi^{(3)} = \chi^{(3)}_{xxxx} = 3\chi^{(3)}_{xxyy} = 3\chi^{(3)}_{xyyx} = 3\chi^{(3)}_{xyxy}$) can be also represented through two components [21]:

$$\mathbf{P_{NL}} = P_+\sigma_+ + P_-\sigma_- \tag{1.64a}$$

$$P_\pm = \varepsilon_0 2\chi^{(3)}(|E_\pm|^2 + 2|E_\mp|^2)E_\pm = \varepsilon_0\chi^{NL}_+(E_+, E_-)E_\pm \tag{1.64b}$$

where $\chi^{NL}_+(E_+, E_-)$ and $\chi^{NL}_-(E_+, E_-)$ correspond to the effective nonlinear susceptibilities which depend on the amplitudes of the electric fields E_+ and E_-. Introducing the nonlinear polarization term from (1.64) into the wave equation equation (1.3) one

can obtain wave equations for the two counter-rotating circularly polarized waves:

$$\nabla^2 E_{\pm}(z,t) = \frac{\varepsilon + \chi_{\pm}^{NL}(E_+, E_-)}{c^2} \frac{\partial^2 E_{\pm}(z,t)}{\partial t^2} \tag{1.65}$$

where ε is the permittivity of a medium. Solving the wave equations (1.65) in the form of plane waves (1.66a) we get that their phase velocities $v_{p\pm} = c/n_{\pm}$ depend on the ratio between the amplitudes $E_{\pm}$.

$$\mathbf{E}(z) = A_+ e^{in_+\omega z/c}\sigma_+ + A_- e^{in_-\omega z/c}\sigma_- \tag{1.66a}$$

$$n_{\pm}^2 = n_0^2 + 2\chi^{(3)}(|E_{\pm}|^2 + 2|E_{\mp}|^2) \tag{1.66b}$$

where $n_0 = \sqrt{\varepsilon}$ is the linear refractive index of the medium. In the case of an elliptical polarization $E_+ \neq E_-$ the contribution of both components to the optical Kerr effect will not be equivalent. As a result, the refractive indices for the E_+ and E_- components and thus the phase velocities are different. Equation (1.66a) can be rewritten in the form:

$$\mathbf{E}(z) = \left(A_+ e^{i\theta}\sigma_+ + A_- e^{-i\theta}\sigma_-\right) e^{ik_m z} \tag{1.67}$$

where $k_m = \frac{1}{2}(n_+ + n_-)\omega/c$ is the mean propagation constant and $\theta = \frac{1}{2}(n_+ - n_-)\omega z/c$. Equation (1.67) describes a wave with the same ellipticity as the initial one (1.62) but rotated through an angle θ. In other words, the elliptical polarization rotates without a change of the ellipticity.

The expression (1.66b) can be rewritten in the form:

$$n_{\pm}^2 = n_0^2 \left(1 + \frac{2\chi^{(3)}}{n_0^2}(|E_{\pm}|^2 + 2|E_{\mp}|^2)\right) \tag{1.68}$$

and thus

$$n_{\pm} \simeq n_0 + \frac{2\chi^{(3)}}{2n_0}(|E_{\pm}|^2 + 2|E_{\mp}|^2) \tag{1.69}$$

Taking into account the equation (1.69) and replacing $\omega = 2\pi c/\lambda$, one can express the rotation angle θ:

$$\theta = \frac{\chi^{(3)}}{2n_0}(|E_-|^2 - |E_+|^2)\frac{2\pi}{\lambda} z \tag{1.70}$$

Let us now replace the term $|E_{\pm}|$ by parameters, that are understandable in an experiment. Elliptically polarized light can be obtained by passing a linearly polarized light through a quarter waveplate. The angle γ between the fast axis of the quarter waveplate and the plane of the light polarization determines the ellipticity of the polarization. The amplitudes $|E_{\pm}|$ of the circular components can also be expressed through the angle γ. Let us assume a linearly polarized wave with an amplitude of the

electric field E and a polarization in the plane formed by the x-axis and the propagation direction perpendicular to the x and y axis. The quarter-wave plate at the angle γ transforms the linear polarization into an elliptical one with semi-axes E_a and E_b

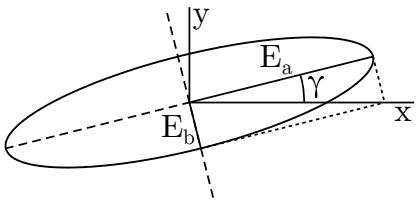

Figure 1.18: Elliptical polarization obtained from a linear polarization, using a quarter waveplate aligned at an angle γ between the fast axis and the linear polarization of the seed

$$E_a = E\cos\gamma \tag{1.71a}$$

$$E_b = E\sin\gamma \tag{1.71b}$$

For simplicity, let us limit the angle γ by the range $[0, \pi/4]$ in order to ensure that $E_a \geq E_b$. Then, one can write

$$E_a = (E_+ + E_-)/\sqrt{2} \tag{1.72a}$$

$$E_b = (E_+ - E_-)/\sqrt{2} \tag{1.72b}$$

Combining (1.71) and (1.72) one can obtain

$$|E_+|^2 = \frac{1}{2}|E|^2\sin(2\gamma) \tag{1.73a}$$

$$|E_-|^2 = -\frac{1}{2}|E|^2\sin(2\gamma) \tag{1.73b}$$

Using this equation, one can express the rotation angle θ

$$\theta = -\frac{\chi^{(3)}}{2n_0}|E|^2\sin(2\gamma)\frac{2\pi}{\lambda}z \tag{1.74}$$

Taking into account that $n_2 = 3\chi^{(3)}/(4n_0^2\varepsilon_0 c)$ and $I = 2n_0\varepsilon_0 c|E|^2$ we get

$$n_2 I = \frac{3\chi^{(3)}}{2n_0}|E|^2 \tag{1.75}$$

and thus

$$\theta = -\frac{1}{3}\cdot\frac{2\pi}{\lambda}n_2 I z\cdot\sin(2\gamma) = -\frac{1}{3}B(\lambda, I)\sin(2\gamma) \tag{1.76}$$

where $B(\lambda, I)$ is the value of the accumulated B-integral.

Principle of temporal filtering based on rotation of the polarization ellipse

In the NER, the nonlinear temporal filtering occurs between two crossed polarizers. The first polarizer makes the polarization highly linear and the second polarizer blocks the beam. Two $\lambda/4$ waveplates are placed between the polarizers. The first $\lambda/4$ waveplate is aligned at an angle γ to define the ellipticity: $\gamma = 0$ corresponds to an

unchanged linear polarization, whereas $\gamma = \pm\pi/4$ correspond to the case of right-hand and left-hand circular polarization.

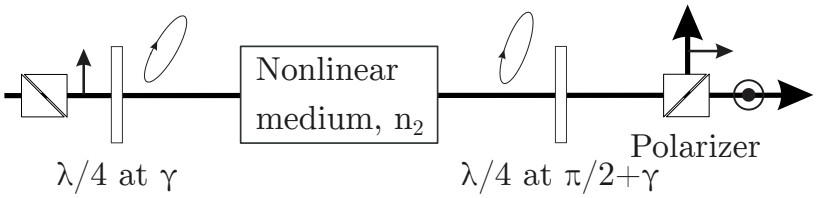

Figure 1.19: Principle of nonlinear temporal filtering based on rotation of the polarization ellipse. The first quarter waveplate transforms the linear polarization of the input beam into an elliptical polarization which at low pulse intensity is transformed back into linear polarization by the second quarter waveplate which is crossed with respect to the first one. In case of high intensity and a nonlinear medium between the plates, a polarization rotation will occur resulting in an uncompensated ellipticity at the second waveplate and thus a leak through the polarizer. The input beam must be highly linearly polarized as in the case of XPW

At low intensity this ellipticity is turned back to linear by the second waveplate. When a high intensity is reached in the main pulse, the elliptical polarization between the quarter waveplates is rotated according to the mechanism described above. The accumulated B-integral and the ellipticity of the polarization determine the rotation angle. Since the polarization is rotated at high intensity, the second quarter waveplate does not turn the polarization back to linear. After the second quarter waveplate the rotated intense part of the light will have a polarization component orthogonal to the initial linear polarization. This allows to select the most intense part of the laser pulse using the second polarizer which is crossed to the one at the input.

The efficiency of temporal filtering using NER can be obtained from the geometry for the case of flat-top temporal and spatial shapes of the pulse and can be expressed as[1]

$$\eta = \sin^2\theta \cos^2(2\gamma) \tag{1.77}$$

where θ is the rotation angle of the polarization and γ is the angle between the plane of the polarization of the seed and the fast axis of the first quarter waveplate. However, the real beam has a Gaussian pulse shape. This must be taken into account and can be done using a calculation of the weighted arithmetic mean of the efficiency. In addition,

[1] see appendix A

the B-integral also depends on the intensity. As a result, one gets

$$\eta(\gamma,\tau,B)=\frac{\cos^2(2\gamma)\int\limits_{-\infty}^{\infty}\sin^2(1/3\cdot B_{peak}e^{-2t^2/\tau^2}\sin(2\gamma))e^{-2t^2/\tau^2}\mathrm{d}t}{\int\limits_{-\infty}^{\infty}e^{-2t^2/\tau^2}\mathrm{d}t} \tag{1.78}$$

where B_{peak} is the B-integral accumulated at the peak intensity. Similar manipulations are required to take into account the spatial intensity distribution of the beam which depends on the exact implementation of the filtering scheme. Equation (1.78) was derived in a collaboration with colleagues from Laboratoire d'Optique Appliquée (LOA) located in Palaiseau, France.

Experimental results as well as a practical implementation of NER in a hollow-core fibre will be presented in the chapter 5.

Chapter 2

Diagnostics of the temporal contrast of ultrashort pulses

2.1 Introduction

In the chapter 1 we have learned that the temporal contrast is important and that there are modern techniques for its enhancement. However the existing techniques are limited and further improvement of the temporal contrast requires investigation of reasons of its degradation.

Before doing the investigation of the temporal contrast it is worth to review the available techniques for temporal contrast characterization. It is also important to ensure that the available characterization tools are reliable enough for our investigation. In this chapter I am going to talk about techniques for characterization and analysis of the temporal contrast. In particular, the rough characterization with a photodiode, and the working principles of Wizzler and high-dynamic cross-correlators will be considered. This is followed by a detailed description and an investigation of the reliability of the commercially available Sequoia cross-correlator. I will show that this device is not reliable and suggest a modification of the optical scheme in order to make it reliable for high-dynamic range characterization.

2.2 Characterization using a photodiode

There are a few techniques available for the characterization of temporal contrast. The simplest technique uses a conventional photodiode with a temporal resolution of about $\sim 1\,\mathrm{ns}$ and a set of calibrated neutral-density (ND) filters. The main peak is integrated by the diode which in fact measures its energy rather than its intensity. The duration of the ASE is much longer than the temporal resolution of the photodiode

($\sim$ 1 ns). Saturating the photodiode with the main pulse in most cases makes the ASE visible. On the other hand, adding a set of calibrated ND filters makes the main pulse visible. Assuming that the pulse re-compression is perfect, the ratio of $E_{\text{pulse}} \times F/E_{ASE} \times T_{PD}/T_{\text{pulse}}$ gives an estimate of the ASE intensity contrast. Here E_{ASE} and E_{pulse} are integrated oscillograms of the ASE and the main pulse, F is the attenuation of the ND filters, T_{PD} is the time resolution of the photodiode, and T_{pulse} is the duration of the re-compressed pulse.

This technique is simple and works well [48] but it does not provide reliable information about the detailed temporal shape of the ultra-short light pulses, especially in the vicinity of the main peak. The characterization using a photodiode is usually used to identify pre-pulses on the nanosecond time scale. The following characterization techniques work mainly on the picosecond and femtosecond timescale and do not allow the temporal contrast on tens of nanoseconds to be characterized.

2.3 Wizzler

There are also various interferometric techniques which provide information about the light intensity as well as the temporal and spectral phases. Here I will focus on a high-dynamic version of interferometric characterization implemented in the commercially available Wizzler device [84, 85, 86] and in its high-dynamic range version, Wizzler HD [87], from Fastlite. Both devices are similar and use the same physical principles. This type of device is useful for re-compression as it gives information about the phase of the re-compressed pulses and can be used as a feedback for an acousto-optic modulator such as Dazzler in order to compensate high-order dispersion.

Wizzler diagnostics is based on self-referenced interferometry [84]. The beam to be measured is split and XPW filtering is applied in one arm. This is done to obtain a reference pulse with a short pulse duration and a clean temporal profile when compared with the second arm. As a result we get two beams: $E(t)$ and $E_{\text{ref}}(t) \sim |E(t)|^2 E(t)$. These two fields can be represented in the spectral domain as $E(\omega)$ and $E_{\text{ref}}(\omega)$. One of the beams is delayed and combined with the second one. The resulting interference pattern is measured by a spectrometer. One can write the expression of the measured spectral density

$$S(\omega) = |E_{\text{ref}}(\omega) + E(\omega)e^{i\omega\tau}|^2 = |E_{\text{ref}}(\omega)|^2 + |E(\omega)|^2 + f(\omega)e^{i\omega\tau} + f^*(\omega)e^{-i\omega\tau} \quad (2.1)$$

where τ is the delay between the two beams and $f(\omega) = E_{\text{ref}}(\omega)E^*(\omega)$. After that, the

inverse Fourier transformation is applied to get the representation in the time domain

$$F.T.^{-1}[S](t) = E^*_{\mathrm{ref}}(-t) \otimes E_{\mathrm{ref}}(t) + E^*(-t) \otimes E(t) + f(t-\tau) + f^*(-t-\tau) \quad (2.2)$$

The first two terms are related to the autocorrelation functions of the two beams and thus centered around zero, while the functions f and f^* are centered at around $t = \tau$ and $t = -\tau$. Thus, in case of large τ the latter will not overlap with the autocorrelation functions and can be numerically extracted. One need to take only f or f^* because they are identical, so let us choose f. Calculating the Fourier transformation from the function $f(t-\tau)$ we get the resulting function $g(\omega, \tau) = f(\omega)e^{i\omega\tau}$ with the argument corresponding to the difference of the phases of the reference and pulse to be measured:

$$\arg[g(\omega,\tau)] = \phi_{\mathrm{ref}}(\omega) - \phi(\omega) + \omega\tau \quad (2.3a)$$

$$|g(\omega,\tau)| = |E_{\mathrm{ref}}(\omega)||E(\omega)| \quad (2.3b)$$

The phase of the reference pulse is unknown, however it can be assumed and then an iterative numerical method can be applied. In case of a near to transform-limited seed pulse, the spectrum of the XPW pulse is $\sqrt{3}$ times broader than the spectrum of the input pulse and the linear chirp is 9 times smaller [75, 86]. This is correct for pulses with $\phi^{(2)} \ll \tau^2_{0,\mathrm{fwhm}}/3$ where $\phi^{(2)}$ is responsible for the linear chirp: $\phi^{(2)} = \partial^2\phi(\omega)/\partial\omega^2\big|_0$. Thus, in this case, the temporal phase ϕ_{ref} can be neglected and the phase of the pulse to be measured can be directly derived from (2.3a). The spectral intensity is usually derived from a separately measured spectrum of the input beam.

To increase the accuracy of the characterization, an iterative method is applied in the Wizzler software. At the first iteration, the XPW phase ϕ_{ref} is neglected and $\phi(\omega)$ is derived. Since we know the relation of the seed signal and its XPW signal, the obtained phase $\phi(\omega)$ can be used to calculate the reference phase ϕ_{ref}. It is then used at the second iteration to derive $\phi(\omega)$ more precisely using equation (2.3a). A few iterations allows the phase to be derived with a good accuracy.

The dynamic range of the Wizzler is determined by the optical scheme and the measurement electronics (camera or line sensor) of the spectrometer. Unfortunately, the dynamic range of the conventional Wizzler does not exceed 4-5 orders of magnitude. In [87], which presents an implementation of the high dynamic Wizzler system, the high dynamic range phase information is extracted in a single shot. The Wizzler HD shows a dynamic range of up to 8 orders of magnitude in the single-shot regime and allows the temporal shape to be characterized with a femtosecond temporal resolution. This is a good achievement, taking into account the opportunity to derive the phase information,

which cannot be provided by correlators. In addition, the characterized temporal range is limited to 10 picosecond in the vicinity of the main pulse and it does not allow the temporal contrast outside of this range to be characterized.

The temporal contrast in the temporal range from -10 to 10 ps of the available high peak power laser systems does not usually exceed 8-9 orders of magnitude and taking into account the high temporal resolution of the Wizzler HD, it can be a perfect tool to characterize the temporal contrast in the vicinity of the main peak.

2.4 Cross-correlators

However, there is another characterization technique which allows measuring the cross-correlation function [88, 89, 90, 91, 92]. In general, the cross-correlation function can be expressed as:

$$I_{CC}(\tau) = \int_{-\infty}^{\infty} R(t)I(t-\tau)\mathrm{d}t \tag{2.4}$$

where $R(t)$ is a reference signal and $I(t-\tau)$ is the signal to be measured. Today, it is common to characterize pulse contrast using a cross-correlator.

There are several types of these devices and the first one to be considered is a self-referencing one using the second harmonic of the fundamental as the reference, i.e. $R(t) = I^2(t)$. This is a third-order cross-correlator measuring the sum-frequency [91, 92] of the signal and the frequency-doubled signal. It is assumed that the frequency-doubled pulse is shorter and its temporal profile is substantially cleaner than the incoming pulse, thus it can be used as a reference signal. Technically, the frequency-doubled signal is mixed with the fundamental and the third harmonic is analysed as a function of the relative delay between the fundamental and the second harmonic. Since the cross-correlation function $I_{CC}(\tau)$ is asymmetric this measurement delivers information about both, the leading and trailing slopes of the measured laser pulse. However, since the frequency-doubled signal still contains all the temporal artefacts of the measured pulse (pre-/post-pulses), artificial ghost artefacts can appear in the measured temporal trace. The details of this are considered later in 4.2. It is important to note that third-order cross-correlators do not deliver information about the temporal phase.

Another type of a high-dynamic range cross-correlator uses a reference beam from another source $R = I_R(t)$ with a different wavelength. Both signals are mixed to generate the sum frequency or the difference frequency in a second-order process in a nonlinear crystal [90]. With this technique one can shift the resulting correlation signal to the visible range which allows this type of device to be used for characterization pulses in the blue and UV ranges.

It is worth mentioning the opportunities for single-shot characterization using cross-correlators [93, 94, 95]. However, the dynamic range of such devices is lower than that of scanning type third-order cross-correlators. The latter are commercially available and despite the lack of information about the temporal phase, they are widely used for high-dynamic range characterization of ultra-short pulses.

Modern third-order cross-correlators provide an incredible opportunity to characterize laser pulses with energies close to a mJ at a high dynamic range of up to 10^{13}. When laser pulses are measured over such an extreme intensity range, the diagnostics itself has to be checked to ensure that it does not introduce artefacts that could be misinterpreted as components of the real pulse shape.

2.5 Sequoia cross-correlator

There are several commercial cross-correlators available on the market. The commercial Sequoia cross-correlator provided by Amplitude Technologies [91] is one of the most widely used and reliable cross-correlators for the characterization of the temporal contrast of ultra-short pulses. The temporal resolution of this device is about 100-200 fs. A modified version of the conventional Sequoia cross-correlator is mainly used in this thesis. Hence, it is important to ensure that it is reliable enough for the investigation of the temporal contrast. In this section I am going to talk about the reliability of Sequoia and those details which must be taken into account when the measured Sequoia traces are analysed. I will discuss in detail the optical scheme of the conventional Sequoia and then, in section 2.5.3, I will discuss questions related tot he dynamic range of the Sequoia.

There are a few generations of the Sequoia device. In both of them the sum frequency signal generated in a non-collinear configuration is analyzed. The conventional Sequoia uses an unfocused beam for this purpose whereas the new generation of this device – Sequoia HD has a proprietary focusing scheme inside. We will see that this detail can be crucial.

2.5.1 Aperture effect in Sequoia cross-correlator

It has been experimentally found during the pulse characterization, that the fronts of the main pulse in the temporal trace measured using the Sequoia depend on the size of a flexible aperture located in front of the bulk compressor. The flexible aperture is aligned coaxially with the laser beam, leading to radial clipping of the spatial intensity profile. Cross-correlation traces with and without spatial clipping are shown in Fig. 2.1a. There is a strong dependence of the leading front below 5 ps on the diameter of

an aperture placed in front of the bulk compressor. A similar effect was achieved when the flexible aperture is located in front of the Sequoia. However, since the beam size is smaller there, it was more difficult to observe.

A similar experiment was carried out with orthogonally oriented slits in front of the compressor (Fig. 2.1b). The leading front of the main pulse in the measured traces was only sensitive to the vertically oriented slit, i.e. the vertical spatial clipping of the beam.

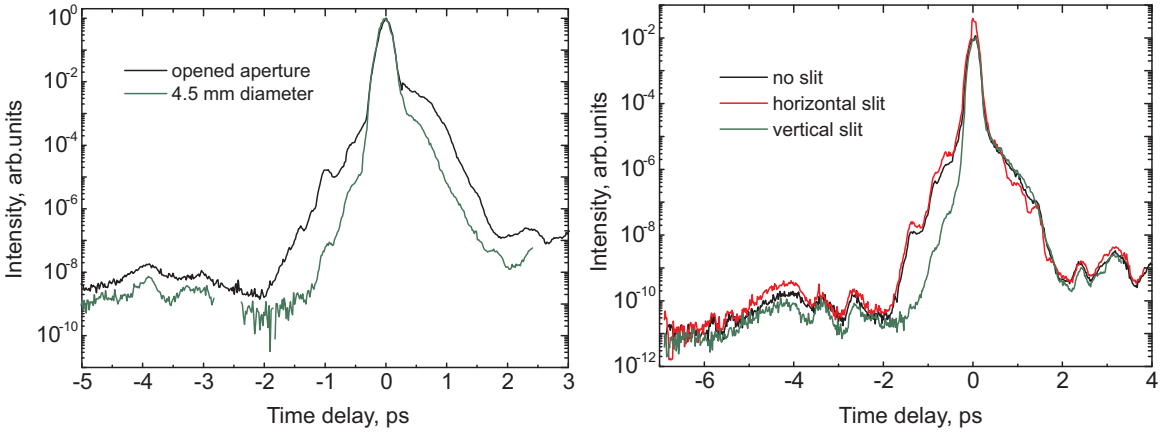

(a) Cross-correlation trace with an unclipped beam (black curve) and with the beam clipped using a flexible aperture (green curve)

(b) Cross-correlation trace measured with an unclipped beam (black curve), the beam clipped using a vertically oriented slit (green curve) and with a horizontally oriented slit (red curve)

Figure 2.1: Cross-correlation traces measured when clipping the spatial mode of the beam in front of the compressor. This figure shows that the measured temporal trace depends on the input beam profile

Despite the fact that Sequoia device has its own optical scheme, it has to be considered as a black box which is supposed to deliver accurate information about the temporal parameters of the input pulses when the measurements are performed according to the user manual [96]. The user manual does not mention the fact that the shape of the measured traces depends on the spatial beam profile. Hence, the dependence of the temporal profile on the spatial beam profile can indicate that the Sequoia is an unrealiable characterization tool. On the other hand one can assume that the pulse has different temporal contrasts in the orthogonal directions and it strongly depends on the radius of the beam. Before concluding anything about the Sequoia device, it is important to ensure that the beam has the same temporal contrast in the orthogonal directions. A beam rotation about the propagation axis was employed for this purpose by using a home-made rotator [97] designed and built by colleagues from Max Born Institute. Its scheme is shown in Fig. 2.2 and it allows rotating the beam

along the propagation axis.

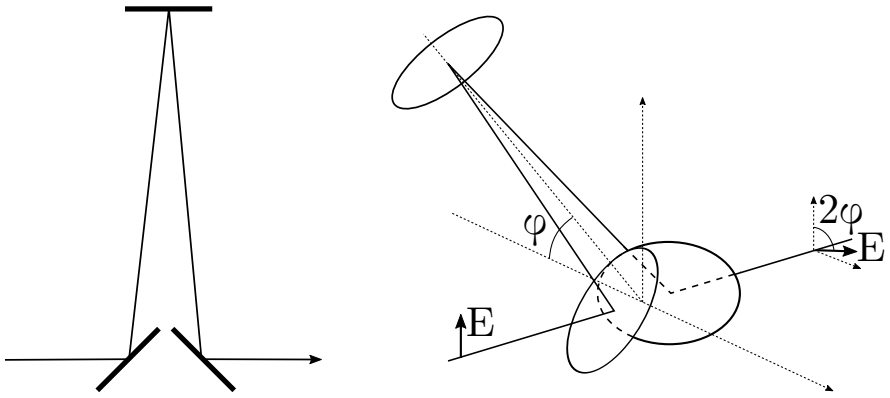

(a) 2D view (b) 3D view

Figure 2.2: Principle optical scheme for the beam rotator [97] for rotating the beam along to its propagation axis. The rotator aligned at the angle φ leads to a beam rotation angle of 2φ

Since we rotate the beam, the polarization of light is also rotated which, in turn, can impact the following propagation of the pulse and lead to wrong characterization. Thus compensation of the polarization rotation is necessary and it was implemented using an achromatic $\lambda/2$ waveplate. This was followed by a vertical slit which was inserted into the beam in front of the compressor, as in the previous experiment. The rotation angle was gradually increased from 0°(corresponding to point 1 in Fig. 2.3) to 90°(corresponding to point 9 in Fig. 2.3) with an approximate step of $\approx 11°$. If the laser beam has a different temporal contrast in the vertical and horizontal directions, the leading front of the main pulse should significantly depend on the rotation angle.

Fig. 2.3 shows that the leading front of the main pulse does not depend on the rotation angle. However, we observe differences in the trailing front of the main pulse. This fact does not mean that the temporal shape depends on the rotation angle and this phenomenon will be explained later in the section 4.3.

The observed difference of the signal level in front of and behind the pulse is a result of the measurements being taken at different alignment conditions. An *"active"* or a non-fixed optical element slightly changes the beam alignment, especially the position and angle of the beam. Taking into account the fact that the distance that the beam travels in the compressor is a few metres, as well as the sensitivity of the Sequoia to the beam position, it can be assumed that this is the reason for the observed difference of the noise level.

A similar experiment was performed with the aperture shifted from the axis of the laser beam in order to characterize the temporal contrast not in the center of the beam but on its edge, and shows that the temporal contrast does not depend on

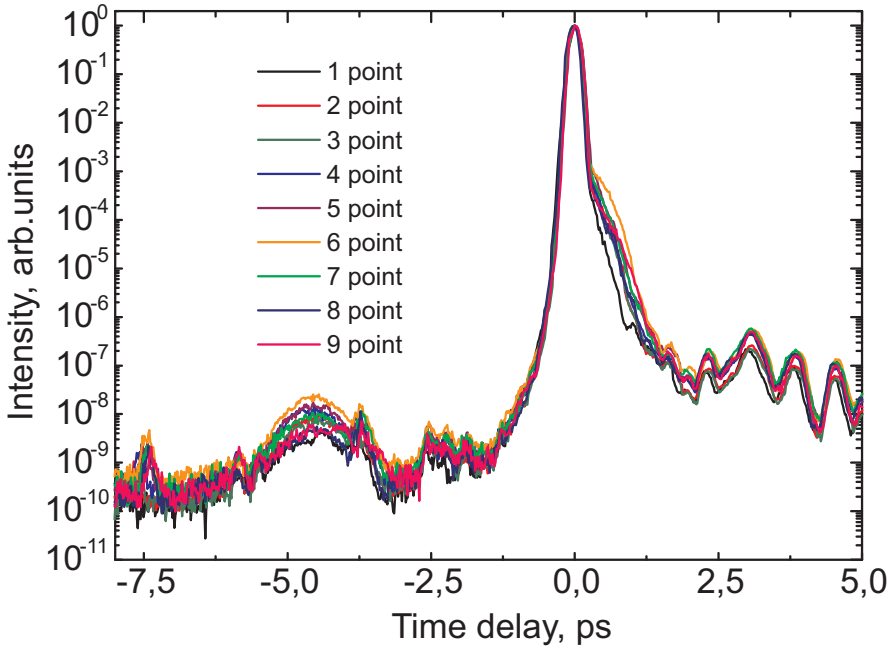

Figure 2.3: Cross-correlation traces obtained at different angle of the laser beam rotation. Different colors correspond to a different rotation angle

the radial coordinate. This experiment yields the same result. Both results indicate that the measured beam has no difference in temporal contrast depending on spatial coordinate. This result confirms the proposition that the observed effect is an issue of the conventional Sequoia. Moreover, the presented result means that the Sequoia is not reliable because the measured temporal profile depends on the spatial parameters of the input beam.

In order to identify the reason of this issue one must consider the principle of the conventional Sequoia instrument which is shown in Fig. 2.4a. The input beam is attenuated by a set of neutral density filters and then split into two parts. The second harmonic (SH) is generated in one arm and used as a reference beam. The nonlinear character of the interaction results in a SH pulse that is shorter and temporally more "clean" than the input pulse. Thus it can serve as a reference beam. The two beams, the fundamental and the second harmonic, meet non-collinearly in a second nonlinear crystal to generate a sum-frequency wave (see Fig. 2.4c). The resulting wave has the frequency of the third harmonic (TH) of the fundamental beam. The relative delay between the fundamental and the SH in the TH crystal is controllably scanned using a motorized linear stage in the SH arm. The third-harmonic signal, generated in a non-collinear interaction, is measured by a photomultiplier (PMT) as a function of the time delay. The gain of the photomultiplier can be controlled by the applied high-voltage. Changing the latter allows a dynamic range of 10^4 to be covered. A set of neutral density filters at the Sequoia input is used in addition. The combination of

attenuation and tuning the photomultiplier allows for approximately 13-14 orders of magnitude of the registered signal to be reached. The value of the measured signal obtained from the PMT is divided by the attenuation of the filters and the gain of the PMT giving the intensity value at a certain time.

The limit of the dynamic range of the third-order cross-correlator is determined by the direct generation of the third harmonic (TH) from the fundamental signal in both arms of the instrument. It is well-known that the odd components of the nonlinear polarization are not equal to zero in any media and thus the corresponding nonlinear effects are unavoidable. Since the generated cross-correlation function has the frequency of the third harmonic (TH) of the input beam, it must be separated from the third harmonic signal that is directly generated by the fundamental beam through the third-order susceptibility $\chi^{(3)}$ in the nonlinear crystals. Unpublished results of the SHARP project show that because of this reason, collinear third-order cross-correlators do not support a dynamic range above 10^7 [66].

The non-collinear interaction is chosen to increase the dynamic range above 10^7. The angle between the beams plays an important role. Increasing the angle of the non-collinear interaction allows the directly generated third harmonics and the sum-frequency cross-correlation signal to be spatially separated. However, increasing the angle between the beams reduces the overlap of the SH and the fundamental beams in the crystal, hence reducing the TH signal. Thus, a high dynamic range ($> 10^{12}$) can be reached at a certain angle between the fundamental and the SH, when the balance between the efficiency of the sum-frequency generation and sufficient damping of the parasitic third harmonic signal is reached.

Since the reference arm is mechanically scanned, there are reasons to be concerned about the pulse-overlap in the crystal where the cross-correlation signal is generated. Unfortunately, it is challenging to simulate numerically or calculate analytically the measuring process. However, this interaction is very important, because as it was experimentally demonstrated, that the outcome of the measurement depends on the incoming beam profile only if a vertical slit is used.

A vertical slit was applied in the SH arm in front of the non-collinear interaction in the Sequoia in an attempt to reduce the impact of the spatio-temporal coupling by cutting the second harmonic beam. It is shown in the figure 2.4a in grey color and marked as an additional vertical slit. In this position, the vertical slit cuts spatially the second harmonic beam but not the fundamental which stays unchanged. However, since the thin slit cuts the SH beam which is used as a reference, the clipping has the potential to decrease the dynamic range of the cross-correlator. Since there is no theoretical model or a reliable simulation an experiment was performed. The width

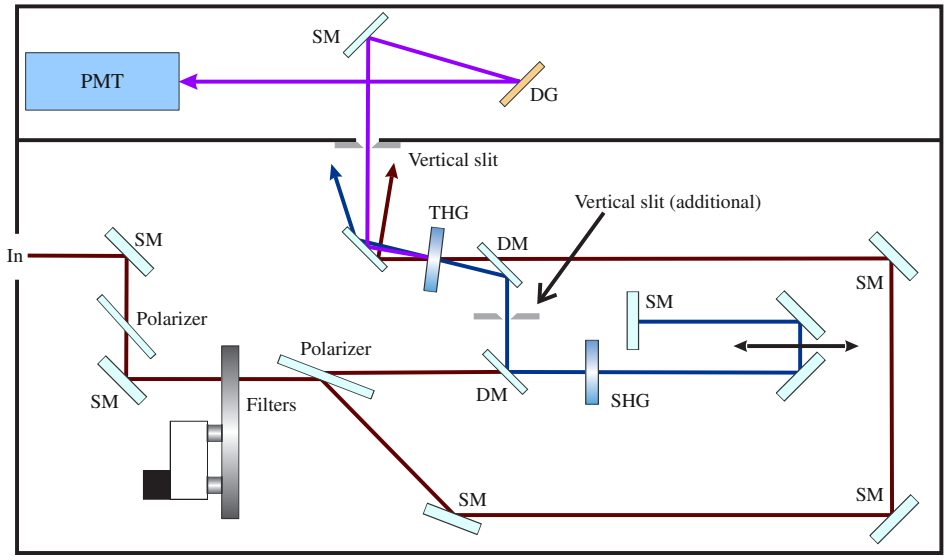

(a) Layout of the Sequoia cross-correlator

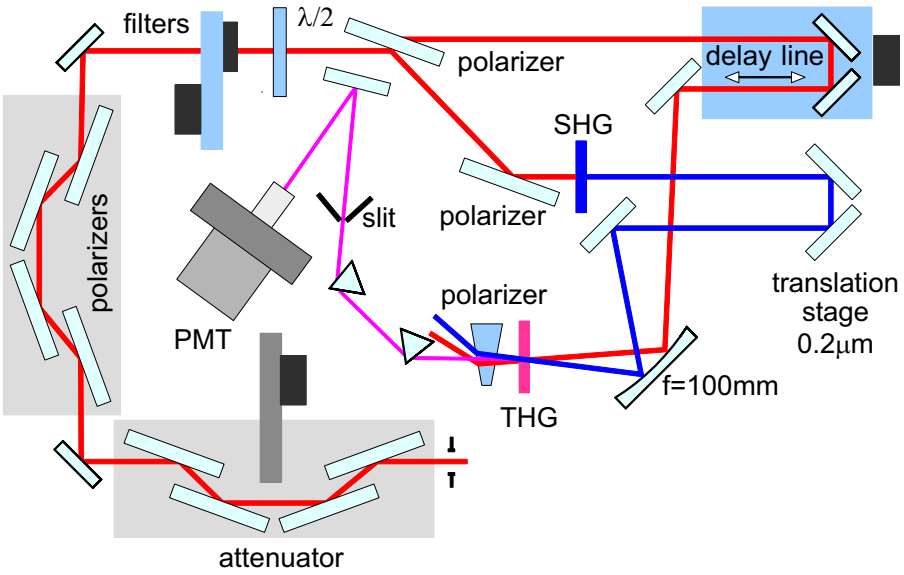

(b) Scheme of the home-made correlator

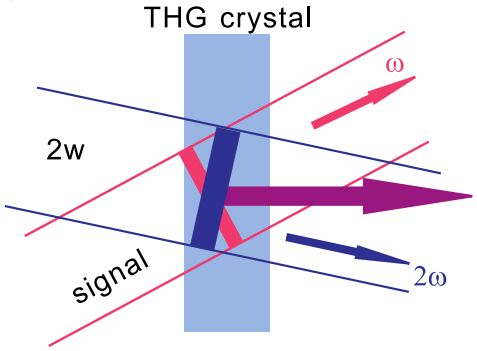

(c) Scheme of the cross-correlation wave generation in a non-collinear geometry

Figure 2.4: Principle schemes of third-order cross-correlators and the illustration of the non-collinear interaction used for the generation of the cross-correlation beam

of the slit was gradually decreased from a width of 1 mm. The cross-correlation trace was measured for every width of the slit. The experiments have shown that there is an optimal width of the slit, which allows the influence of the spatial profile to be decreased without degrading the dynamic range of the Sequoia cross-correlator. The width can be sensitive to the angle between the fundamental and its second harmonic. The vertical slit in the SH arm has minimized the impact of the spatio-temporal coupling and cancelled the dependence of the measured temporal shape on the spatial beam profile. This approach allows the conventional Sequoia to be improved and made it reliable with minimal changes to the scheme.

A similar investigation was done with the Sequoia HD cross-correlator. It was found that it does not have the spatio-temporal coupling issue. This can be associated with the proprietary focusing system implemented to focus both beams participating in the non-collinear sum-frequency generation. It may also indicate that the non-collinear sum-frequency generation is responsible for the observed issue.

The results presented in the following part of the thesis were obtained using the modified Sequoia with the vertical slit in the SH arm.

2.5.2 Temporal artefacts caused by the characterization using a third-order cross-correlator

Since the third-order cross-correlator is a self-referenced device, the reference pulse can cause temporal artefacts which do not exist in the temporal profile of the pulse to be measured. As it was mentioned above, the second harmonic is generated in one arm, after splitting the income beam into two beams. The temporal shape of the second harmonic beam is the square of the temporal shape of the initial, fundamental, beam. Thus, it contains all the temporal structures of the fundamental pulse, such as the pre-/post-pulses. The SH signal is scanned temporally against the fundamental to generate the cross-correlation signal. As a result, the post-pulses in the SH generate artificial pre-pulses and pre-pulses generate artificial post-pulses in the measured cross-correlation trace. The artificially generated pre- and post-pulses have the same shape as the pre- and post-pulses in the fundamental. For instance if the main pulse of the fundamental is asymmetric, the generated artificial pre-pulse is also asymmetric. Figure 2.5 illustrates this mechanism, where the blue curve is the temporal shape of the fundamental and the orange curve is the measured cross-correlation trace. Obviously, the position and the intensity of the pre-pulse can be well predicted if the position and intensity of the post-pulse are known. The intensity of the artificial pre-pulse is always the square root of the post-pulse intensity and the absolute value of the temporal position at the position of the post-pulse.

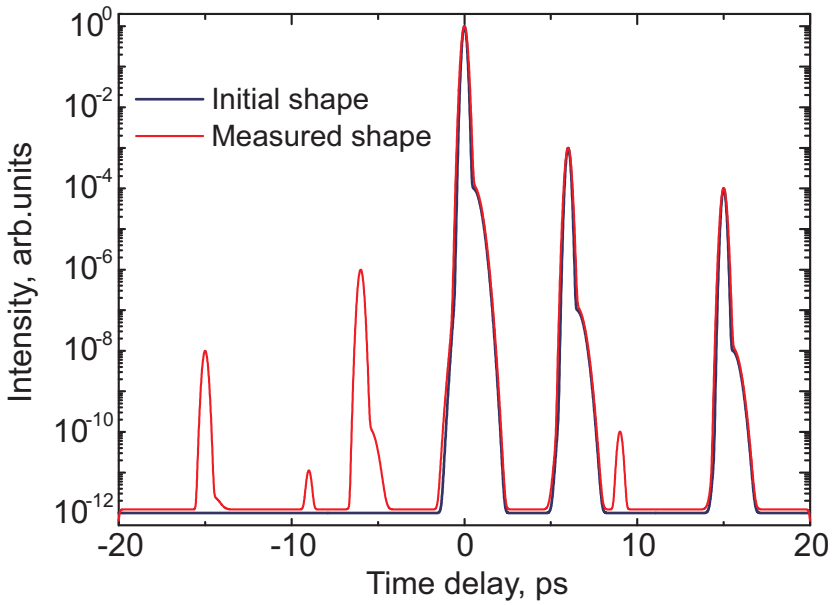

Figure 2.5: Simulation of the generation of pre-pulses during high-dynamic range characterization using a cross-correlator. Characterization of the temporal shape in the blue curve leads to the measured correlation trace shown in the red curve

To identify and avoid any impact of the diagnostics on the results, three types of third-order cross-correlators were used in the current work: the commercial Sequoia [91], the Sequoia HD (Amplitude Technologies) and the home-made high-dynamic range cross-correlator. The devices enabled a temporal resolution of $\sim$ 180 (Sequoia) and $\sim$ 60 fs (home-made). All three devices employ different optical schemes and use different optical elements. Thus, a comparison of the temporal traces measured with the help of these devices aims to minimize any possible impact associated with a certain implementation of the cross-correlator on the measured temporal contrast. In the home-made and Sequoia HD cross-correlators the fundamental and the second harmonic beams are focused by cylindrical mirrors into the crystal where the sum frequency is generated. This allows for a better temporal resolution to be reached and avoids the issues discussed in section 2.5.1.

A comparison of the traces obtained by the conventional Sequoia and Sequoia HD (Fig. 2.6) allows identifying an additional artefact ($\tau \approx 15.2$ fs) generated by the optical scheme of the Sequoia HD. The figure also shows that the Sequoia HD has a lover noise level compared with the conventional device.

2.5.3 Characterization of high dynamic range

Let us now discuss the dynamic range of Sequoia. Since it covers more than 12 orders of magnitude, it is necessary to ensure that the device is correctly calibrated and shows

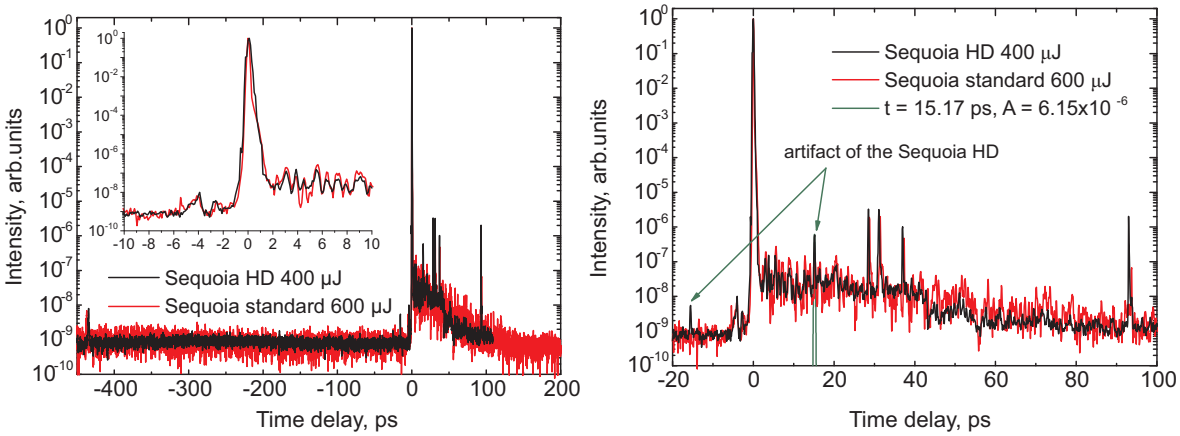

Figure 2.6: Cross-correlation traces measured using the conventional Sequoia (red curve) and the Sequoia HD (black curve). The comparison highlights a temporal artefact generated by the optical scheme of the Sequoia HD. It also shows a lower noise level of the Sequoia HD

the real dynamic range. In this section I will discuss the dynamic range of the Sequoia and a way to verify it using thin glass plates.

Technically the dynamic range is characterized by the minimal ratio achieved between the peak intensity and the noise level. The level of noise is estimated by two measurements when the signal in one of the two arms of the cross-correlator is blocked (see Fig. 2.7). The maximum of the two signals determines the noise level taken for the dynamic range estimation.

Another important parameter determines the linearity of the measured dynamic range. This parameter was measured by using uncoated glass plates installed in front of the cross-correlator (Fig. 2.8).

Two glass plates with different thicknesses (145 μm and 1.06 mm) were used. The values of the refractive indexes were cross-checked between the given catalogue value and the value calculated from the time of appearance of the post-pulses. The reflection coefficient of the glass plates at normal incidence can be obtained using the Fresnel formula

$$R = \left| \frac{n_1 - n_2}{n_1 + n_2} \right|^2 \tag{2.5}$$

where n_1 and n_2 are the refractive indices of the first and the second medium. This, in turn, yields information about the attenuation of the post-pulses. These values are represented by the square and fourth power of the first and second post-pulses respectively.

Figure 2.9 shows the measured cross-correlation traces. The post-pulses generated by the double internal reflection in the different glass plates are marked by letters and the number gives the order of the pre- or post-pulse. Number 1 is related to the first

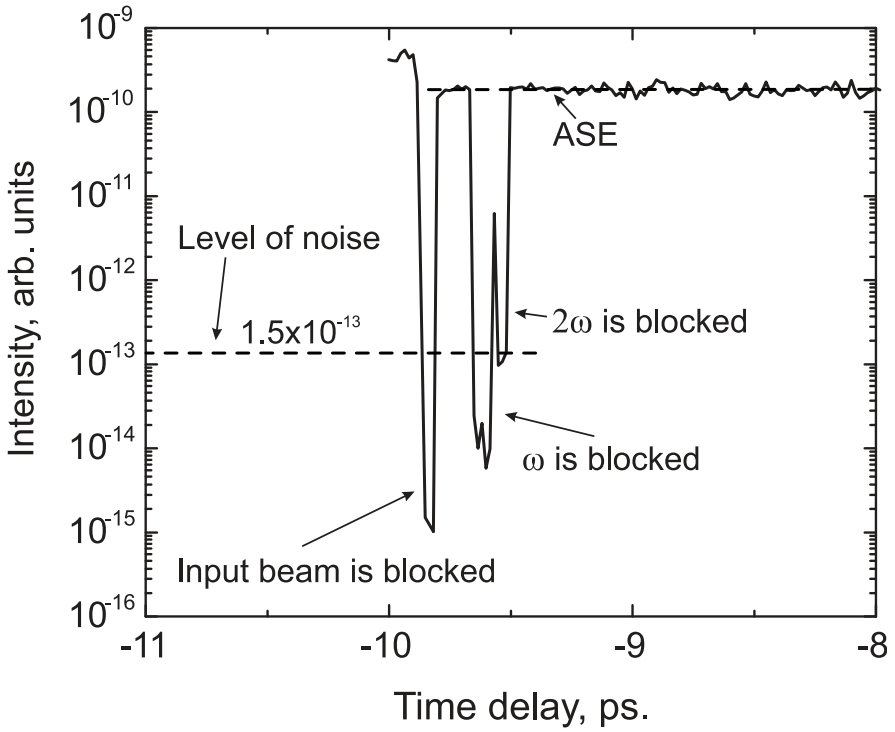

Figure 2.7: Demonstration of the optical noise level in the Sequoia by blocking the beam in the fundamental and the second harmonic arms

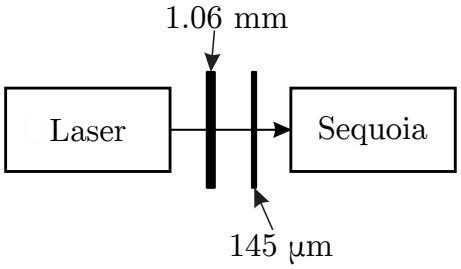

Figure 2.8: Experimental check of the linearity of the dynamic range of the Sequoia cross-correlator. Two thin glass plates are placed in front of Sequoia

internal double reflection, and number 2, to the second internal double reflection.

Two pre-pulses (-1a and -1b) can also be seen in Fig. 2.9. These artificial pre-pulses are generated by the SH in the cross-correlator (see above).

The values of the intensity calculated using the value of the refractive indices and the results of the experimental measurements are presented in Table 2.1. For a conventional Sequoia device, the measured trace (Fig. 2.9, Table 2.1) shows a good agreement with the theoretically calculated pre- and post-pulses. The difference of 2 at the intensity level of 10^{-6} is not significant and may be explained by imperfections in the glass plates (surfaces that are not clean or the plate not being strictly perpendicular to the beam). This leads to the conclusion, that the Sequoia cross-correlator was calibrated correctly.

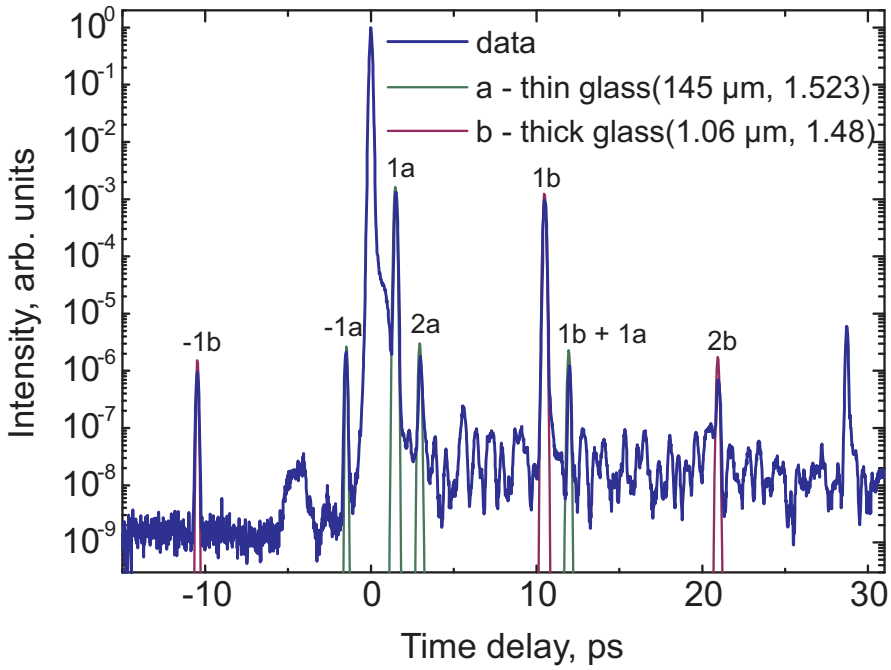

Figure 2.9: Scheme of marking the reference post-pulses. Green and purple curves represent the pulses generated by the double internal reflection in the thin plates and those which are generated by the cross-correlator as a result of the characterization

#	Delay, [ps]	Calculated intensity [arb. units]	Measured intensity [arb. units]
Thin glass, s = 145 μm, n = 1.523			
1a	1.5	1.8×10^{-3}	1.3×10^{-3}
2a	2.9	3.4×10^{-6}	1.7×10^{-6}
-1a	-1.5	3.4×10^{-6}	2.1×10^{-6}
Thick glass, s = 1.06 mm, n = 1.48			
1b	10.5	1.4×10^{-3}	9.9×10^{-4}
2b	20.9	1.96×10^{-6}	9.8×10^{-7}
-1b	-10.5	1.96×10^{-6}	9.6×10^{-7}
Thin + thick glasses			
1a + 1b	11.9	2.6×10^{-6}	1.21×10^{-6}

Table 2.1: Table for comparison of the parameters of the pulses obtained from the geometry and medium of the glass plates and measured using the Sequoia cross-correlator

Saturation effects in a third order cross-correlator

The nonlinear optical processes in a cross-correlator, such as SHG or the sum-frequency generation may show a saturation effect [98]. When a low level signal is measured, all filters are removed from the beam path in the Sequoia device. Thus, the full power input beam goes to generate the SH signal. If the SHG process is saturated, it produces a lower SH signal than it would generate without the saturation. As a result, the generated cross-correlation signal is also weaker compared with that what would be generated without the saturation of the SH. This leads to a lower ASE level detected by the Sequoia and an artificial increase of the temporal contrast in the measured trace.

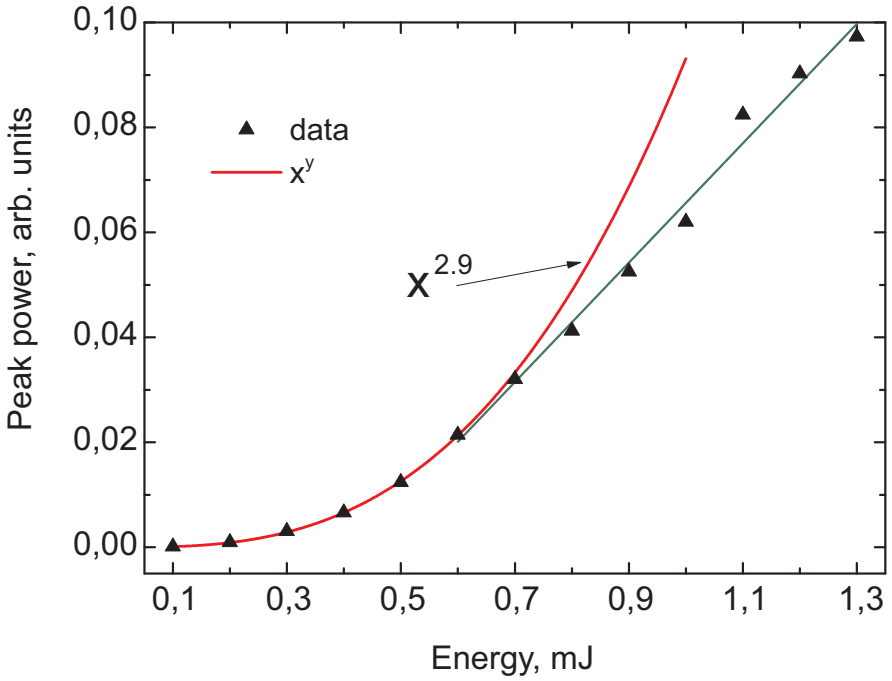

Figure 2.10: The saturation of the peak intensity measured using the Sequoia. Black triangles are the experimental data, whereas the red curve corresponds to fitting to a power law with an exponent value close to 3

On the other hand, the measured absolute peak intensity must grow as a cubic function of the input intensity. Figure 2.10 demonstrates how the peak intensity changes when varying the input beam energy. The laser energy was tuned using the combination of a half-wave plate and a polarizer. The level of saturation depends on the beam parameters. In this case ($\tau_{\mathrm{fwhm}} \approx 25\,\mathrm{fs}$, beam diameter d $\approx 4\,\mathrm{mm}$ in front of the Sequoia) the peak signal starts to be saturated when the energy level exceeds 0.7 mJ.

Chapter 3

Investigation of temporal contrast on the picosecond time scale

3.1 Introduction

In the previous chapter techniques suitable for the high-dynamic range characterization of temporal contrast have been presented. We have seen that the commonly used Sequoia cross-correlator has issues and found a way to make it more reliable.

From the moment that Double CPA (DCPA) was demonstrated [17], only little research has been performed to understand and improve the temporal contrast of Ti:Sapphire laser systems. The reason for this could be the availability of plasma mirror technology that works well even for PW laser systems and that allows the problem of the temporal contrast to be solved, although only for low repetition rate systems. DCPA with XPW filtering allows for strong suppression of the ASE level but this technology is still limited by the damage threshold of diffraction gratings in the stretcher to an ASE level of $\sim 10^{-15}$ of the main pulse. Thus, this technology can be successfully used for new generations of Petawatt lasers and slightly above. However, the problem with the long pre-pedestal at the leading edge of the main pulse which appears on a picosecond time scale remains unsolved. Currently, several scientific groups are working on improving the temporal contrast of high-power laser systems [99, 100]. Previous publications considered pedestals in the picosecond time range appearing at both edges of the main pulse to be related to scattering of the stretched pulse off the diffraction gratings in the stretcher [101]. During the last few years, parametric processes are actively used for temporal contrast cleaning [102, 103]. The temporal range of interaction of parametric processes is limited by the duration of the pulses participating in the interaction. By shortening the duration of the pump pulse, the temporal range of the temporal artefacts (parametric fluorescence, pre-pulses) can be

significantly reduced. Parametric processes are not in the scope of this work and thus will not be considered in detail.

In this chapter I am going to consider assumptions known in literature, their experimental validation, original experimental results and relevant discussion. The chapter starts with an investigation of the possible dependence of the temporal contrast on spectral clipping which can occur in a stretcher or a compressor. In the section 3.3 the influence of different stretcher/compressor designs is discussed. After that, the birefringent-cause degradation of the temporal contrast will be presented in section 3.4

3.2 Impact of spectral clipping in a stretcher or a compressor on the temporal contrast

One of the possible sources of temporal degradation mentioned in the literature [7], are spectral clippings that can occur in the stretcher or compressor. Since the clipping can occur in a complex part such as the stretcher, when the pulses are not transform-limited, it may impact the temporal contrast. This can be experimentally investigated and this we are going to do in this paragraph.

Spectral clippings can occur in stretchers and compressors due to the limited size of optical elements, such as the diffraction grating. This effect and its potential influence on the temporal contrast has been discussed in detail [47]. The authors of [47] developed a simulation method to predict the possible contrast distortion caused by this sort of clipping. The simulation in [47] has shown that the possible influence is comparatively low and lies in the sub-picosecond time range in the area around the main peak. The tools currently available for high dynamic characterization do not support high temporal resolution at that high dynamic range and thus these features are difficult to observe. It is worth to remind that the Wizzler allows the pulses to be characterized with a high temporal resolution, however the dynamic range of the available devices is practically limited by 4 orders of magnitude. The Wizzler HD was not commercially available when this investigation was performed. It is nonetheless worth trying to increase spectral clipping in the experiments and to observe the measured cross-correlation traces.

Several experiments with spectral clipping were performed with two types of stretchers: the stretcher based on prisms and the stretcher based on a reflective diffraction grating. There is an area, in both stretchers (and compressors), where all spectral components propagate co-linearly. This place is in front of the back reflector, injecting the beam back through the stretcher/compressor for the second path. Spectral clipping may be easily arranged here by using a screen to block certain spectral components

and it is then quite simple to check the theory with this approach.

This section starts with the experimentally obtained curves using the prisms-based stretcher and these are shown in Fig. 3.1. In the first series of experiments, the beam was clipped on both the blue and red sides of the spectra (Figs. 3.1a and 3.1b). Both clippings are clearly visible in the spectra.

It can be seen in Fig. 3.1a and 3.1b that the changes to the temporal trace are visible with higher clipping, as presented in the blue curve. The changes behind the main pulse can be neglected due to their smallness. There is a big distortion of the broad pre-pulse at around -6 – -3 ps which has almost disappeared in the blue curve. The spectrum was clipped separately on both the red and blue sides in the second experiment and Figs. 3.1c and 3.1d show that only the clipping on the blue side of the spectra results in changes to the pre-pulse. The explanation of this result requires further investigations and it stays unresolved here. Concerning the leading front of the main pulse, no distortions of the main pulse are observed.

A similar experiment was performed using a reflective diffraction grating-based stretcher and the results are shown in Fig. 3.2. These results are markedly different to the results in Fig. 3.1 as there is a significant broadening of the re-compressed pulse and *"wings"* start to appear when the clipping is on the red slope.

In the third case, the spectrum was clipped in the compressor based on the reflective diffraction gratings, and the results are shown in Fig. 3.3. Despite to significant spectral clipping, no changes are visible in the measured temporal traces.

It is necessary to explain the difference between the pulse clipping in the stretcher and compressor based on the reflection diffraction gratings. The difference in clipping in the stretcher with a reflection grating (Fig. 3.2) and in the compressor (Fig. 3.3) results in different re-compressed pulse shapes. Peak broadening is observed for clipping in the stretcher but not in the compressor. The beam size is the cause of this observed difference [47] as the beam is much smaller in the stretcher compared to the compressor. The beam must be expanded prior to the compressor to avoid optical damage of the diffraction gratings. The beam size inside the compressor smoothens the effect of the beam clipping, as mentioned in [47].

The system reacts very differently in the case of the prisms-based stretcher. This may be associated with the sign of the chirp, the stretching ratio or the specific dispersion properties of the prisms-based stretcher. The spectral clippings in all of the experiments is significant and is directly observable in the spectra. This situation has a low probability of occurring within in a real laser system because clipping would be easily detected. However, the significant level of clipping was induced in order to detect changes in the temporal trace.

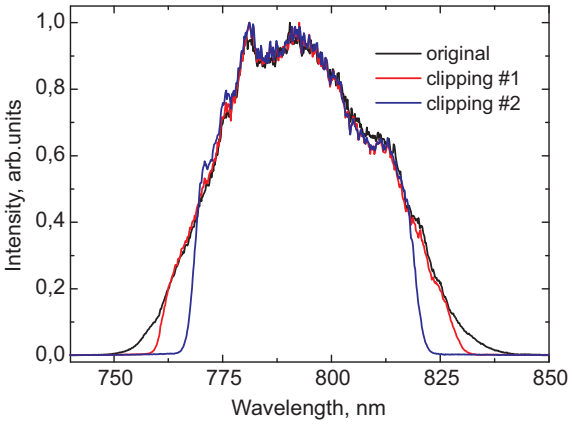

(a) Spectra in cases of two-side clippings

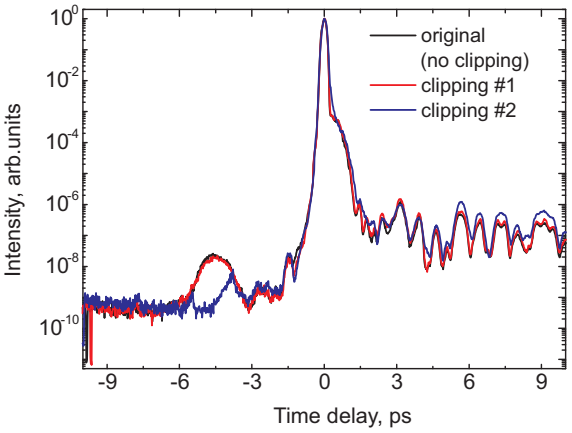

(b) Sequoia traces in case of two-sided spectral clippings

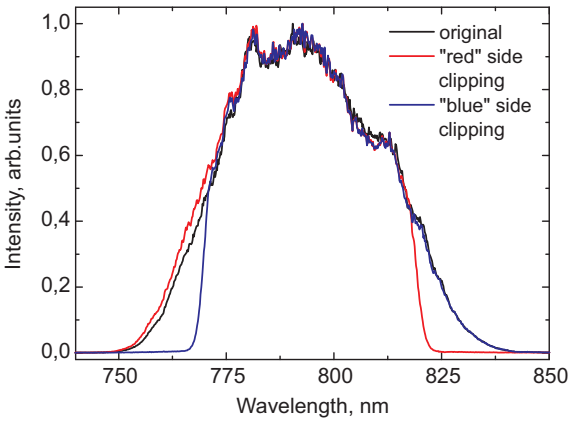

(c) Spectra in case of one-sided clippings

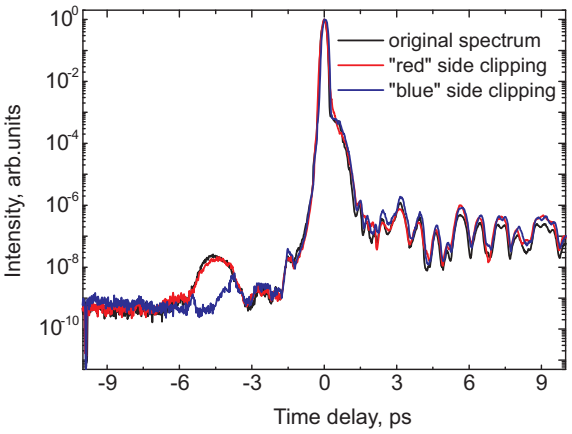

(d) Sequoia traces in case of one-sided spectral clippings

Figure 3.1: Spectral clipping in the stretcher based on prisms and the corresponding temporal traces

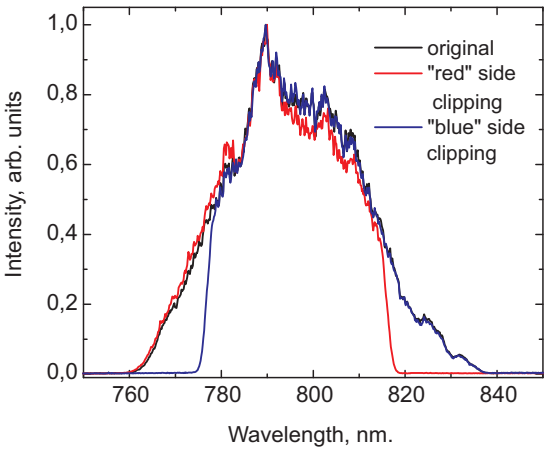

(a) Spectra in case of one-sided clipping

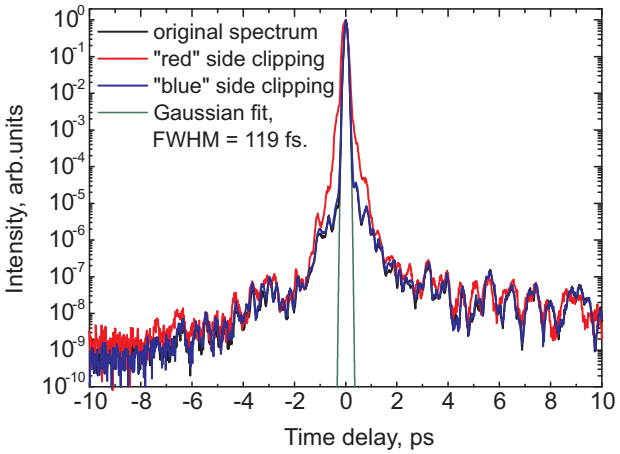

(b) Sequoia traces in case of one-sided spectral clipping

Figure 3.2: Spectral clipping in the stretcher based on the reflective diffraction grating and corresponding temporal traces

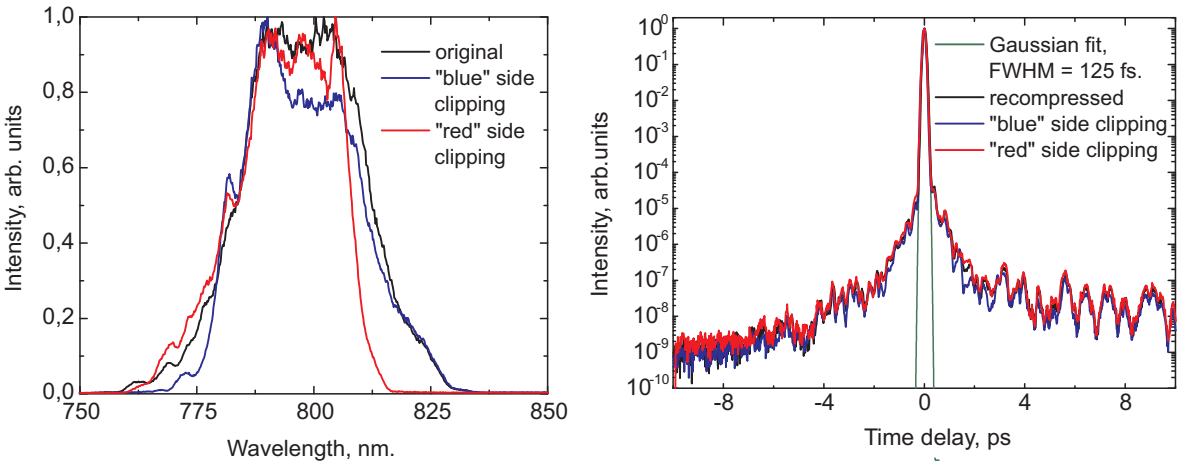

(a) Spectra in case of one-sided clipping

(b) Corresponding Sequoia traces

Figure 3.3: Spectral clipping in the compressor with two reflective diffraction gratings

Only one experiment has shown significant changes in the shape of the main pulse. It is worth comparing this result with the numerical simulation using the methods from [47]. The software implements direct ray tracing taking into account a limited beam size with a super-Gaussian spatial profile of intensity. A compressor based on two parallel reflective diffraction gratings is simulated. A beam of a limited size gets diffracted on the first diffraction grating resulting in an angular distribution of the spectral components. The diffracted light falls on the second diffraction grating of limited size. Adjusting the size of the grating may lead to a situation where the beam gets clipped on the edge of the grating. This clipping is both, spatial and spectral within the aperture of the laser beam. The red or blue slopes of the spectrum can be clipped in the described way. The Fourier transformation of the resulting spectrum gives the temporal shape of the pulse in the focal plane. The simulation shows the similar pulse shape distortion in both, the blue and red side clipping of the spectra.

Since the changes of the fronts of the main pulse were only observed experimentally in the case of the reflective diffraction grating-based stretcher, the experimental curve for this experiment is taken for the comparison presented in Fig. 3.4. The main pulse in the experimental curve (Fig. 3.4, black) was fitted (thin blue curve) by a Gaussian function in order to obtain the approximate temporal response of the Sequoia cross-correlator. A convolution of the simulation curve with the Gaussian fit was performed to simulate the process of characterization with the Sequoia and the resulting curve shown in green is in Fig. 3.4.

Similar broadening near the main pulse at an intensity level between 10^{-5} and 10^{-3} of the main peak maximum can be observed in the experiment (red curve in Fig. 3.4) and in the results of the numerical simulation (green curve). The simulation

therefore shows a rather similar effect for the rough spectral clipping. The good match between the calculated and measured curves in the pedestal below 10^{-5} confirms that the pedestal may appear because of the spectral clipping. In this case, the spectral clipping must be significant, as presented in Fig 3.3a. In this case the spectral clipping will degrade the pulse duration also as can be seen in Fig. 3.4.

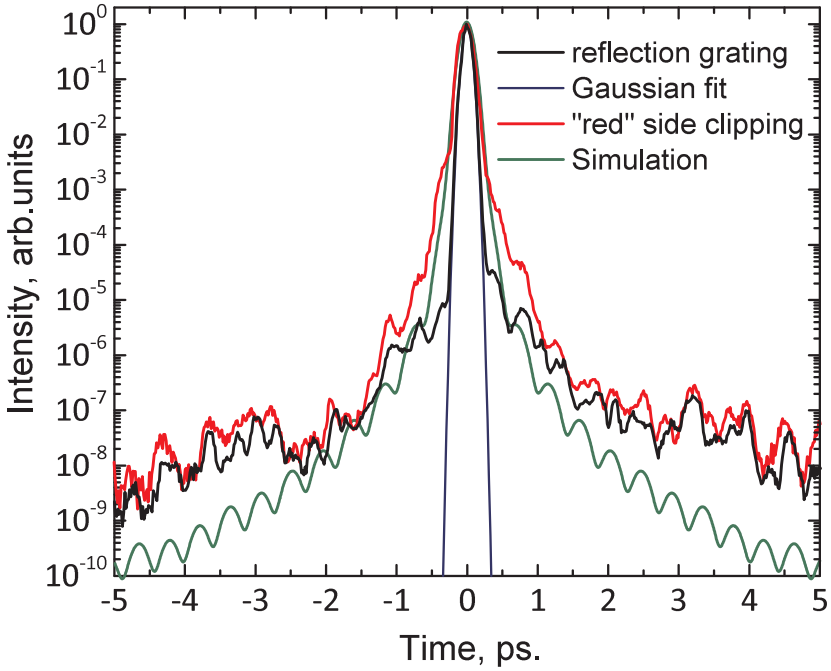

Figure 3.4: Experimental curves and simulation of spectral clipping in a compressor with reflective diffraction grating. The black and red curves correspond to the measured temporal traces with unclipped and red-side clipped spectra respectively. The green curve shows the results of a numerical simulation where the spatial and spectral clippings are simulated in a scheme based on two parallel reflective diffraction gratings. In the simulation the spectrum was red-slope clipped

The experiment with the spectral clipping has shown the viability of the numerical simulation model implemented. Currently available high dynamic range characterization methods do not allow for the effects of small spectral clipping to be observed due to the limited temporal resolution at high dynamic range. The considered case, where significant clipping can appear, can be easily detected within a real laser system analysing the pulse spectrum and duration.

3.3 Comparison of stretcher/compressor configurations

There are different designs of the stretcher/compressor combination that are used in CPA laser systems. Currently, the influence of their particular design on the temporal contrast has not been sufficiently studied. Various stretcher/compressor schemes were studied in terms of aberrations and wavefront distortions only. However, a particular implementation of the stretcher/compressor as well as the dispersive elements used can also impact the temporal contrast near the main peak. An attempt to perform this investigation is known in the literature [99, 101], where the influence of different optics in a stretcher on the long pre-pedestal (marked in red in the Fig. 1.9) was investigated. The authors of [99, 101] concluded that the use of a transmission diffraction grating in the stretcher gives a shorter pre-pedestal and a better leading edge than in the case of using reflective diffraction gratings. It is also suggested in [99, 101], and continued in [104], that the observed difference can be explained by the roughness of the optical surfaces of the elements that make up a stretcher or compressor. Moreover, the authors of [105] suggest that both, the pre- and post-pedestals appearing around the main peak may be explained by parasitic scattering in the stretcher and compressor. This section shows results of a comparison between different designs of stretchers and compressors. Their role and influence on the temporal contrast is clarified.

Cross-correlation traces, related to the three stretcher/compressor pairs described in section 1.6, are presented in Fig. 3.5. The red and black curves in Fig. 3.5 are related to the laser system configuration with prisms and reflective diffraction grating stretchers. The blue curve is related to the case of the transmission diffraction grating-based stretcher.

Since the impact of the scattering on the pedestal of the main peak is considered in the literature, I start with a discussion of the pulse contrast in the vicinity of the main peak in the time range from -2 to 2 ps, then consider the preceding region and the trailing region following the pulse. It can be seen that the leading and trailing edges of the main peak show significant differences. The observed difference reaches more than two orders of magnitude at -1 ps. The configuration with the transmission diffraction grating-based stretcher shows a shorter leading edge compared to the stretcher based on the reflective diffraction grating, similar to what is published in [101]. However the difference in the length of the leading pedestals is smaller than is presented in [101]. The leading edge is short and steep in all three configurations of the CPA system. It does not show a long and growing leading front of the main pulse, as is commonly visible in high-power laser systems. Usually, the pre-pedestal has a duration of tens and

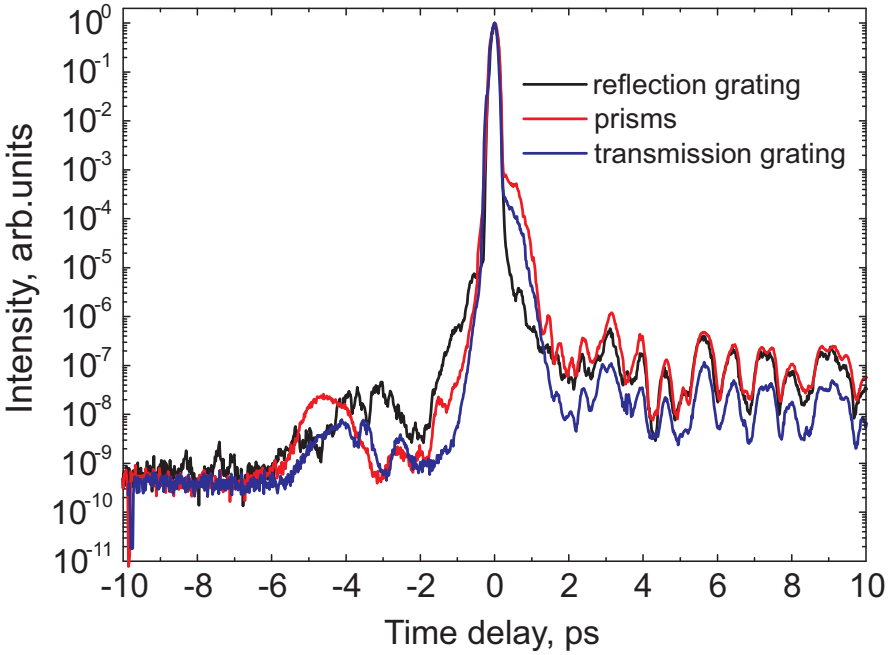

Figure 3.5: Comparison of Sequoia traces obtained with the bulk-based compressor, the stretcher based on transmission diffraction gratings (blue curve), prisms (red curve) and the stretcher/compressor configuration with reflective diffraction gratings (black curve)

even hundreds of picoseconds. Our results support the conclusions presented in [101] that the stretcher with transmission gratings is better for temporal contrast, however the reasons for this phenomenon discussed in [101] are not convincing. In chapter 4 I will present my vision of the problem and reinterpret the results from [99, 101]. In particular I will argue that the long pedestal in front of the main pulse is often observed in high-peak power Ti:Sapphire-based laser systems and that this pedestal is generated from the coherent post-pedestal in CPA systems. It its turn, the post-pedestal is the artefact caused by the Ti:Sapphire medium itself.

It is worth drawing attention to the long pre-pulse in the range -6 – -2 ps that is visible in figure 3.5. The shape of it slightly varies depending on the stretcher/compressor configuration. However, this long pre-pulse is stable and is slightly changed only by the spectral clipping discussed in 3.2. Unfortunately it is still unclear what can be source of this pre-pulse. Excluding this peak, all three stretcher/compressor configurations do not show any other pre-pulses at least until -420 ps.

Concerning the publication [105] which shows that scattering in the stretcher is responsible for the long pre-pedestal which is marked in red in 1.9 and as long as tens of picoseconds, one can say that our system in the tested configurations does not show this typically observed long pre-pedestal. The nature of this long pre-pedestal is not caused by scattering and together with the post-pedestal it will be considered and

explained in detail in the chapter 4.

3.4 Specific issues of high-power cascades

The main differences between a high-power laser and classical front-end are the scale and scope. A power laser system consists of more amplifiers which allow the delivery of higher energy and, as a consequence, higher peak power and intensity. Higher pulse energy creates the need for a larger beam diameter to avoid a high intensity. This, in turn, may lead to unwanted phase distortion or an optical breakdown of the optics in the laser chain. High aperture and energy prevent the use of dispersion control devices, such as the Dazzler and Mazzler, in high power cascades. This limit is associated with difficulties in making specific large crystals with the required optical quality. In principle, it is still possible to use a Pockels cell with a big aperture to cut out temporal artefacts in the nanosecond time range. However, this means that a large amount of glass is placed in the beam path resulting in an undesirable change in the B-integral value. On the other hand, large optical quality Ti:Sapphire crystals with a thickness of several centimetres are commercially available. Their size makes these crystals expensive and, as a consequence, the crystals are not cut at the Brewster angle, but a normal cylindrical geometry is applied. These limitations affect the design of high-power cascades, which in turn, impacts the temporal contrast.

It is well-known that the Brewster cut of the active medium is designed to keep the laser light linearly polarized to suppress the second, orthogonal, polarization component. It significantly reduces the depolarization due to non-ideal alignment of the optical elements and other factors. The Ti:Sapphire crystal is a birefringent medium, where two perpendicular polarization components co-exist.

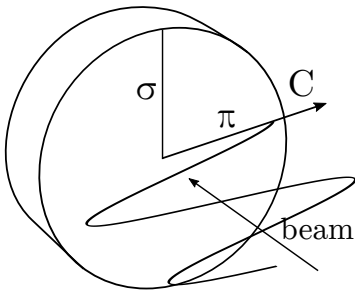

Figure 3.6: Orientation and selected direction of the birefringent Ti:Sapphire crystal

A crystal is usually not perfectly aligned by angle and, as a consequence, the angle between the seed pulse polarization and π axis of the crystal is small but not zero. This leads to decomposition of the linear polarization of the seed into two perpendicular polarization components in the crystal. The orthogonal polarization components propagate with different speeds inside the crystal due to the difference in the refractive indices. This leads to the delay of one component with respect to the other one. Usually, the π direction is used for amplification due to the higher cross-section, which determines the gain factor. For the Ti:Sapphire crystal, the π component corresponds to the extraordinary wave, con-

sequently, σ corresponds to the ordinary wave.

The intensity-driven changes of the refractive index and the population inversion [106] will change the difference between n_e and n_o. However, this effect is neglected in this investigation and the delay of the post-pulses, introduced by birefringence, is estimated only. The corresponding refractive indices of a sapphire crystal at 20 ℃ are n_e (800 nm) = 1.7522; n_o (800 nm) = 1.7601 [107, 108]. As a result, the π component (extraordinary wave) propagates faster than the σ component (ordinary wave). After the first pass through the crystal, we obtain two perpendicularly polarized pulses with a delay Δ between them, determined by the thickness of the birefringent crystal and the difference between the refractive indices. The ratio in intensity at the exit of the crystal will be different from the intensity at the entrance due to the difference in emission cross-sections of the π and σ components of the polarization.

A Brewster cut crystal would filter the parasitic polarization. However, crystals in high power cascades are usually cut for a normal incidence of light. Another option, to filter the parasitic delayed component, would be a reflective polariser, placed after the crystal. However, it makes the scheme more complicated and expensive.

It is complicated to implement the optical scheme in a way that makes the beam propagate in a flat plane. Usually there is a slight variation of the beam height on the optical elements between passes. This will cause a polarization rotation effect while propagating through the cavity of an amplifier. Thus, the polarization components will be slightly rotated with respect to the birefringent planes of the crystal and as a result, both the main and delayed polarization components will have a projection on the π and σ axis. The second pass through the crystal will again split the pulses in time. Considering their projections on the axis of the crystal, there are two pulses in both π and σ directions with different delays. The π component will consist of pulses with zero and Δ delays, whereas the σ component will consist of two pulses with Δ and $2 \times \Delta$ delays. The following passes only increase the number of post-pulses. Therefore, a number of post-pulses will be observed at the exit of the crystal, with a delay according to the difference between the refractive indices of the orthogonal polarization components. The resulting temporal shape is quite complicated, however one can say that the number of post-pulses generated in such a way linearly depends on the number of passes in a multi-pass amplifier. If the birefringence of the crystal has the opposite sign, it will cause pre-pulses instead of post-pulses.

Chapter 4

Investigation of the ragged pre- and post- pedestals

4.1 Introduction

The chapter is devoted to the part of the pulse shape which was never in focus in previous studies of pulse contrast. I am going to discuss the temporal region which follows the main pulse and impacts the temporal contrast before the main pulse. I start this chapter with an introduction to a new diagnostics method which allows coherent/uncoherent parts of the measured temporal traces to be distinguished. Then, in section 4.4.1 I discuss a long pedestal appearing in front of the main pulse in high-power lasers based on the use of Ti:Sapphire crystal. I will explain its nature and show that it originates from the pedestal after the main pulse. The new diagnostics is actively used in this investigation. Then I focus on the temporal area lying after the main pulse and identify the source of the parasitic post-pedestal. In section 4.4.4 and 4.4.5 I will present a plausible theory for the appearance of the post-pedestal. Finally I consider the pulse shape of a home-made high-field (100 TW) laser system and analyse it in 4.5.

It is necessary mentioning that some parts of the results presented in this chapter are strongly related to a publication [109] where I am the corresponding author who prepared the first draft of the manuscript.

4.2 Diagnostics of coherence

There are two articles, both published in 2008 [110, 111], which describe a mechanism leading to pre-pulse generation from a post-pulse. These two publications are the experimental and theoretical descriptions of a series of nonlinear processes, leading to

generation of artificial pre-pulses in CPA lasers. The physical phenomena behind these mechanisms not only significantly impact the temporal contrast but can also be used to investigate which parts of the re-compressed pulses are coherent with the main pulse.

The mechanism, discussed in [110, 111] may be split into a few steps. The temporal shape can be assumed to consist of a main pulse and a post-pulse. The post-pulse is considered to be coherent with the main peak. This situation for example may happen if the post-pulse appears through double internal reflection in an optical element such as a thin lens, active medium or a window in a Pockels cell. After being stretched, two similarly stretched pulses, deriving from the main pulse and the post-pulse, are obtained. If the delay between the pulses is small enough, the stretched pulses will overlap in time. When the pulses are strongly chirped, the temporal evolution of the pulse follows its spectral evolution but the chirp introduced by the stretchers is not constant over the whole spectral range of the pulse spectrum. The time axis may then be presented as a nonlinear axis of wavelengths or frequencies. The overlap causes an interference pattern in the time domain due to the coherence of both pulses. This interference pattern depends on many factors, including the dispersion introduced by the stretcher, the delay between pulses and their relative intensities. The modulation of intensity induces phase distortions because of the intensity dependence of the refractive index and, as a result, the modulation pattern is imprinted on the temporal phase of the light propagated in a nonlinear medium.

The value of the nonlinear refractive index n_2 and the propagation length determine how strongly the intensity profile will be imprinted on the shape of the spectral phase. The phase of the stretched pulse will be modified according to the interference pattern only in the area of temporal overlap of the main pulse and its replica. The re-compression stage may be considered as an inverse Fourier transformation, which finally makes two pulses appear temporally symmetric with respect to the main pulse [112]. These are now post- and pre-pulses. The described mechanism works in both directions and the energy transfer is possible also in the reverse direction from pre-pulse to post-pulse. The observed effect is a disadvantage of the Chirped Pulse Amplification technique.

Along with the disadvantages, these phenomena may also provide tools for temporal contrast investigation. The fact that interference is involved leads to the conclusion that only artefacts coherent to the main pulse will generate pre-pulses as discussed above. This leads to an interesting fact: one can use the described phenomena to obtain information about the **coherence** of the temporal artefacts. This may form the basis for a powerful technique for determining the coherence of parts of the measured temporal trace. This may help in the analysis of the measured temporal cross-correlation traces.

In [110], a theoretical prediction for the energy of the pre-pulse generated from the post-pulse is given (4.1).

$$E_{\mathrm{pre-pulse}}/E_0 \approx 0.58B^2W \tag{4.1}$$

where the term W is the relative energy of the post-pulse, the B is the *"breakup"* integral value indicating the accumulated nonlinear phase, E_0 is the energy of the main peak, and $E_{\mathrm{pre-pulse}}$ is the energy of the generated pre-pulse. It is worth mentioning that a flat-top pulse profile is considered in [110]. Thus, the impact of the stretched pulse shape is not taken into account.

A numerical calculation, presented in [47] shows a similar dependence:

$$E_{\mathrm{pre-pulse,1}}/E_0 \approx 0.343B^2J \tag{4.2a}$$

$$E_{\mathrm{pre-pulse,2}}/E_0 \approx 0.042B^4J^2 \tag{4.2b}$$

where J is the relative intensity of the post-pulse compared to the main pulse, and $E_{\mathrm{pre-pulse,1}}$ and $E_{\mathrm{pre-pulse,2}}$ are the energy of the first and second order pre-pulses, respectively. Equations (4.1) and (4.2) offer the opportunity to predict the intensity of the first replica only. However, the physics of this mechanism will also lead to second- and higher-order pre-pulses; [47] also contains predictions for higher orders.

A series of experiments were carried out in order to show how the generation of a pre-pulse from a post-pulse works. The simplest way to show the generation of the pre-pulse is to introduce a thin plane parallel glass plate into the laser beam. Internal double reflection on the glass plate surfaces makes for a well-defined post-pulse in the temporal trace. The accumulated nonlinear phase (B-integral) depends on the pulse intensity, the nonlinear refractive index of the medium n_2 and the propagation length. The nonlinear phase gets accumulated during the pulse propagation through the laser system. Thus, a pre-pulse will be generated from the post-pulse and its energy will be proportional to the B-integral accumulated after the glass plate. The energy of the generated pre-pulse decreases while moving the glass plate from the stretcher towards the pulse compressor. The most energetic pre-pulse can be generated when the glass-plate is located just in front of the stretcher.

In order to be confident that the B-integral of the system is not small, it was artificially increased. This can be implemented by changing the optical path in an additional transparent material placed in the stretched pulse. Since the n_2 of air is comparably small, the B-integral of the system can be dynamically changed by placing plane parallel glass plates of different thicknesses into beams of different diameters. A 1:1 Kepler telescope was designed in front of the bulk compressor for that purpose and this telescope provides a variation in the diameter and thus also the intensity. It

is schematically illustrated in Fig. 4.1. A quartz medium was used as the nonlinear medium. The beam size, energy and pulse duration determine the intensity, while the material and geometry of the medium determine the n_2 and the interaction length. The additionally accumulated nonlinear phase (B-integral) can be estimated using equations (1.28) and (1.29).

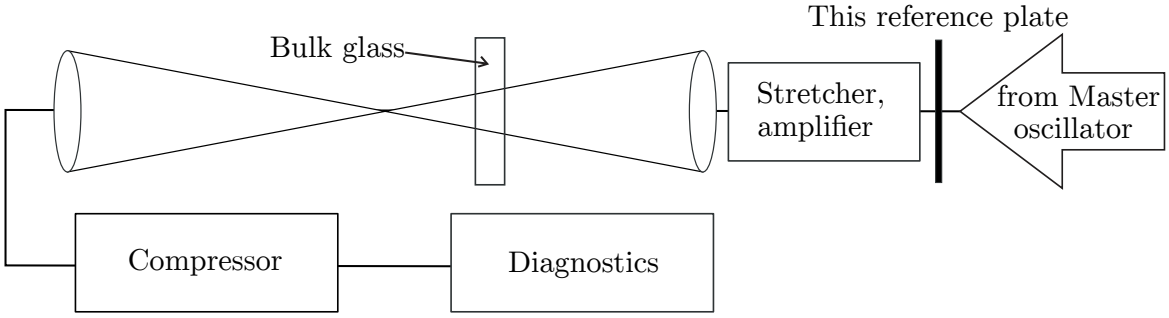

Figure 4.1: Scheme of experiment where the influence of the B-integral on the formation of a pre-pulse from a post-pulse was investigated. A thin glass plate creates the reference post-pulse and a 1:1 telescope with a set of parallel glass plates changes the value of the accumulated B-integral in front of the re-compression stage

A thin glass plate was placed in two different positions, either in front of the amplification stage or behind the re-compression stage. In the first case, the relative amplitude of the pre-pulse (related to the post-pulse) yields information regarding the impact of the nonlinear phase accumulated in the amplifier and the compressor. In the second case, it indicates the impact of the second harmonic generated in the cross-correlator. In Fig. 4.2, the resulting cross-correlation traces are presented for the stretcher based on the transmission diffraction grating and the bulk compressor.

Figure 4.2 shows that the thin glass has created two post-pulses. The delay between the pulses is determined by the thickness and the value of the refractive index of the glass plate. The glass plate thickness is approximately $\approx 340\,\mu$m. The intensity ration between the main and post-pulses provides information about the ratio between the refractive indices of the glass and the air in the laboratory and can be simply estimated by using the Fresnel equation (2.5), if a normal angle of incidence is assumed.

There is good agreement between the two curves except for the region of the pre-pulse, at approximately $\approx -4\,$ps. When a thin parallel glass plate is placed into the beam in front of the stretching stage this leads to the creation of a post-pulse . Then, both the main pulse and the post-pulse are stretched and overlap in time. Further propagation and re-compression leads to the generation of a pre-pulse through the mechanism discussed above. The result can be seen in the black curve in Fig. 4.2. The pre-pulse in the red curve corresponds to the pre-pulse generated in the Sequoia as was mentioned in paragraph 2.5.2. As expected its intensity is the square of the intensity

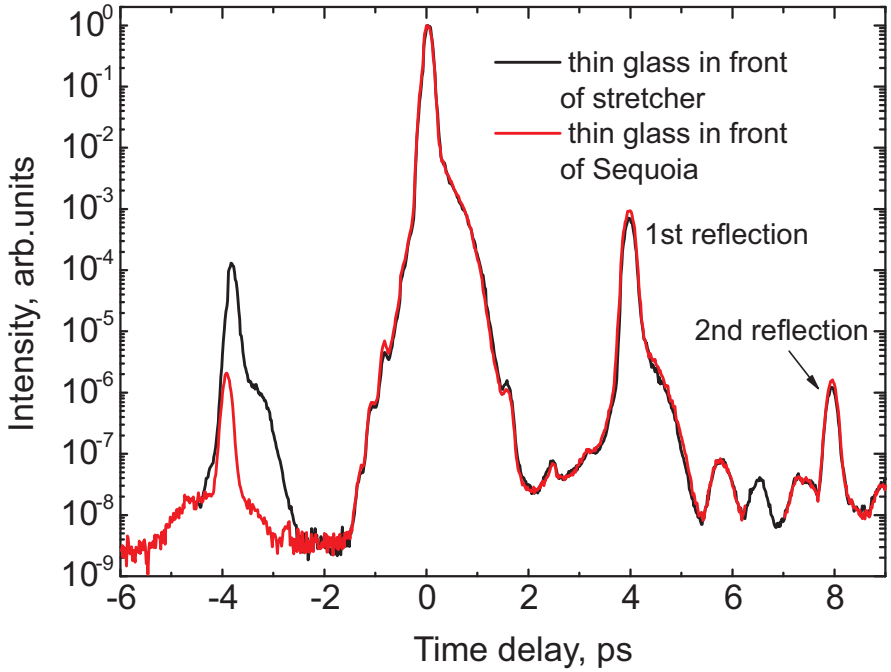

Figure 4.2: Sequoia traces measured for a different location of the reference glass plate in the experiment aiming at checking the impact of the B-integral on the temporal pulse shape. The reference plate was located in front of the Sequoia (red curve) or in front of the stretcher with the transmission grating (black curve)

of the corresponding post-pulse.

In the second experiment, the glass plate was located only in front of the stretcher and the B-integral value was varied by using bulk glass plates of different thicknesses installed inside the telescope (see Fig. 4.1). The obtained curves are shown in Fig. 4.3.

It can be seen that, despite the glass plate being located only in one position, different intensities of the pre-pulse can be observed. The B-integral values are 0.1 and 1 radian. As was predicted in [110], the energy and hence the intensity of the pre-pulse at the higher B-integral value is higher than in the case at the lower B-integral value.

In principle, it allows for a measurement of the B-integral value in different parts of the laser system. However, as was mentioned above, the real temporal trace can not be measured without the *"artificial"* pre-pulse produced by the Sequoia if the B-integral value is low (it will be masked by the *"ghost"* pulse generated by the SHG). Due to the fact that the SH signal generates a pre-pulse on the measured curve, the B-integral value of the system can only be approximately estimated if it exceeds a certain value. This minimum measurable value of the B-integral depends on the intensity of the post-pulse.

The post-pulse created through the double internal reflection in the plane parallel glass plate may indicate changes of the accumulated nonlinear phase in a part of the laser system. Any temporal structure coherent with the main pulse produce corre-

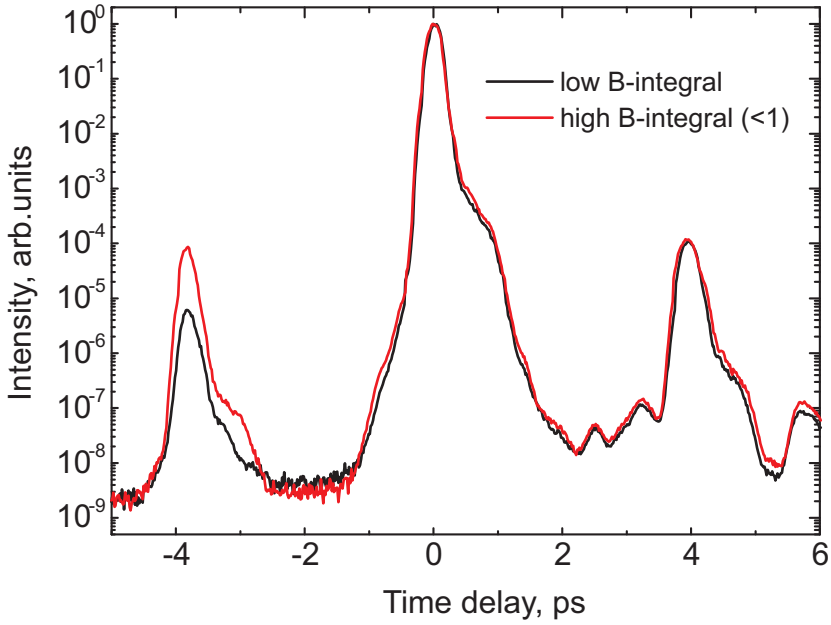

Figure 4.3: Impact of a high B-integral value in the Sequoia characterization of the measured temporal trace. The black curve corresponds to the impact of the characterization by the Sequoia only, while the red curve shows the mixed impact of both effects

sponding symmetric pre-/post-structures in the same way and with comparable relative amplitude as the reference post-pulse does. The accumulated nonlinear phase shift can impact the temporal contrast if coherent structures such as post-pulses exist in the pulse shape.

4.2.1 Generation of pre-pulses from post-pulses, numerical simulations

Modern numerical simulation methods are powerful tools which enable a better understanding of physical mechanisms. The described mechanism was simulated using the Miró software[113]. It is a reliable simulation tool developed by CEA, France to simulate the propagation of light in laser systems. It can be used to simulate many physical phenomena taking place in a laser system by solving the nonlinear Schrödinger equations [114]. It allows for a broadband optical pulse simulation with a pulse duration limited by the slowly varying envelope approximation ($\tau_{\mathrm{fwhm}} > 15$ fs) [115]. Version 5.27 of the Miró simulation software was used in this work. The Miró software was used to illustrate the processes relating to the generation of pre-pulses from post-pulses.

The considered optical scheme is shown in Fig. 4.4 consists of a laser source producing ultra-short light pulses ($\tau_{\mathrm{fwhm}} \approx 30$ fs). A post-pulse is then added and the resulting temporal profile is stretched. It then propagates through a nonlinear medium and is

afterwards re-compressed in a compressor with a similar configuration as the stretcher but with a dispersion of the opposite sign. Simulations are performed with parameters which reflect the most common stretcher/compressor configurations used in high field laser systems. A stretcher/compressor pair based on reflective diffraction gratings was considered. An incident angle of $\alpha = 41°$ and diffraction gratings with 1480 grooves per millimetre are common for many high-power laser systems. The B-integral value for the simulations was chosen to be $B \approx 0.35 \pm 0.05$ radians, representing the case of many amplifiers.

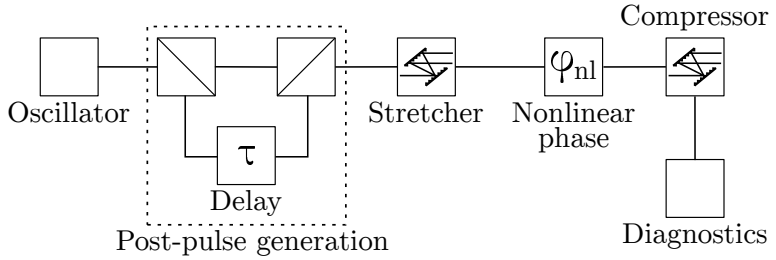

Figure 4.4: Scheme of the simulation. A part of the seed is split, attenuated, delayed and mixed with the major part to create a post-pulse. Then the pulse is stretched, the phase is changed, the pulse re-compressed and it is measured

The time delay of the post-pulse in the initial temporal distribution was varied as well as the distance between the diffraction gratings in both the stretcher and the compressor in order to change the duration of the stretched pulse. This was done to show the difference in the generated pre-pulses as a function of the delay and stretching factor. Both of these factors impact the interference pattern caused by the overlap of the stretched main pulse and the post-pulse and, as a result, significantly impact the intensity of the generated pre-pulses.

Figure 4.5 shows a number of curves related to different delays of the post-pulse. This figure shows the case, when the distance between the reflection diffraction gratings is about 40 cm. This is related to a stretched pulse duration of approximately $\tau_{\mathrm{fwhm}} \approx 100$ ps. These simulations show that the re-compressed pre-pulses, generated through the SPM process, can be chirped. It is visible that the generated pre-pulses, which have a comparatively long delay have a longer pulse duration than the main pulse. This is best seen in Fig. 4.6b, where the full width at half maximum is presented for each post-pulse delay. The chirp of the stretched pulse is not linear. Thus, it has different values of the main pulse and post-pulse. As the result, the pre-pulse appears to be slightly stretched after the dispersion compensation of the main pulse.

Figures 4.6a, 4.6c and 4.6d illustrate the evolution of the other parameters of the pre-pulses, such as the peak intensity and the relative temporal shift due to the above-mentioned nonlinear chirp. The distances between the gratings in the stretcher of 10,

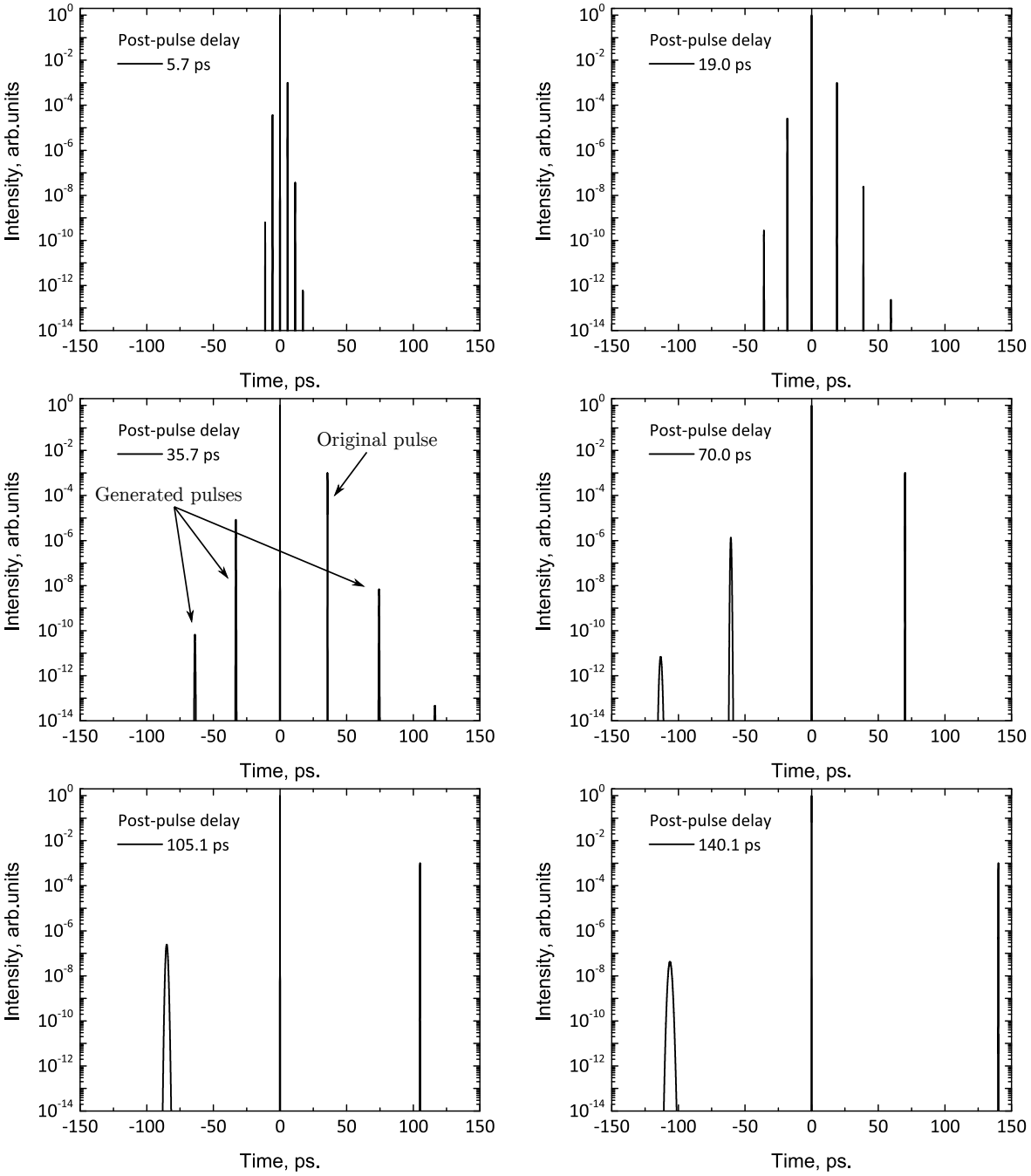

Figure 4.5: Results of the numerical simulation showing the evolution of the generated pre-pulse depending on the delay of the post-pulse. The intensity, duration of post-pulses as well as the accumulated B-integral value are the same for all presented curves

20, 30 and 40 cm correspond to stretched pulse durations $\tau_{\text{fwhm}} \approx 26$, 51, 77 and 100 ps respectively. Concerning the relative temporal shift, the distance from the main pulse and the generated pre-pulses is not the same as the distance between the main pulse and the corresponding post-pulse. The difference in their appearance in time can be positive or negative depending on the chirp parameters. The time difference between the delays of the pre- and post-pulses with respect to the main pulse is called the relative temporal shift. These values are presented in Fig. 4.6c. The figures demonstrate the complexity of the mechanism of generation of the pre-pulses. The relative time shift of the generated pre-pulses can exceed tens of picoseconds depending on the positions of the post-pulses.

It is worth noting that there are also pre- and post-pulses of higher order. In particular, the second and third replicas appear on both the leading and trailing edges of the temporal trace. The simulation was performed with only one post-pulse. However, a real system has many post-pulses which can interact with each other generating sets of multiple pre-/post-pulses. All of these factors create a complicated picture in which the complicity grows strongly with the number of peaks, making the analysis almost impossible. From this, it can be concluded that the number of post-pulses must be minimized for further improvement of the temporal contrast.

One can see that the generated pre-pulses are not transform limited and shifted towards the main pulse when the stretcher with the reflective diffraction gratings is used. The increase of the pre-pulse duration additionally decreases the its peak intensity.

Both (4.1) and (4.2) show that the energy of the generated pre-pulse depends on the relative intensity or energy of the post-pulse and the square of the accumulated nonlinear phase (B-integral value). The latter depend on the relative intensity of the stretched pulse (1.28). Thus, the envelope of the stretched pulse determines the efficiency of the process of energy transfer and, as a result, it determines the temporal region in which the pre-pulse may appear. The energy of the pre-pulses can be derived from the simulation. Since pre-pulses created as an internal double reflections were considered in [47], the pulse duration of the created post-pulse is similar to the pulse duration of the main peak. Thus, the relative intensity of the post-pulse is this case is the same as the relative energy. The only coefficients in (4.1) and (4.2) are different.

Let us have a look how the energy of the generated pre-pulse depends on the delay of the post-pulse. The red points in Fig. 4.7 show this dependence for the cases where there was a distance 20 cm ($\tau_{\text{fwhm}} \approx 51$ ps) and 40 cm ($\tau_{\text{fwhm}} \approx 100$ ps) between the reflective gratings. The black curves correspond to the normalized amplitude of the stretched pulse. One can see that the energy of the generated pre-pulses reproduce well the shape of the stretched pulse.

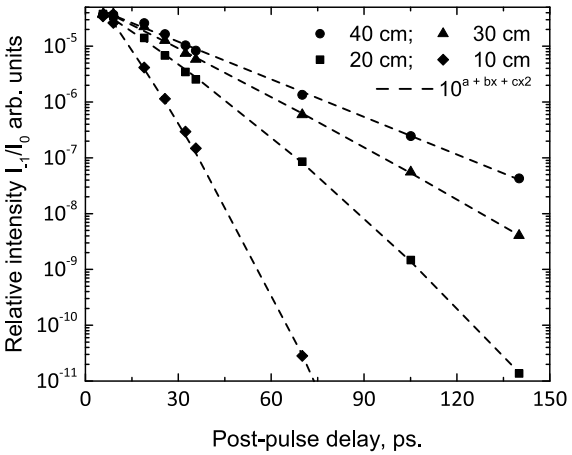

(a) Calculated dependence of the relative pre-pulse intensity on the post-pulse delay for different distance between the diffraction gratings

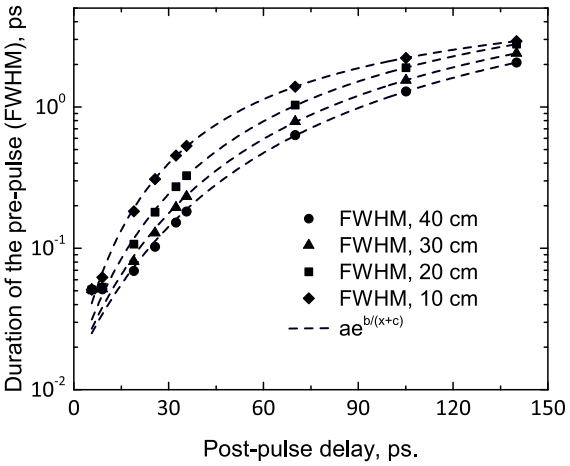

(b) Calculated dependence of the relative pre-pulse duration time on the post-pulse delay for different distance between the diffraction gratings

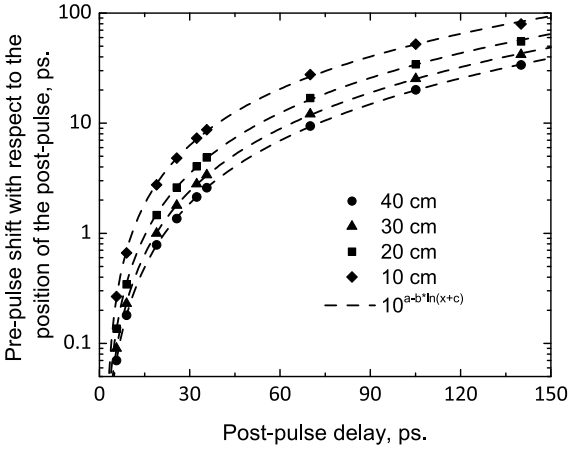

(c) Calculated dependence of the relative temporal shift (definition see text) on the post-pulse delay for different distance between the diffraction gratings

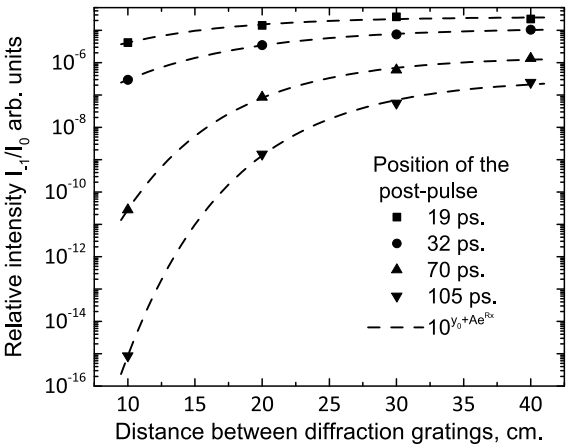

(d) Calculated dependence of the relative pre-pulse intensity on the distance between the diffraction gratings

Figure 4.6: Results of the numerical simulation showing the evolution of the generated pre-pulse on the properties of the post-pulse delay. The figures represent the cases when the seed duration is $\tau_{\mathrm{fwhm}} = 30\,\mathrm{fs}$, and the reflective diffraction gratings compressor at the incidence angle of 41° is used. The distance between the gratings is 10, 20, 30 and 40 cm. The accumulated nonlinear phase is $B \approx 0.35\,\mathrm{rad}$

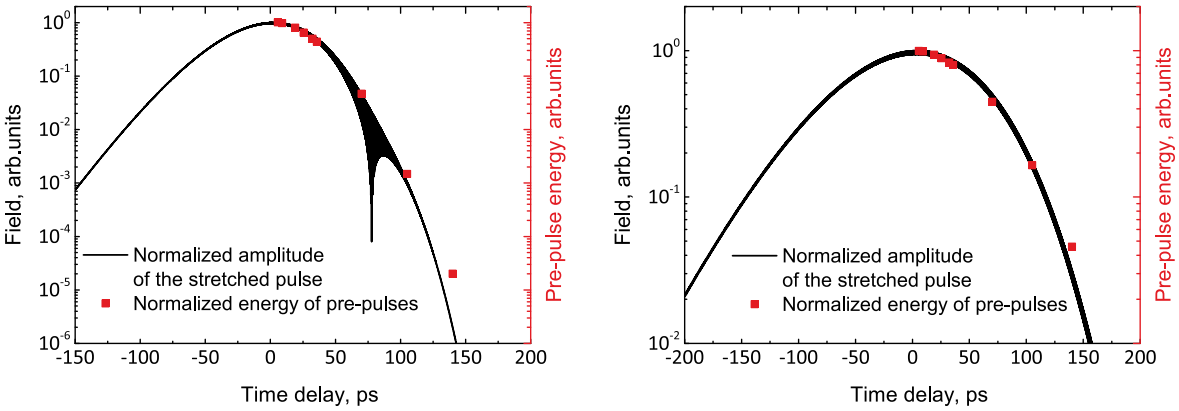

(a) 20 cm corresponding to a stretched pulse duration $\tau_{\mathrm{fwhm}} \approx 51\,\mathrm{ps}$)

(b) 40 cm corresponding to a stretched pulse duration $\tau_{\mathrm{fwhm}} \approx 100\,\mathrm{ps}$)

Figure 4.7: Dependence of the pre-pulse energy on the post-pulse delay derived from the simulation (red dots) and the amplitude of the stretched pulse (black line) for different distances between the reflective diffraction gratings in the stretcher

Since SPM is a third-order process, it appears logical that the pre-pulse energy depends on $|E|^3$, not $|E|^2$ (in the B-integral) as in equations (4.1) and (4.2). So, one can write an equation which takes into account the envelope of the stretched pulse

$$\left.\frac{E_{\mathrm{pre-pulse}}}{E_0}\right|_{\mathrm{z=L}} = \frac{1}{2}\left.\frac{E_{\mathrm{post-pulse}}}{E_0}\right|_{\mathrm{z=0}} \cdot B(z)^2 \sqrt{\frac{I_{\mathrm{stretched}}(t)}{I_{\mathrm{stretched}}(t=0)}} \tag{4.3}$$

where $I_{\mathrm{stretched}}(t)$ is the intensity of the stretched pulse at the time delay t of the post-pulse (not the corresponding pre-pulse), $E_{\mathrm{post-pulse}}/E_0|_{\mathrm{z=0}}$ is the relative energy of the post-pulse just after the post-pulse creation, and $E_{\mathrm{pre-pulse}}/E_0|_{\mathrm{z=L}}$ is the relative energy of the generated pre-pulse. The coefficient 1/2 derived from the simulations is close to 0.58 which is presented in [110] for a flat-top pulse profile.

Finally, it is worth checking the quadratic dependence of the energy of the first pre-pulse on the B-integral values. In these simulations, a single post-pulse was added to the temporal profile, as in the previous scenarios. The seed energy was then varied to change the B-integral value and the resulting curves are presented in figures 4.8a and 4.8b. The relative energy of the first pre-pulse and post-pulse are shown in figures 4.8c and 4.8b, respectively. It can be seen that the energy of both pulses depend on the B-integral value. The solid line in Fig. 4.8c is calculated using equation (4.3). It fits well the simulated data below value 1. The observed discrepancy between equation (4.3) and the simulated dots can be the explained by simplicity of the equation which cannot take into account the complex interaction while the pulse propagates.

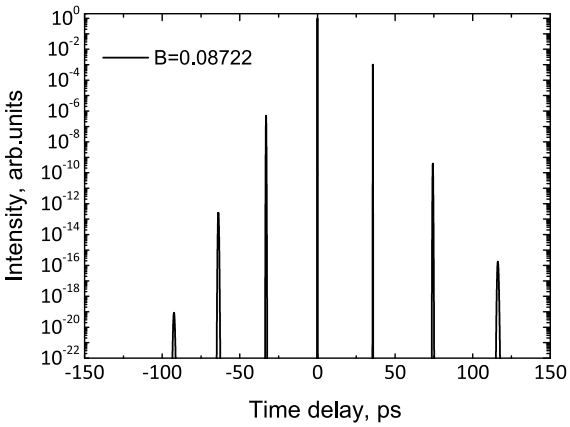

(a) Simulated temporal trace with a post-pulse of a relative energy 10^{-3} at 35.7 ps and B-integral = 0.8722 rad

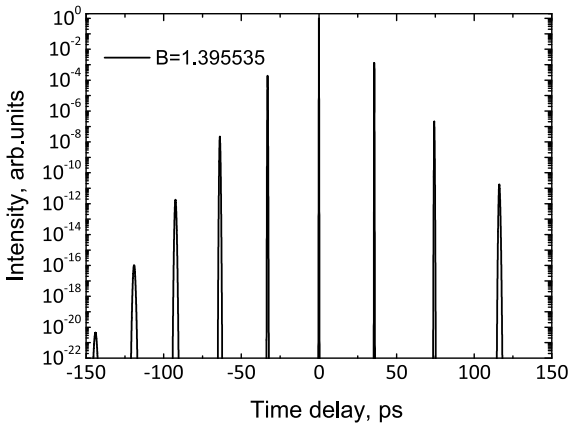

(b) Simulated temporal trace with a post-pulse of a relative energy 10^{-3} at 35.7 ps and B-integral = 1.3955 rad

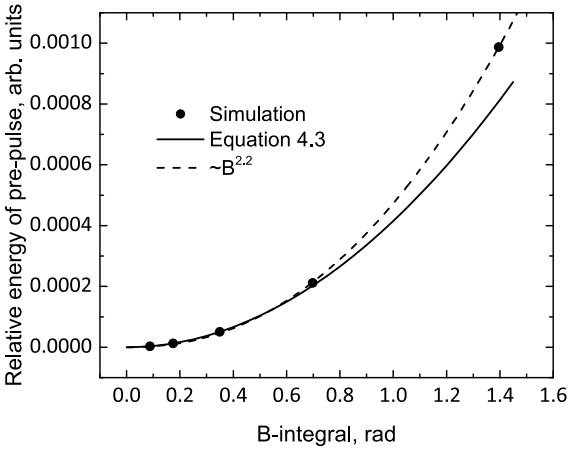

(c) Dependence of the first pre-pulse energy on the accumulated nonlinear phase. Dots represent the simulated data, the solid line shows the energy calculated using equation 4.3 and the dashed curve represents a fit with the power function $C_1 B^{2.2}$

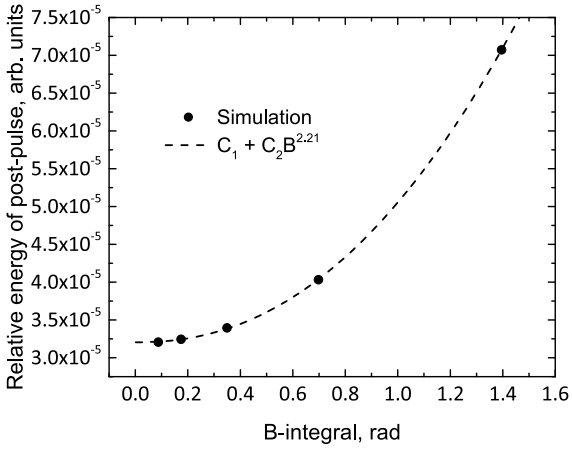

(d) Dependence of the first post-pulse energy on the accumulated nonlinear phase. Dots represent the simulated data and the dashed curve represents a fit with the power function $C_1 + C_2 B^{2.2}$

Figure 4.8: Results of a numerical simulation showing the evolution of the energy of the generated pre- and post-pulses on the B-integral value accumulated between the post-pulse appearance and the re-compression. The case of two parallel diffraction gratings is presented. The distance between the gratings is 40 cm corresponding to a stretched pulse duration $\tau_{\text{stretched}} \approx 100$ ps

4.3 Investigation of the observed asymmetry of the main pulse

One can notice that the temporal traces presented in the figures 4.2 and 4.3 show an asymmetry of the main pulse as well as the pre- and post-pulses. The temporal shape looks as if the main pulse and other pulses *"sit"* on a second longer and lower intensity pulse shifted by half a picosecond. This is clearly visible in Fig. 4.9. Moreover, it follows from the figures 4.2 and 4.3 that this shifted pulse remains insensitive to the changes of the accumulated nonlinear phase which can indicate their incoherent nature.

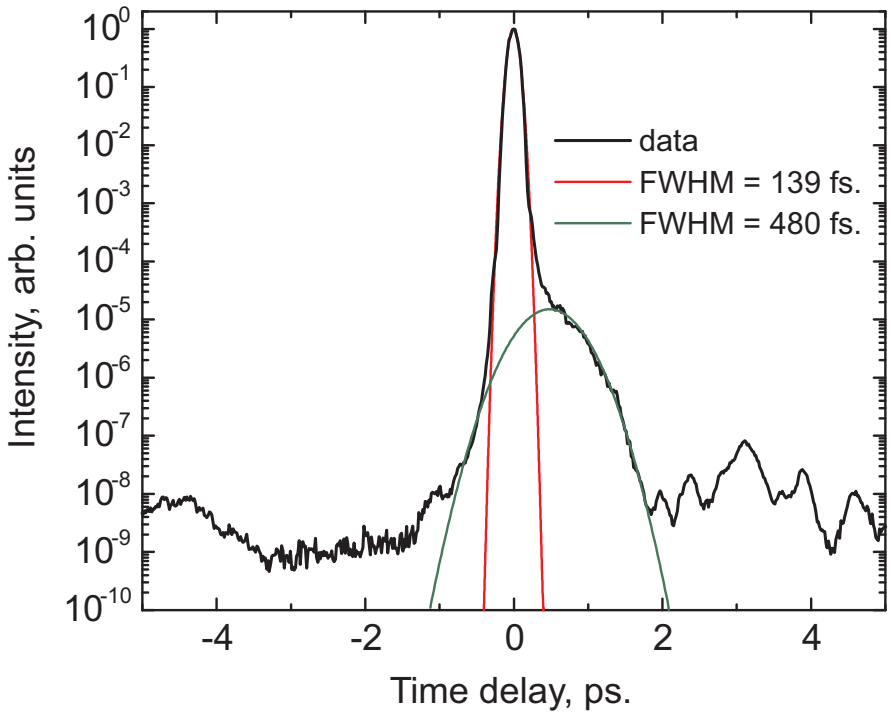

Figure 4.9: Pedestal of the main peak observed in the cases when the compressor is based on bulk glass. The experimental data (black curve) with the peak fitted by the Gaussian function (red curve) and the long Gaussian pedestal

If we get back to the comparison of stretchers presented in section 3.3, one can see in Fig. 3.5 that the asymmetry is visible in the case of stretchers with a transmission diffraction grating and prisms only. These two configurations show a shorter leading front compared to the trailing front. This is not the case for the reflection diffraction grating.

It is important that the stretchers based on the transmission diffraction grating and the prisms use the same compressor based on SCHOTT SF6 glass. In fact, the second pulse exists only in the case of the compressor based on bulk glass. The optical path in the bulk compressor has a significant value ($\approx 40\,\mathrm{cm}$). One can assume an incoherent

scattering inside the bulk glass compressor. This explains the delayed nature of the *"hump"* and its insensitivity on the accumulated nonlinear phase.

It is well-known that optical defects are unavoidable in transparent optical elements and always need to be taken into account. Optical glasses are classified by several classes of purity and each class of purity determines the number and sizes of the defects, such as bubbles. Table 4.1 presents information about the classes of SCHOTT glass used for the bulk compressor.

Bubble class	Standard	VB	EVB
Maximum cross section in mm^2 per 100 cm^3 of glass volume	0.03	0.02	0.006
Maximum quantity per 100 cm^3	10	4	2

Table 4.1: Bubble classes of SCHOTT class reflecting the purity of the material. VB – increased bubble selection, EVB – extra increased bubble selection) [116]

If the assumption of the scattering origin of the *"hump"* is correct, then the upper limit of the scattered light can be estimated using Table 4.1 and compared with the obtained result. The diameter of the laser beam in the bulk glass compressor is approximately $\approx 3\,cm$ and thus, the area is $\approx 7\,cm^2$. The path length inside the glass (SCHOTT SF6) compressor is $4 \times 10 = 40\,cm^3$. On the other hand, for standard SCHOTT glass according to Table 4.1, the area of the bubbles is approximately $\approx 8.25 \times 10^{-4}\,cm^2$. The ratio of the area of the bubbles to the beam is approximately $\approx 8.25 \times 10^{-3}/7 = 1.2 \times 10^{-4}$. This means that, in the case of the stretcher with the transmission diffraction grating, the level of scattered light is below 10^{-4} of the peak intensity of the main peak. This level can be slightly higher in the case of the prisms-based stretcher. The prisms (OHARA Glass) in the stretcher will contribute to the scattering. Indeed, the trailing pedestal in the case of the prisms-based stretcher is higher than in the case of the transmission grating (Fig. 3.5).

4.4 The problem of the long pedestals lying on the both sides of the pulse

In the previous section 4.2 we have learned the diagnostics which allow coherent parts of the pulse shape to be distinguished. Here I am going to discuss an application of this new diagnostics to our investigation and the problem of the appearance of a long pedestal in front of the main pulse. As was mentioned in 3.3, it is commonly assumed

[99, 101], that this pedestal is associated with the design of a stretcher. I am going to present an alternative point of view about the origin of this parasitic pre-pedestal. I will show that the pre-pedestal is generated by the post-pedestal lying behind the main pulse. Then I will try to identify the source of the post-pedestal and discuss the possible reasons of its appearance.

4.4.1 Investigation of the pre-pedestal appearing at delays of tens of picoseconds

The experiments showing generation of a pre-pulse presented in section 4.2 were performed with the stretcher delivering a low stretching factor. The pulse duration in that case is approximately 10 ps. The stretching factor and thus the stretched pulse duration delivered by the stretcher with the reflective diffraction gratings is one order higher ($\sim$ 100 ps). This has motivated an experiment, as described in 4.2, using the configuration with the reflective diffraction gratings. The B-integral of the system was increased by several thick glass plates installed in the 1:1 telescope before the re-compression stage. The resulting curves at low and comparatively high B-integral values are presented in Fig. 4.10.

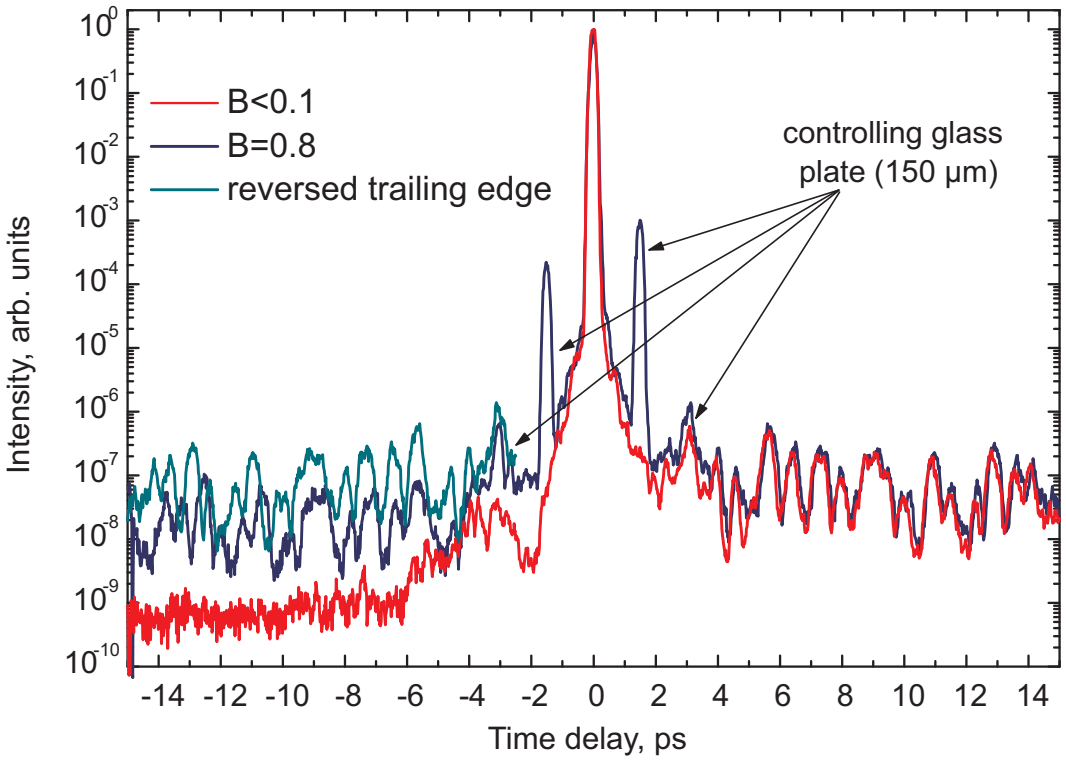

Figure 4.10: Results of the variation of B-integral value at longer stretched pulse duration in the configuration when the stretcher and compressor are based on the reflection diffraction gratings

The red curve in Fig. 4.10 is measured without the thin glass plate and at a low B-integral value. The blue curve represents the shape for a high B-integral value. The introduced glass, and thus the value of the B-integral, corresponds to approximately B ≈ 1. The blue curve shows that the temporal shape of the main pulse front is changed and a ragged pre-pedestal has appeared. Moreover, the structure of the pre-pedestal looks similar to the post-pedestal behind the main pulse. The cyan curve in Fig. 4.10 is mirror image of the ragged post-pedestal and is used to check the similarities between these pedestals. It can be seen that the blue curve repeats well the shape of the cyan curve at low values of the delay from the main peak and shows a slight temporal shift at longer time delays. The shape is similar, however the timing of the structures increasingly changes further away from the main peak.

The pre-pedestal at a high value of the B-integral can be explained in a similar way as the pre-pulses generated through interference and SPM processes. Moreover, the observed temporal mismatch between the curves in Fig. 4.10 indicates a nonlinear (from high-order dispersion) chirp of the main pulse. A similar shift was observed in [110] for single pre-pulses, as well as in the simulations in 4.2.1. This leads to the important conclusion that the ragged post-pedestal lying behind the main peak is coherent to the main peak. This coherence is required for the interference involved in the described mechanism.

It is obvious that the duration and the shape of the stretched pulse directly limit the duration of the generated pre-pedestal. It is also apparent why no corresponding pre-pedestal was observed in the experiments with other types of stretcher/compressor configurations. The stretched pulse was substantially shorter in the case of the transmission diffraction grating ($\sim 10\,\mathrm{ps}$). Consequently, the intensity of the stretched pulse decreases faster with increasing the time delay compared with the case where the reflective gratings are used. This, in turn, impacts the efficiency of the generated pre-pedestal as follows from equation (4.3). It also explains the difference demonstrated in [99, 100]. In the latter, the temporal trace measured in the configuration with a transmission diffraction grating-based stretcher has shown a shorter pre-pedestal and leading front of the main pulse compared with the stretcher based on a reflective diffraction grating. The authors of [99, 100] explained the worse temporal contrast in the case of the reflective diffraction gratings-based stretcher by the roughness of the optical surfaces of the reflective diffraction gratings and a parasitic scattering inside the stretcher. At the same time, the stretching factor provided by the stretcher with transmission diffraction grating is much smaller compared with the reflective diffraction grating, and the results presented in [99, 100] can be treated in the way presented above: the shorter pre-pedestal is caused by the shorter duration of the stretched pulse.

The reduction of the stretched pulse duration leads to the shortening the pre-pedestal which is beneficial. On the other hand, this also leads to an increase of the accumulated nonlinear phase and, hence, an increase of the pedestal amplitude. However, the stretched pulse shape practically limits the area where the pre-pedestal gets generated. In addition, the amplitude of the generated pre-pedestal is up limited by the amplitude of the pre-pedestal at the corresponding delay. Thus, depending on the laser system and the particular requirements for the temporal contrast, the duration of the stretched pulse needs to be optimized. However, too short stretched pulses significantly increase the risk of self-focusing leading to optical damage of the amplification crystal and other optics.

In principle, the pre-pedestal, as well as the post-pedestal can be filtered out using available nonlinear filtering methods. However, it will be shown in the following that the amplification cascades also generate a post-pedestal and then a pre-pedestal. Thus, temporal filtering, excepting the plasma mirror, cannot help in avoiding the generation of the pre-pedestal. In the following paragraph we attempt to understand the nature of the post-pedestal aiming to cancel the conditions of its formation.

Measurements with all available stretcher/compressor pairs (Fig. 4.11a) indicate that the temporal structures in the post-pedestal are very stable and match well, with the noted exception of a few peaks which stem from reflections from the optical elements within the transmission grating-based stretcher. The post-pedestal neither depends on the stretching factor nor on the dispersive element used in the stretcher. Moreover, all available master oscillators with different dispersion compensation schemes were compared, yielding again nearly the same shape of the post-pedestal. Finally, the Ti:Sapphire crystal in the amplifier was also changed to a crystal from a different batch with a slightly different doping concentration and this also did not impact the structure of the post-pedestal.

To avoid possible artefacts due to the diagnostics, the measurements were repeated using a home-made third-order cross-correlator, which provides a higher temporal resolution but a lower dynamic range. Figure 4.11b shows that the home-made cross-correlator reproduces the observed structures in the post-pedestal, showing additional finer substructures. The curves are shifted in the y direction for better comparison. From all of these experiments it can be concluded that the trailing pedestal does not depend on the stretcher/compressor configuration, the amplifier, the diagnostics or on the dispersion compensation type in the master oscillator. It is worth noting that the stretched pulse duration in the case of the transmission grating-based stretcher and the stretcher with prisms is low compared with the case of the reflective diffraction grating-based stretcher. The orange curve in Fig. 4.11a shows the approximate shape for the

stretched pulse for the cases of stretchers with prisms and the transmission diffraction grating. If the observed post-pedestal appeared as an artefact of the CPA, it would definitely be shorter than the stretched pulse duration. It is seen that even after 70 ps, the observed pedestal is still very stable and reproducible in all three configurations of the laser system.

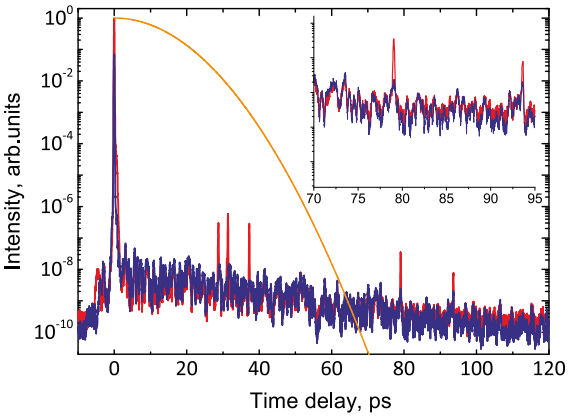

(a) The measured long post-pedestal, which is longer than the stretched pulse duration

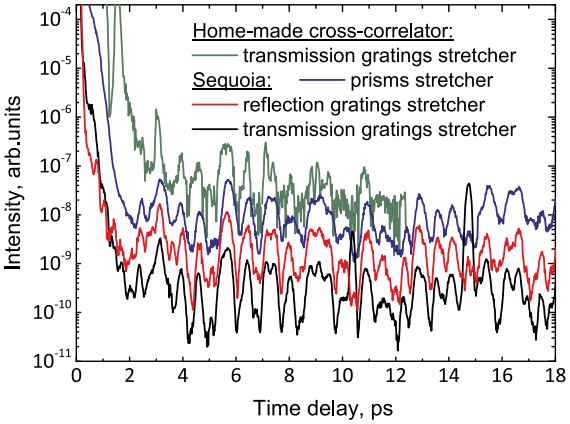

(b) Comparison of post-pedestals measured in different stretcher/compressor configurations. The temporal traces are shifted vertically for a better comparison

Figure 4.11: Structure of the post-pedestal, measured with all tested stretcher/compressor configurations

The post-pedestal starts at a relative level of $\sim 10^{-8}$-10^{-7} with respect to the maximum of the main peak. This level depends on the particular laser system, the re-compression of the pulses and the accuracy of the characterization. The ragged structure, as visible in Fig. 4.11, identically reappears for different configurations of the Ti:Sapphire system. It has a very stable and reproducible shape with an intensity decay which scales approximately as $P(t) \sim \exp(-t/30)$, where t is the time in picoseconds.

In order to analyse this situation, the laser system needs to be simplified as much as possible. However, there is a significant problem if the CPA stage is excluded and the work is only performed with the master oscillator. Currently, there is no available characterization device which allows the temporal contrast of a master oscillator with sufficient dynamic range to be characterized. This is associated with the low pulse energy at the exit of a Kerr mode-locked master oscillator. However, this measurement has in fact already been performed at Laboratoire d'Optique Appliquée (LOA) [117]. Their results were published more than 15 years ago [117]. With the consent of the authors of [117] I present their result here in the red curve in Fig. 4.12. The measurement was performed at LOA using a home-made cross-correlator. The characterized master oscillator is based on a Ti:Sapphire and is commercially available from Femtolasers.

The black curve shows the regular temporal shape of our CPA system.

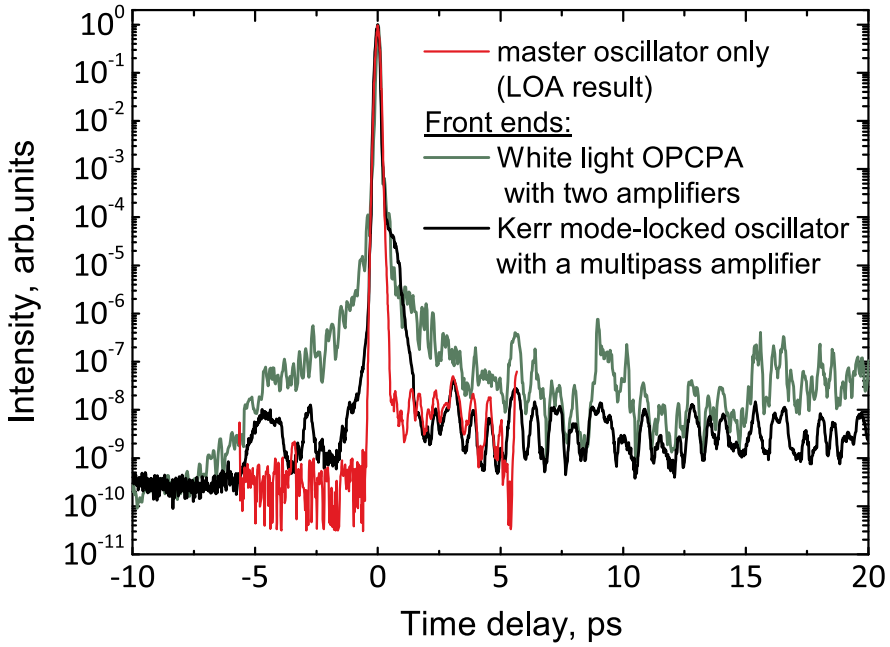

Figure 4.12: Cross-correlation trace of a master oscillator investigated at LOA 15 years ago [117] (red curve) in comparison with the investigated front-end (black curve) and an OPCPA laser system without a Ti:Sapphire-based oscillator but with Ti:Sapphire used in an amplifier (green curve)

There is a perfect match between the ragged temporal structures of both shapes. This indicates that the long trailing pedestal is already present in the radiation of Ti:Sapphire Kerr mode-locked oscillators. Moreover, no triangular pedestal around the main peak is seen indicating that the triangular pedestal appears after the master oscillator in the CPA stage.

The observed trailing pedestal has several specific features, including coherence with the main pulse (different from ASE), a ragged character and a duration exceeding $\sim$ 100 ps, where it reaches the detection limit. The pedestal appears independently of the stretching arrangement employed. In multi-terawatt and particularly PW Ti:Sapphire laser systems, where the value of the B-integral cannot safely be kept below 1 rad, the post-pedestal unavoidably leads to the appearance of the mirror symmetric pre-pedestal. An analysis of the literature on high dynamic range characterizations of different Ti:Sapphire high peak power laser systems [76, 101, 100, 118, 119, 120, 121] leads to in the conclusion that similar trailing pedestals have been observed in all Ti:Sapphire CPA laser systems.

Therefore, it can be concluded, based on the literature [117] and the experimental data, that the coherent post-pedestal is already present in the output of the Kerr-lens mode-locked master oscillator. Moreover, the picosecond structure does not depend

on a particular realization. In order to resolve this problem, it appears reasonable to suspect that the trailing pedestal is generated inside the Ti:Sapphire gain medium or that it may occur due to a global factor, such as the intrinsic medium – air, which is a nonlinear medium for the laser pulse to propagate through.

It is important to mention that most likely our cross-correlator does not allow good resolution of the structures in the post-pedestal. The period of the oscillations in the ragged pedestal is about the temporal resolution of the Sequoia cross-correlator, meaning that the ragged pedestal may have more fine structure which cannot be measured with the currently available high-dynamic range characterization methods. Spectral and temporal analysis may shed some light on possible reasons which lead to post-pedestal generation. The further analysis is based on the assumption that the real temporal shape of the post- and pre-pedestals is not far from the measured curves, even if the structure of the pedestals are not fully temporally resolved.

4.4.2 Investigation of a parametric-based front-end as an alternative to the Ti:Sapphire-based oscillator

Some issues regarding the temporal contrast degradation could be potentially resolved by using a new type of a front-end laser system, in which no Ti:Sapphire-based master oscillator is used. One of these issues is the generated post-pedestal which plays a key role in limiting the temporal contrast on the picosecond scale.

The new type of front-end uses an Yb-fibre laser instead of a classical mode-locked Ti:Sapphire-based oscillator. This is a source of comparatively long femtosecond pulses of $\tau \sim$ 200-300 fs at wavelength of $\lambda_0 =$ 1030-1040 nm [122]. The fibre-based laser delivers the best possible energy stability of all available ultrafast laser sources. A passive Carrier Envelope Phase (CEP) stabilization technique based on a parametric process including broadband generation is used [123, 124]. The scheme can deliver CEP stabilized ultra-short pulses of a few optical cycles at a wavelength of $\lambda_0 = 1.6\,\mu$m. A second harmonic generation stage is employed to transform this into light at $\lambda_0 = 800$ nm. The second harmonic generation additionally improves the temporal contrast. Its resulting temporal shape in this case is the square of the initial shape (if the temporal trace is normalized to its maximum). This trick allows optical pulses of a few cycles of the optical field with a good temporal contrast to be achieved.

The significance of this scheme for our investigation is the absence of a Ti:Sapphire-based master oscillator. This allows for a check regarding whether the ragged post-pedestal appears in amplification cascades or only in a Ti:Sapphire based master oscillator. It is the principal moment which shows the severity of the generated post-pedestal problem. If the pedestal is generated in a master oscillator only, the seed can be gener-

ated with a Ti:Sapphire-free source. The described OPA-based front-end with a fibre laser is a good option. However, if the post-pedestal is generated in a Ti:Sapphire-based amplifier, it is a principal limiting factor for the temporal contrast on the picosecond time scale for high-power Ti:Sapphire-based CPA laser systems.

The fibre-based front end can help to clarify the situation. However, the pulse energy at the exit of a such front-end is too low for the high-dynamic range characterization using available devices. This requires an additional amplifier, which includes a Ti:Sapphire crystal. However, the system does not include a conventional master oscillator with a Ti:Sapphire, which enables an indirect conclusion if an amplifier with Ti:Sapphire generates the post-pedestal.

A measured temporal trace of such a system, which contains the ragged post-pedestal, is shown in Fig. 4.12 by the green curve [109]. Even with the slightly different relative intensity, it reproduces the shape of the post-pedestal presented in the other curves obtained with a conventional master oscillator based on a Ti:Sapphire crystal. This result means that the post-pedestal is generated in a Kerr mode-locked master oscillator but also by Ti:Sapphire crystals in amplifiers. Another indication for the origin of the post-pedestal during amplification in Ti:Sapphire amplifiers is the additional measurement performed at the MBI 100 TW Double-CPA High-Field Laser system (HFL) [76]. The laser system used in this investigation is an exact copy of the HFL front-end with the same level of ASE and the post-pedestal. XPW nonlinear filtering, installed in the HFL, reduces the ASE, as well as the post-pedestal, by four orders of magnitude. Despite the temporal filtering applied, the measurements at the exit of the laser chain clearly show the recovery of the post-pedestal level in amplifiers (see Fig. 4.13). There is a good match with one of the temporal traces from the front-end, which does not have any filtering.

A Ti:Sapphire-free front end does not allow for the generation of the post-pedestal to be avoided. Moreover, if a temporal filtering technique is applied after the front end, the ragged pedestal will appear again in the following amplification cascade. As the major part of the B-integral is usually generated during the last two passes through the crystal in an amplifier, nonlinear temporal filtering will not help to avoid the generation of the pre-pedestal. The only way to avoid this is to find the physical reason for its generation and to cancel or significantly reduce it.

4.4.3 Investigation of a possible impact of air on the coherent post-pedestal

There are several possible reasons for the ragged trailing pedestal. One possible reason is a Raman effect in the air inside the laser beam path, including the paths inside the

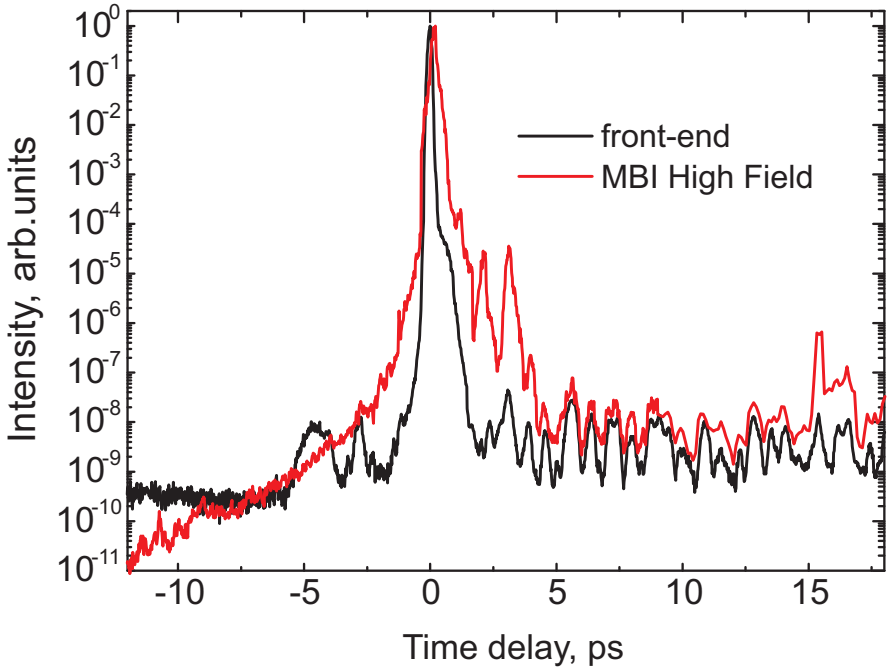

Figure 4.13: Temporal contrast of the MBI High Field laser system (red curve) and the temporal contrast of the front-end (black curve)

oscillator and the amplifier. Intense ultra-short laser pulses of high intensity may induce rotations of N_2 and O_2 molecules [125, 126], which make up 99 % of the composition of air. This high intensity can be reached while focusing the seed in a crystal inside the cavity of a master oscillator. The Raman effect influences the refractive index of the air medium. A mixture of two kinds of molecules can create a complex modulation of the refractive index in the section following the main pulse. The characterization process smoothens the measured temporal trace through convolution with the temporal response function of the Sequoia cross-correlator. The resulting temporal shape can have a periodicity comparable to the measured temporal traces.

To validate this assumption, the pulses in the trailing pedestal were checked to see if they exhibited a periodic structure. It is worth splitting the part behind the main peak pulse in the temporal trace and to try to find regular frequencies by using the Fourier transform method. The temporal trace was clipped just after the main peak and the slow decay of the post-pedestal was compensated by dividing by an exponential function presented in Fig. 4.14a. The compensation of the slow decay is necessary otherwise the coherent structures with relatively short delay contribute more to the spectrum compared with the structures with long delays. The resulting temporal trace is presented in Fig. 4.14a. The Fast Fourier Transform (FFT) was calculated after manipulation of the temporal trace. Several FFTs with different parameters were calculated and compared. They did not show any stable and reliable peaks. One of

the resulting spectra is shown in Fig. 4.14b.

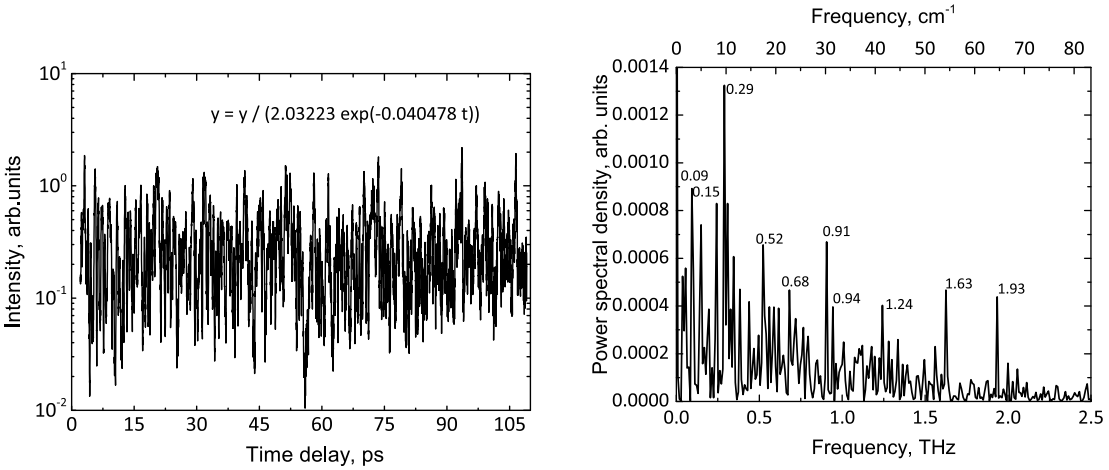

(a) Modified pulse shape with only post-pedestal. The slow decay is compensated in order to get more information about the observed periodical structures

(b) Fourier Transform power spectrum of the modified temporal trace following the main pulse

Figure 4.14: The modified post-pedestal and its spectrum. The spectrum does not show unique frequencies

In the case of rotations of the molecules in air it would have a strict periodicity, at least for a few periods of the molecular rotations. This means that the molecules of air do not play a significant role in the ragged post-pedestal generation. The absence of Raman-induced artefacts due to air has been verified by experimentally filling the oscillator, compressor, cross-correlator and amplifier with argon gas. Argon is an atomic gas and thus has no molecular rotations. A constant gas flow was implemented to maximize the possible impact of the gas. The proportions of the molecules of N_2, O_2 and argon were significantly changed. This should change the measured temporal traces if the air medium was involved. The Sequoia traces, obtained with argon gas, are presented in Fig. 4.15.

The curves in Fig. 4.15 were measured over a period of one day. The plot legend reflects the time at which a certain curve was measured. The experiment was started at regular conditions. Then, the argon flow was turned on and a few more curves were measured. After that, the flow was switched off, the cavity opened and the system ventilated for the final measurements. The amount of O_2 and N_2 differed significantly in all three stages: before pumping the argon, with the argon and after the oscillator cavity ventilation. However, despite a few minor changes in the two peaks between 2 and 3 ps in the trailing edge, no substantial impact of the atmospheric gas was observed. Moreover, the observed difference was not reproducible. Another important detail is that the peak at around 3 ps started growing after the ventilation of the cavity.

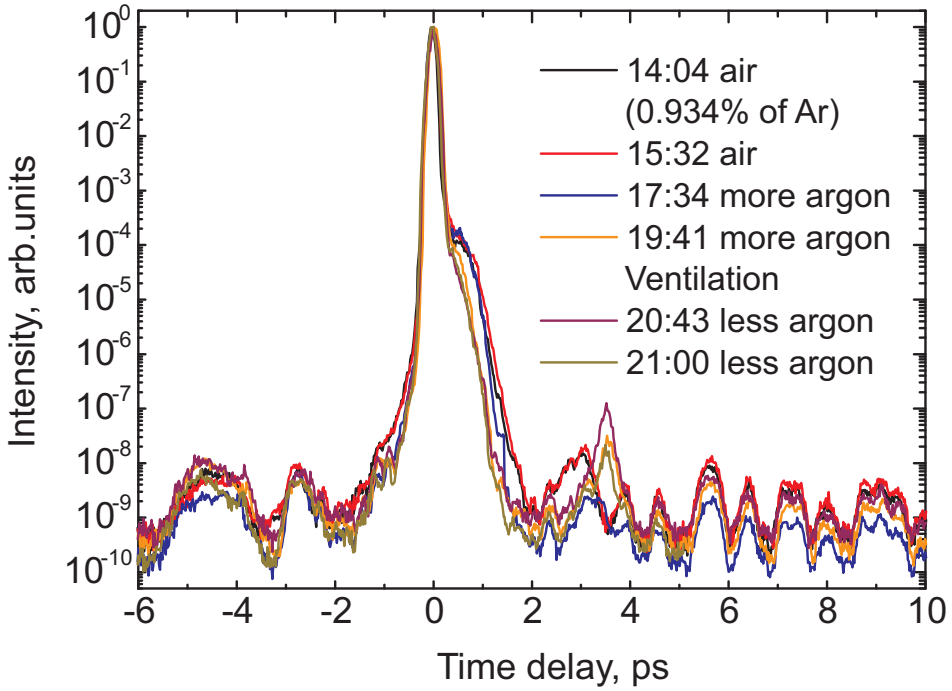

Figure 4.15: The influence of argon gas in the master oscillator, compressor and Sequoia cross-correlator on the measured temporal traces. Curves of different colors show the evaluation of the spectral shape on the pumping and the ventilation procedures

It is visible in Fig. 4.15 that, at certain stable conditions, with argon or without, the temporal profile is well reproducible. The only transition process for which the gas flow changes introduces the observed difference in a very limited time range (at around 3 ps). This experimental result may serve as indirect confirmation that air is not responsible for the generation of the post-pedestal.

4.4.4 Raman effect in sapphire as an explanation of observed pedestal

The Raman effect can be involved into the process of the post-pedestal generation, even, if the post-pedestal does not occur due to the Raman response of air. It is reasonable to assume that internal vibrations of the Ti:Sapphire crystal itself can be the mechanism which leads to the appearance of the post-pedestal. The Ti:Sapphire active medium is a sapphire crystal which is doped with Ti^{3+} ions. The doping level is comparatively low and the host crystal – sapphire, known as corundum or aluminium oxide Al_2O_3 – determines the Raman properties of the crystal. The generation of the post-pedestal might be associated with vibrations of the crystal lattice of a sapphire crystal.

An aluminium oxide crystal forms the basis of various laser crystals, for instance,

the most well-known laser crystal, ruby (Cr^{3+}:Al_2O_3). It can be found in nature as a mineral, called corundum, or, more rarely as sapphire or ruby crystals. Of course synthetic sapphire crystals are used in laser systems. This is associated with special requirements of optical quality and the absence of unwanted chemical impurities. The latter may significantly change the optical properties of sapphire. Moreover, chemical impurities, such as chromium (Cr) and titanium (Ti) ions allow the optical properties of the crystal to be manipulated.

Ti:Sapphire-based lasers are vibronic lasers where the lattice vibrations or phonons play a key role in the light amplification process [44, 127, 128, 129]. The internal vibrations of the crystal lattice play an important role in a formation of the broadband emission spectra. If it is assumed that phonons in a Ti:Sapphire crystal play a role in the process of generation of the post-pedestal, certain oscillation modes must be supported by the crystal lattice of the Ti^{3+}:Al_2O_3.

There are several techniques which allow for the study of atomic dynamics or vibration modes of materials. The most used techniques are infrared (IR) spectroscopy and Raman spectroscopy [130]. Phonon modes contribute to the IR or Raman processes under different conditions [130], which are complimentary in most cases. This means that a phonon mode will be active in either IR or Raman measurements. Here, we will consider Raman spectroscopy only. This is associated with an opportunity to measure a sample in a Raman spectrometer in an interesting frequency range.

Raman spectroscopy is a spectroscopic method which uses the Raman scattering effect, which is based on the inelastic scattering of incident light on vibrating molecules. The resulting light has a frequency shift from the frequency of the incident light. The frequency shift yields information about the vibration mode of the molecules. Usually, the vibration modes are incoherently excited by an argon or helium-neon (He:Ne) laser beam in a Raman spectrometer. The resulting scattered light from the sample is passed through a notch filter, suppressing the frequency of the exciting beam, and is then analysed by a spectrometer.

It can be assumed that the periodicity in the observed post-pedestal is a representation of a Raman mode and thus with respect to Fig. 4.14b, the frequency of the phonons must be in the range 0.3-1.9 THz which corresponds to 10-64 cm^{-1} (see the top scale in Fig. 4.14b). The related Raman wavenumbers are calculated using a simple equation (4.4).

$$\tilde{\nu} = \frac{1}{\lambda} = \frac{\nu}{c} \tag{4.4}$$

The Raman scattered light has a low intensity level compared with the incident light. The initial laser beam must have as narrow a spectral bandwidth as possible as a frequency shift is being measured and the filter for separating the scattered light con-

taining shifted frequencies must have a steep enough spectral function to measure small shifts. The Raman shift is usually measured in cm^{-1} units and the measured Raman wavenumbers usually lie in the range starting from $\sim 100\,\mathrm{cm}^{-1}$ to a few thousands of cm^{-1}. Usually, frequencies below $100\,\mathrm{cm}^{-1}$ are difficult to detect due to the small difference between the frequency of the incident light and the frequency of the Raman scattered light. It is necessary to suppress significantly the signal from the laser line.

Equation (4.5) is used to calculate the Raman shift. It includes the excitation wavelength λ_0 and the shifted wavelength λ of the light, registered by the spectrometer.

$$\Delta\omega = \frac{1}{\lambda_0} - \frac{1}{\lambda} \tag{4.5}$$

According to (4.5), a $100\,\mathrm{cm}^{-1}$ Raman shift corresponds to the wavelength $\lambda \approx 636.8\,\mathrm{nm}$ when using a laser with an excitation wavelength of $\lambda_0 = 632.8\,\mathrm{nm}$. In case of a $50\,\mathrm{cm}^{-1}$ shift, the spectrometer must detect a wavelength of $\approx 634.8\,\mathrm{nm}$; a $10\,\mathrm{cm}^{-1}$ shift corresponds to $\approx 633.2\,\mathrm{nm}$. It is difficult to construct a filter with a sufficiently steep spectral function and high attenuation coefficient. This is the main reason why measurements of frequency shifts below $100\,\mathrm{cm}^{-1}$ require special filters, which have a very steep spectral edge and a high suppression coefficient. Modern filtering methods allow for the measurement of Raman spectra starting from $8\,\mathrm{cm}^{-1}$. Special ultra-low frequency filters [131] or reflective diffraction grating-based monochromators [132] can be used for that purpose, but these devices are usually extremely expensive.

There is another issue with Raman characterization of the Ti:Sapphire crystal. The luminescence line of the crystal is quite broad and in the case of using a He:Ne gas excitation laser, the Raman shifted wavelengths will be in the spectral range of the luminescence line. It is impossible to resolve the resulting Raman lines due to the strong luminescence of the crystal.

However, as was mentioned above, the host crystal is sapphire, and titanium ions are a trace component. It is thus reasonable to assume that the Raman modes of a Ti:Sapphire crystal will not be significantly different to modes of a synthetic sapphire. Titanium ions may slightly change the position or the intensity of the lines or introduce a few more lines, but they will not change the spectral pattern of the sapphire. This leads to the conclusion that the Raman spectrum of a synthetic sapphire crystal of similar quality and purity is similar to a titanium-doped sapphire Raman spectrum.

A series of Raman measurements have been carried out using a LabRAM HD Evolution spectrometer (HORIBA). The spectrometer has an Ultra-Low Frequency (ULF) Raman Module [131] to measure spectra shifts down to $10\,\mathrm{cm}^{-1}$. A He:Ne (wavelength $\lambda = 623.8\,\mathrm{nm}$) laser is used as the excitation source. Unfortunately, the ULF Raman

module is strongly related to a particular wavelength and thus there is no opportunity to use a laser with a shorter wavelength.

Figure 4.16a shows the Raman spectrum of a conventional sapphire substrate used for scientific investigations. It clearly shows several peaks, which match with the Raman modes of sapphire, presented in the literature [133, 134]. The peaks are accompanied by a huge background, which is associated with chemical impurities in the substrate. Figure 4.16b demonstrates the reference spectrum of silicon, which is used for the calibration process of the LabRAM HD Raman spectrometer. The inset in Fig. 4.16b shows the magnified part of the spectrum in the range up to $200\,\mathrm{cm}^{-1}$. This plot is presented here to show the artificial nature of the peaks below $10\,\mathrm{cm}^{-1}$ and to prove that the weak peak near $50\,\mathrm{cm}^{-1}$ is not a measurement artefact.

Figure 4.16c shows the Raman spectrum for a clean sapphire substrate without the background signal. Both figures 4.16c and 4.16a show peaks around $380\,\mathrm{cm}^{-1}$, $717.5\,\mathrm{cm}^{-1}$ and an important weak peak at around $\sim 50\,\mathrm{cm}^{-1}$ lying in the range of the frequencies derived from the spectrum of the post-pedestal which is presented in Fig. 4.14b. A shorter excitation wavelength e.g., argon (wavelength $\lambda = 488\,\mathrm{nm}$), would allow for a Raman shift with greater confidence to be registered. The shorter wavelength might measure the Raman spectrum of a Ti:Sapphire crystal, used for laser light amplification.

The low-frequency mode in the measured Raman spectra indicate that the lattice of the Sapphire crystal may support the eigenmodes in the frequency range of the structures observed in the post-pedestal. This result supports the assumption that phonons can play a central role in the process of generation of the post-pedestal observed in the time domain.

4.4.5 Discussion of observed effects

The experimental results presented in 4.4.1 have shown that the ragged pedestal, which appears in front of the main pulse, has a structure that clearly resembles the post-pedestal. Figure 4.10 clearly shows that the leading pedestal and the trailing pedestal are mirror-symmetric, in particular, in the vicinity of the main pulse. The same structure in the pre-pedestal can be observed in the post-pedestal. This finding confirms that the leading pedestal was generated from the trailing pedestal, which is coherent with the main pulse. The coherence of the post-pedestal is required according to the physics of the process described in 4.2.

It is confirmed that a Ti:Sapphire-based master oscillator generates the post-pedestal. This findings follows from the experimental measurements of the temporal profile of the seed pulses from the commercial master oscillator at LOA (Fig. 4.12). This includes

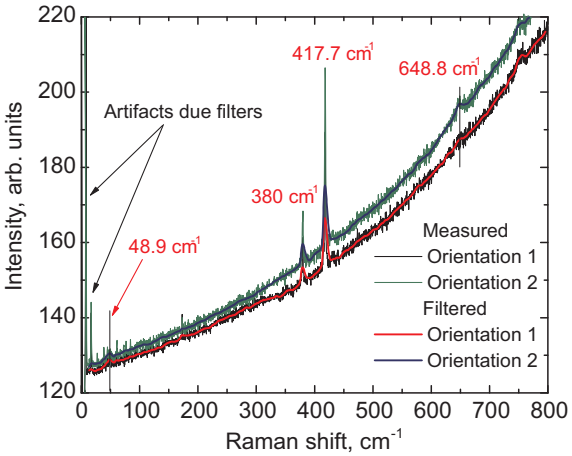

(a) Conventional sapphire substrate

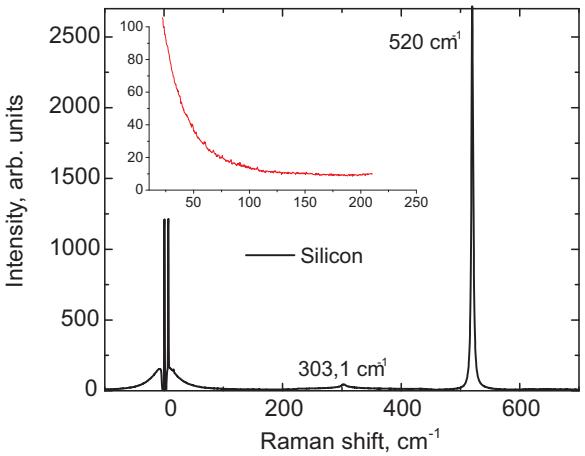

(b) Silicon spectrum for reference

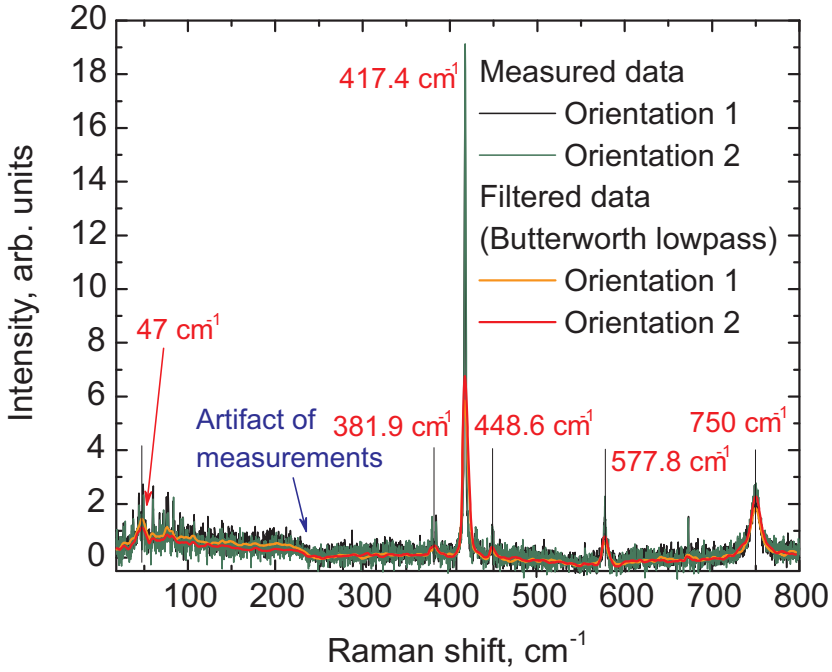

(c) High quality and purity sapphire substrate

Figure 4.16: Raman spectrum of sapphire substrates

a Ti:Sapphire crystal, several dielectric mirrors and a dispersion compensation scheme based on several chirped mirrors. The laser system was used in configurations with master oscillators either with dispersion compensation based on prisms or chirped mirrors. This did not show the difference in the temporal contrast. Thus the Ti:Sapphire crystal is the most probable source of the post-pedestal.

One might propose that the specific temporal profile is caused by constructive interference of eigen modes of the resonator, which form the laser cavity. The discrete eigen modes might form such a complicated temporal profile while forming ultra-short pulses in the Kerr-lens mode-locking. However, a pedestal, formed in a such way must be symmetric around the main peak. In additional, the post-pedestal is also observed when the parametric-based front-end is used. The latter creates pulses in a parametric process with generation of a white light and therefore Kerr-lens mode-locking can be excluded from the consideration.

The majority of ideas cannot satisfy the condition that the generated pedestal follows the pulse and in the case of a low B-integral it does not exist in front of the main peak. The most reasonable solution may be that an ultra-short pulse induces a stress in the medium because of the high peak intensity. This can explain the asymmetric shape of the temporal contrast. An ultra-short pulse initiates physical processes which then change the temporal shape. In other words, the post-pedestal is a result of self-induced processes.

This process may happen in air or in a Ti:Sapphire crystal. There are no assumptions about the air except the considered Raman response of air molecules. However, the investigation presented in 4.4.3 shows that the Raman effect in air is negligible. This leads to the conclusion that the post-pedestal is generated inside the Ti:Sapphire crystal and is associated with the inner structure and atoms constituting the crystal.

It is well-known that Ti:Sapphire is a vibronic crystal and phonons play an important role in the laser parameters of the crystal [135]. The vibronic nature provides the broad emission spectrum [128]. The first idea thus might be that phonons, collective lattice vibrations, could be responsible for the generation of the pedestal and that somehow the phonons can be displayed in the measured cross-correlation traces.

Phonons in a sapphire crystal could be a good explanation for the observed post-pedestal but in this case, the crystal must support the observed frequencies (shown in Fig. 4.14b). The vibrational modes in a crystal can be either Raman-active or IR-active. The presence of Raman-active modes was investigated in section 4.4.4. The measured Raman spectra showed that there is a high probability, that these low-frequency and thus low-energy phonon modes can exist in a sapphire crystal and thus must exist in a Ti:Sapphire crystal. The presence of IR-active modes was not investi-

gated because of the lack of required instruments.

It is important to explain, how the lattice vibrations of certain frequencies are induced. The answer can be given by one of mechanisms known in literature. For instance let us consider the Impulsive Stimulated Raman Scattering (ISRS) [136, 137, 138, 139].

Impulsive Stimulated Raman Scattering (ISRS)

Let us assume that a vibrational mode with the frequency Ω is supported by the medium. In the classical stimulated Raman scattering, the incident light with frequency ω_2 gets scattered on the Raman-active mode resulting in the photon $\omega_1 = \omega_2 - \Omega$. However, if the spectrum of the incident light is broad enough and includes both frequencies ω_1 and ω_2, it can be a driving force for the phonon. In this case, the higher-frequency photon with the frequency ω_2 gets coherently scattered into lower frequency photon ω_1 producing the coherent phonon with the frequency $\Omega = \omega_2 - \omega_1$ and causing a red-shift of the incoming pulse spectrum. In other words, the phonon is generated by frequency mixing of the spectral components of the incident light which is characterized by a broad enough spectrum. Coherent phonons are collective oscillations of the crystal lattice components which are characterized by a high spatial and temporal coherence. In other words, ISRS process forms a standing wave in a medium.

In theory a coherent phonon is described as a harmonic oscillator with the amplitude Q

$$\frac{d^2Q(t)}{dt^2} + 2\beta\frac{dQ(t)}{dt} + \Omega_0^2 Q(t) = F(t) \tag{4.6}$$

where $\Omega_0/2\pi$ is the natural frequency of the oscillations, β is the damping parameter, and $F(t)$ is the driving force caused by the broadband light. The damping constant characterizes the dephasing time of the phonon mode as $\beta = \tau_{\text{dephasing}}^{-1}$. The driving force $F(t)$ depends on the process leading to generation of the coherent phonon. In the case of ISRS, it is given in the following

$$F(t) = \frac{1}{2M^*}\left(\frac{\partial\alpha}{\partial Q}\right)_{kl} E_k E_l \tag{4.7}$$

where M^* is the reduced mass of the crystal lattice, $\partial\alpha/(\partial Q)$ is the Raman tensor of polarizability, and E_k and E_l represent the spectral components of the electromagnetic field of the incident light. The mechanism is called impulsive because of the short time acting driving force $F(t)$ compared with the period of the phonons. ISRS is a resonant process and has to satisfy energy conservation and the wavevector laws. The

field components E_k and E_l must satisfy the phase-matching conditions

$$\omega_l - \omega_k = \Omega \tag{4.8a}$$

$$k_l - k_k = K \tag{4.8b}$$

where K is the wavevector of the phonon, k_l and k_k are the wavevectors of the corresponding photons ω_l and ω_k, respectively.

It is worth mentioning that despite the broad spectrum, the pulses are stretched and therefore have a long pulse duration. According to literature, the post-pedestal can be generated by either the transform-limited pulses or stretched pulses with the duration exceeding 1 ns. This creates a question if ISRS works in these conditions or not. The problem of **coherent** generation of a coherent phonon requires additional investigations.

It is known from literature that if a IR-active phonon mode is excited in a medium it may induce a macroscopic polarization which, in turn, can cause an electromagnetic radiation at the frequency of the phonon [139]. Thus, the presence of IR-active modes in the range of interest can be confirmed by direct measurement of the THz radiation from the sapphire crystal.

Another question is why the post-pedestal is observed in the temporal traces measured using the Sequoia device because it requires that the light of the post-pedestal is lying in the same spectral range as the main pulse. This is associated with the fact that the Sequoia can characterize pulses in a comparably narrow spectral range only. Thus, it is not clear why the **coherent** oscillations lying in the same spectral range as the main pulse.

The light forming the post-pedestal must have a similar direction and spectral parameters to be observed in the cross-correlation trace. The spectral range of the emission forming the post-pedestal can be estimated. Some parts of the laser system and the used characterization technique have a spectral selectivity. The stretcher, as well as the compressor, both based on reflective diffraction gratings, can transmit only a spectral bandwidth of at maximum 150 nm. This range is limited by the geometry and the chosen incident angle. The high-dynamic range characterization method also has spectral selectivity because of the nonlinear crystals and optics, the frequency doubling and the sum-frequency generation nonlinear processes that are used for characterization. Nonlinear crystals have a dependence of the efficiency on the wavelength at a certain angle which is needed to fulfil the phase matching requirements. This means that the approximate spectral bandwidth of the generated post-pedestal is limited to the range $\Delta\lambda \approx$ 750-850 nm.

The measured cross-correlations traces are presented with a logarithmic vertical scale meaning that the ragged structures with an oscillating shape in a logarithmic scale are in fact post-pulses if the vertical scale is linear (see Fig. 4.17). These post-pulses have a well reproducible shape in the range of two orders of magnitude of intensity. The physical process generating them must be extremely stable and reproducible.

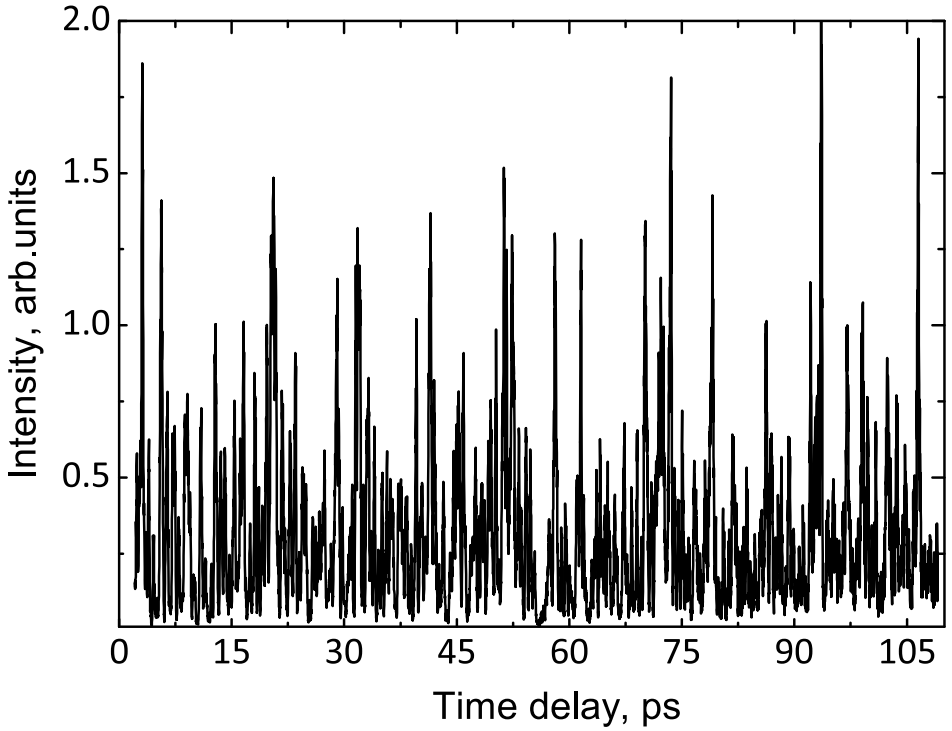

Figure 4.17: Coherent post-pedestal presented in the linear vertical scale

During amplification the energy stored in the active medium is not fully depleted. A certain amount of electrons are still in the excited state and are able to emit light. The ions of the corresponding electrons are surrounded by an oscillating environment. The phonons affect the susceptibility of electrons leading to its modulation [140]. The phonons may impact the excited electrons leading to their transition to the lower level leading to the light emission. Moreover, it can even create a direction selectivity of the emission which may depend on the phase of the phonon. However, to support the coherent post-pedestal, the process must be also **coherent**. In this case it would lead to the coherent emission at the wavelength of laser transition observed as the post-pedestal in the time domain. This theory for now is speculative and requires a serious investigation of this series of processes.

If this theory regarding the phonon nature of the observed post-pedestal is correct, other vibronic crystals must also show a similar effect. This could be possible to check with a laser system based on a Cr:Forsterite crystal. This requires a high-dynamic range characterization tool for the corresponding wavelength of $\lambda = 1.24\,\mu$m.

4.5 Analysis of a measured pulse shape of a high-field laser system

This section is dedicated to the analysis of a measured pulse profile of the home-made 100 TW High-field laser system at the Max Born Institute (MBI). I am going to show how to apply the obtained knowledge.

The high-field MBI laser system employs a Double-CPA technique [76]. It consists of a front-end with temporal filtering based on cross-polarized waveform generation (XPW) followed by a second stretcher, several amplifiers and the final compressor, which is based on two reflective diffraction gratings.

A prototype of the new Sequoia HD cross-correlator was used for the temporal contrast characterization. A part of the beam is taken for the measurement then attenuated down to the energy level E $\sim$ 0.5 mJ in front of the cross-correlator. Fig. 4.18a illustrates the pulse shape. The curve is measured before a plasma mirror at half-of-full energy with the smallest available step of the Sequoia HD (17.8 fs). The curve demonstrates a clean temporal trace in the temporal range from -550 to -100 ps with a level of ASE $\approx 10^{-11}$. The temporal contrast was further improved by removing the intense pre-pulse at approximately ≈ -50 ps. Since the laser system includes a few uncoated optics it was assumed that the pre-pulse is caused by double internal reflection in an optical element. Its refractive index was assumed to be close to the refractive index of glass. The refractive index and the pulse delay deliver information about the approximate thickness of the optical element. The source of the pre-pulse was identified to be a dielectric mirror mounted with the rear surface towards the pulse. As a result, the uncoated side of the mirror caused the pre-pulse as a reflection of the main pulse. The following main pulse is reflected from the dielectric coating inside the substrate of the mirror. When the mirror was changed and mounted properly, the pre-pulse with the relative delay -50 ps has disappeared. The improved contrast is presented in Fig. 4.18c.

Fig. 4.18b illustrates post-pulses generated in the last cascade caused by the birefringence of the Ti:Sapphire crystal. There are three equidistant pulses of similar peak intensity level, which correspond to three passes through Ti:Sapphire crystal. A simple calculation shows that a 0.5 mm glass plate (n = 1.5) may cause a post-pulse with a delay at approximately $\approx$ 5 ps. Without a very thin glass plates in a beam path, the birefringence of the active medium is the only reason for post-pulses below 5 ps. Obviously, these post-pulses will bring about pre-pulses with a shifted delay through the mechanism, described in 4.2. However, if the post-pulses are generated in the final amplification cascade, no pre-pulses are usually observed after that.

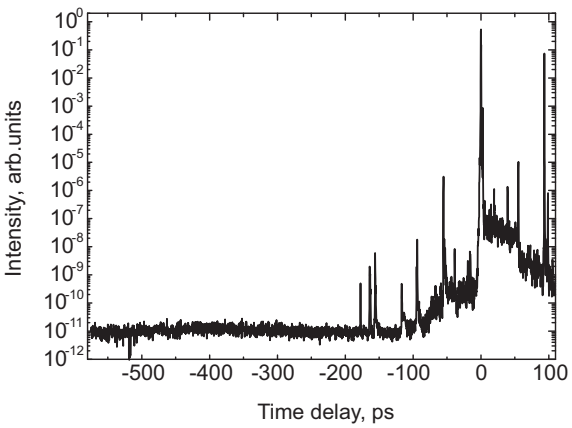

(a) Full temporal scale Sequoia measurements of the 100 TW MBI laser

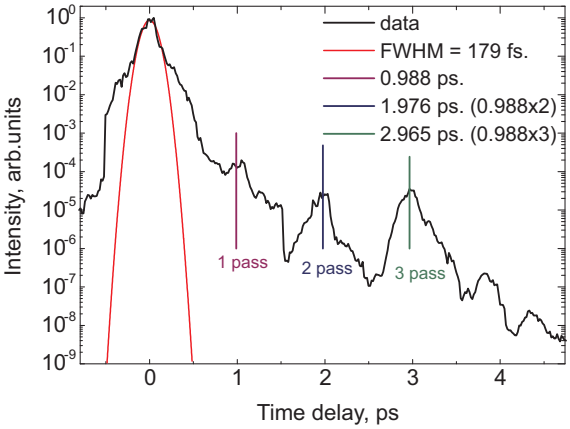

(b) Post-pulses generated because of the birefringence of Ti:Sapphire

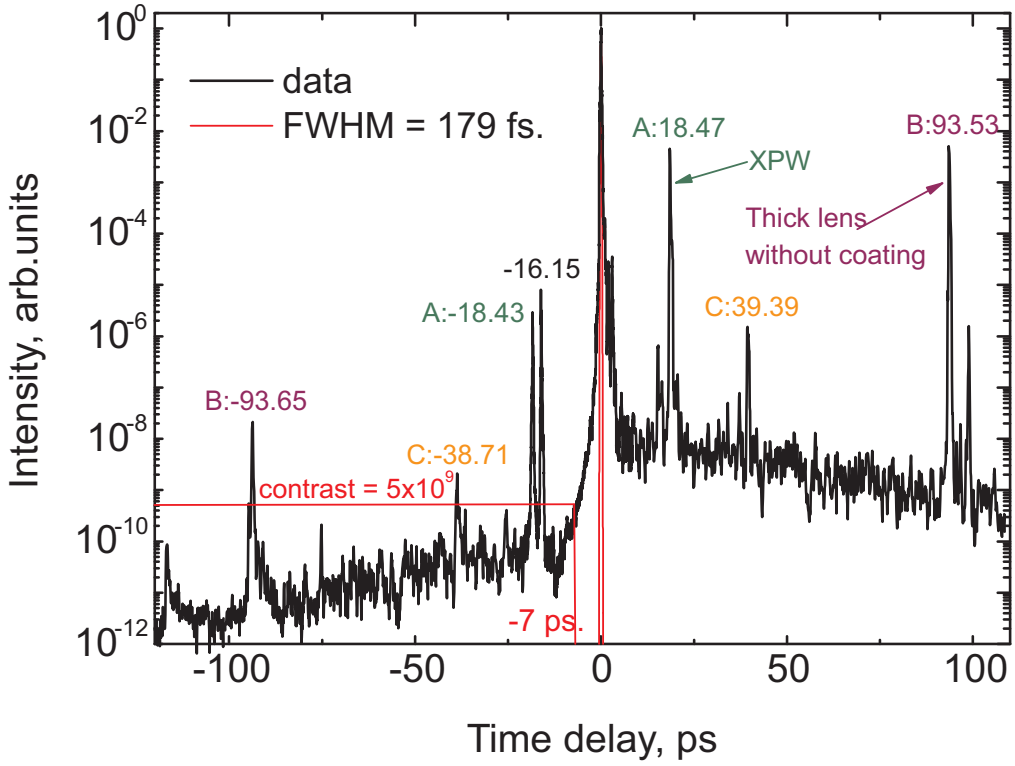

(c) Cross-correlation trace measured for the 100 TW laser at MBI. The pre- and post-pulses are generated by the optics, such as the XPW crystal, as well as by measurements artefacts. The long post- and pre-pedestals generated by the Ti:Sa crystal and SPM process are clearly visible

Figure 4.18: Features of temporal contrast of the home-made 100 TW MBI laser system

The thickness of the Ti:Sapphire crystal in the last cascade of the High-Field MBI laser system is 35 mm. Taking into account the difference in refractive indices of the orthogonal polarizations, the delay between the post-pulses generated by the birefringence can be estimated to be approximately $l \times \Delta n/c \approx 0.922$ ps, close to the 0.988 ps derived from the cross-correlation trace. The difference can be explained by the difference in the refractive indexes of the crystal in the scheme and the refractive indexes, derived from the literature ([107, 108]). An additional path length due to the small angle between the beam and the crystal due to the amplifier geometry is negligible.

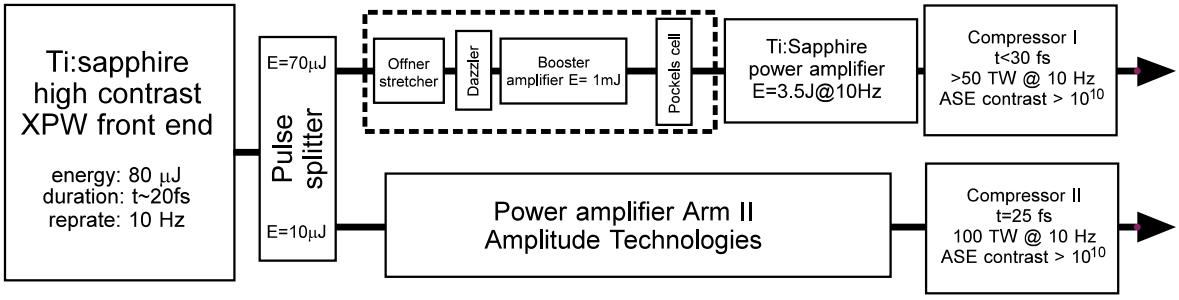

Figure 4.19: Block diagram of the 100 TW high-field MBI laser system

The leading front of the main pulse is steep in the temporal trace in Fig. 4.18c. The temporal contrast at -7 ps is 5×10^9. The pre- and post-pedestals that are discussed in previous paragraphs are clearly visible. In addition, several pre- and post-pulses are observed starting from -100 ps in front of the main pulse. The most intense pulses are marked. There are two pairs of pulses (**B** and **C**) and a triplet **A**. The pulses in the groups **B** and **C** are equidistant. This may be an indication that they are generated by the SH beam in the Sequoia. However, the relative intensity of the pre-pulses does not follow a square relationship (4.2). The lower-than-expected peak intensity of the pre-pulses can be explained by the large step of the scanning, which is approximately ≈ 250 fs in the range -100 – -10 ps. The pre-pulses are not measured properly due to the large time step. As seen in 4.2.1, the pre-pulses generated by SPM usually have a shifted delay. This temporal shift increases with increasing the absolute delay of the post-pulse. No temporal shift in the generated pre-pulses is observed.

The characterization process was simulated. The main peak was fitted by a Gaussian function for the simulation. Then three intense post-pulses with a related delay of 18.5 ps (**A**), 39.4 ps (**C**) and 93.5 ps (**B**) were added to the main peak simulating the intense post-pulses observed in the measured temporal trace. After that, the characterization was simulated as described in section 2.5.2. The correlation was calculated between the resulting shape and its square. The resulting curve, as well as the real measured curves, are presented in Fig. 4.20. The pre-pulses at -93 (**C**), -18 (**A**) and -76 ps match well, except for the amplitude. These three pre-pulses are generated by

the characterization device. The pre-pulse at -38 ps (**B**) is real and generated by SPM. The real measured pre-pulse is slightly shifted closer to the main peak. This is an additional indication that is it is generated by SPM as was discussed in section 4.2.1.

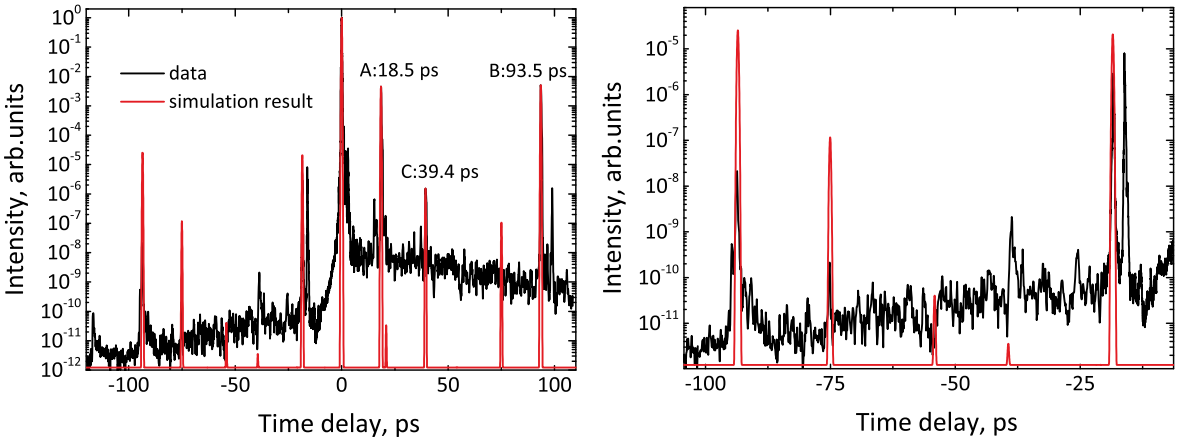

(a) Temporal contrast of the 100 TW MBI laser

(b) The leading part of the temporal trace

Figure 4.20: Analysis of the measured temporal traces of the MBI 100 TW laser. Black curve shows the measured temporal contrast. The main peak was fitted by a Gaussian function. It has been taken for the simulation. Three post-pulses (A, B and C) as in the measured trace were then added. Then, the second harmonic was simulated by taking the square of the initial shape and the correlation calculated between the fundamental and its second harmonic. The red curve shows the result of simulation of the characterization using a third-order cross-correlator. The pre-pulses matching the simulation with lower peak intensity do not exist in the real temporal profile of the measured pulses

There are two pre-pulses with a delay similar to the delay of the post-pulse **A**. The pre-pulse with the same delay as the post-pulse delay is a replica due to the cross-correlation. However, the second pre-pulse at approximately ≈ -16 ps is real. It is generated due to the nonlinear phase shift. In principle, an approximate B-integral value of the part of the laser system between the reflection producing the post-pulse, and the last re-compression stage can be extracted if the envelop of the stretched pulse is known. It is obvious that both pre-pulses will disappear if the corresponding post-pulse is removed. Its source was identified as an internal double reflection in a XPW crystal which is not carefully aligned. When it is aligned properly, the crystal does not cause the post-pulse as can be seen in Fig. 4.18a.

An ultra-fast Pockels cell was used in the system with a rising time approximately ≈ 300 ps. This corresponds to the duration of the stretched pulse. It helps to give a comparably clean temporal shape. A further plasma mirror filters the entire region in front of the main peak and suppresses the intensity of the pre-pedestal and pre-pulses

by four orders of magnitude. Together, this provides good parameters of the temporal contrast of the particular high-field laser system.

Now, it is necessary to mention the characterization of high power laser systems. There are certain requirements for the energy and intensity of the characterized pulses. The Sequoia, for instance, is suitable for the characterization of a front-end with an energy of approximately $\sim 1\,\mathrm{mJ}$, 20 fs pulse duration with corresponding spectral width and few millimetre diameter of the beam. However, what can be done with higher energies? For instance, if a PW level laser system needs to be characterized. There are two correct ways to do this. First, one can attenuate the compressed beam down to the mJ energy level using reflective optics, then scale the beam size down to the size of the input aperture of the characterization device and characterize it. This way is the most appropriate. However, it is often complicated to deal with high power beams of a large size. As an alternative, a small part of the spatially expanded beam at full energy must be characterized. It is also necessary to repeat the measurements at several points along the beam aperture to ensure that the temporal contrast is the same for the whole aperture. However, the characterization procedure is often different. A high-field laser system usually is attenuated by simply switching off of several pump lasers. The following characterization is done properly, except for the energy of the beam produced by the laser system. This incorrect characterization is clearly visible in the obtained temporal traces. The pre-pedestal will be generated anyway in any high field laser system. The confidence about it is associated with the fact that the B-integral value and the stretching factor are high enough to lead to pre-pedestal generation in high power cascade. If the temporal contrast of a high power laser system is measured properly before any nonlinear filtering, such as with a plasma mirror, the pre-pedestal will be visible in the temporal trace and have relative intensity level of $> 10^{-9}$.

Chapter 5

Temporal contrast improvement using rotation of the polarization ellipse in a gas-filled hollow-core waveguide

5.1 Introduction

In the previous chapters we have highlighted issues of modern high-power laser systems based on Ti:Sapphire material and the CPA concept. Here, I am going to discuss a technique aiming at temporal contrast enhancement. Information presented in this chapter is useful not only for Ti:Sapphire-based laser systems but can be applied to modern fibre- and thin-disk based lasers using material different from Ti:Sapphire to generate laser light.

Nonlinear temporal filtering is a commonly used attribute of modern ultra-fast lasers. The mostly used XPW technique has several issues, one of them is the low efficiency, which typically does not exceed 25 %. XPW can also significantly destroy the spatial beam profile and the surface of the XPW crystal is subject to degradation. To avoid this, a short hollow-core fibre is used in front of the XPW in order to improve the spatial parameters of the beam [141]. As was mentioned in 1.7.3, nonlinear rotation of the polarization ellipse can be an alternative to the widely used XPW tehcnique. This chapter describes in details the NER-based technique and suggests an implementation involving a hollow fibre.

It is important to mention that a part of the results presented in this chapter is going to be published in an article where I am the corresponding author.

5.2 Delayed Kerr effect and the choice of a medium for NER

One can see that there are different media which can be used for the temporal filtering. It is important to choose one medium or a group which suits the best our application. In this paragraph, it will be explained what medium is the most appropriate for NER.

Since NER is based on the optical Kerr effect, the optical Kerr response plays a central role in the choice of the medium. There are several physical mechanisms contributing to the Kerr response of a medium which differ in terms of physical origin and time range. The fastest term contributing to the optical Kerr response is associated with anharmonicity of the electron oscillations in a strong electromagnetic field and it was considered in 1.2.1. This optical response is fast, even on the femtosecond scale, and is usually considered to be instantaneous [21]. The second mechanism contributing to the Kerr response on the femtosecond scale is associated with the molecular structure of the medium. It relates to the orientation of the molecules in liquids and the Raman response in gases. This physical mechanism is slower compared to the electronic Kerr response [82]. Free electrons also contribute to the optical response on the femtosecond scale.

The electronic contribution to the nonlinear refractive index can be written as [82]:

$$\Delta n(\omega) = n_2(\omega)|E|^2 + \frac{i\alpha(\omega)}{2k_0} \tag{5.1}$$

The term $\alpha(\omega)$ is responsible for absorption.

In the case of a comparably slow Raman response, the following equation applies, which includes the electronic and Raman contributions [82]:

$$\Delta n(\omega) = n_2(\omega) \int_0^\infty R(t')|E(r, t-t')|^2 \mathrm{d}t' + \frac{i\alpha(\omega)}{2k_0} \tag{5.2}$$

The variable t' is $t' = t - \tau$. The nonlinear response function $R(t)$ includes both the electronic and Raman responses. Assuming the electronic response to be instantaneous, this function can be written as:

$$R(t) = (1 - f_R)\delta(t) + f_R h_R(t) \tag{5.3}$$

The term f_R in (5.3) represents the fractional contribution of the Raman response. The h_R term reflects the form of the Raman response in time [82].

It is known from literature that different materials were used for NER: air [79, 80],

liquid CS_2 [78, 81] and other gases [77]. In [79] a high efficiency of $\approx 60\,\%$ at a mJ seed energy level was demonstrated, but the slow nonlinear response of air did not allow to transmit short pulses and led to clipping of the pulse spectrum. The majority of the optical Kerr response of air at low ionization originates from molecular N_2 and O_2. Both molecules have the above-mentioned Raman contribution within the intensity-dependent part of the refractive index n_2. This is caused by their molecular nature. The Raman contribution is higher than the instantaneous electronic contribution and the characteristic time of the Raman response in the case of air is approximately $\approx 70\,\text{fs}$. This means that the optical Kerr response of air is changing during the pulse duration (this is the case of a classical front-end with $\tau \approx 30\,\text{fs}$.) and the value of the optical Kerr nonlinearity depends on time. This effect is unwanted because it can lead to temporal distortion of the beam profile. Similar observations happen with CS_2, used in [81] for nonlinear filtering. Molecules introduce a term into the Kerr response which is not instantaneous for femtosecond pulses [21]. The additional contribution appears to change the temporal beam profile and makes the theoretical prediction more complicated. Moreover, in the case of chirped pulses, it leads to spectral clipping or spectral selection. Since we deal with ultra-fast pulses, it is worth considering media with only the instantaneous optical Kerr effect. Atomic gases, such as noble gases can be a good option for NER.

To be used for nonlinear temporal filtering, the NER technique must be energy scalable. However, self-focusing [142, 143] and ionization [144, 145, 146] limit the maximal intensity and, therefore, the scalability. The self-focusing process may bring the beam into the regime of filamentation. This increases the intensity and leads to a higher level of ionization and, as a result, it limits the efficiency of the NER filtering. Since noble gases have the highest values of the first ionization potential, they are the best option for this nonlinear temporal filtering technique.

5.3 Implementation of the temporal filtering technique

As it was discussed above, the ultra-short duration of the pulses dictates the choice of the nonlinear medium for the temporal filtering based on the rotation of the polarization ellipse. Noble gases have been chosen as the medium for NER in our experiments. Let us concentrate on the implementation scheme for the temporal contrast improvement. The existing literature shows a wide range of proposed and tested schemes for the NER. Those include a cavity [79], a hollow-core fibre [77] or even a simple spatial filter with two lenses [80].

Because of the large value of the B-integral required (see 1.7.3), it is logical to scale the length of the nonlinear interaction. In addition, since the rotation of the ellipse depends on intensity, it is worth choosing an optical scheme which has eigenmodes in order to avoid a situation where the enhancement of the temporal contrast is a function of the radial coordinate. Thus, we have two options: a cavity formed by two spherical mirrors such as the cavity of a regenerative amplifier or a hollow-core fibre (HCF). The pulse injection/ejection system of a regenerative cavity is based on a manipulation of the direction of the linear polarization. Since we are going to operate with an elliptic polarization, it appears challenging to implement this option. Thus, it was decided to use an HCF.

HCF may support the necessary length of interaction and provide a good control over the effective nonlinear interaction that cannot be reached by a simple focusing of the laser pulses in a medium. As will be shown below, it has eigenmodes and thus also acts as a filter of the spatial mode. Variation of the HCF geometry may be used in order to add flexibility to the filtering scheme. The length and the inner core radius of HCF can be varied, giving flexibility and an opportunity to work in comfortable conditions. The large B-integral value also leads to a significant spectral broadening. The resulting spectrum can be efficiently re-compressed in the following. HCFs are widely used in modern systems [141, 147] for a broad spectrum generation with subsequent post-compression. A HCF guides the beam in order to reach a certain filtering efficiency and broadening without unwanted ionization.

5.3.1 Hollow-core fibres

A hollow-core fibre is not a classical fibre but a capillary tube where the refractive index value of the cladding is higher than the refractive index of the core. Optical fibres of this kind are lossy and do not act as a good conductor of light compared to classical optical fibres. Conversely, manipulations with the HCF must not lead to unwanted additional losses.

The field propagation in a HCF can be expressed as

$$E(r,\omega) = F(r,\theta)A(\omega)e^{i(\gamma z-\omega t)} \tag{5.4}$$

where $F(r,\theta)$ is the transverse field distribution, $A(\omega)$ is the spectral mode amplitude and γ is the propagation constant.

Let us consider the HCF in the configuration of a right circular cylinder of a radius a which is large compared with the optical wavelength ($a \gg \lambda$). Let us also assume that the pulse power P is below the critical power of self-focusing $P < P_{\mathrm{cr}}$. In these

conditions and at low-losses in HCF one can determine the modes $F(r, \theta)$ [148]. Those modes are transverse circular electric modes TE_{0m}, transverse circular magnetic modes TM_{0m} and hybrid modes EH_{nm} ($n \neq m$) with both, electric and magnetic fields. The n and m coefficients are integers characterizing the propagation mode.

The losses in the case of using a HCF are determined by the losses of the eigenmode and the coupling conditions. The attenuation constant for eigenmodes is inversely proportional to the bending radius $\alpha \propto 1/R$ and thus, it is important to minimize the bending of the HCF which can be achieved using stretched fibres. The expression for the attenuation coefficient for the EH_{nm} spatial modes in the case of straight dielectric hollow-core fibres can be expressed as:

$$\alpha_{nm} = \left(\frac{u_{nm}\lambda}{2\pi}\right)^2 \frac{\nu^2 - 1}{2a^3\sqrt{\nu^2 - 1}} \tag{5.5a}$$

$$\nu = \sqrt{\frac{\varepsilon_{\text{cladding}}}{\varepsilon_{\text{core}}}} \tag{5.5b}$$

where ν is the ratio between the refractive indices of the cladding and the core, u_{nm} is the mth root of the equation $J_{n-1}(u_{nm}) = 0$ where J_α is the Bessel function of the first kind. For instance, $u_{11} = 2.40483$, $u_{12} = 5.52008$, $u_{13} = 8.65373$. Equation (5.5) gives the attenuation constant in the units of decibel per unit of length. In order to use the calculated value in the equation for the power or intensity degradation ($P(z) = P_0 e^{-\alpha z}$), the attenuation constant must be expressed in units of reciprocal length

$$\alpha[\text{cm}^{-1}] = \frac{\ln 10}{10} \cdot \alpha[\text{dB/cm}] \tag{5.6}$$

Fig. 5.1a illustrates the losses for the EH_{1m} modes. One can see that the EH_{11} mode has the lowest attenuation coefficient and the attenuation grows significantly with the number of the mode.

The coupling conditions are determined by the overlap of the spatial mode of the input beam and the spatial eigenmodes of the HCF. When a Gaussian spatial mode is coaxially focused into a HCF, only EH_{1m} modes are excited [149]. Let us consider the coupling conditions. For this we need to know the spatial distributions of the input mode and the EH_{1m} modes of the fibre which are expressed below:

$$E_{\text{Gaussian}}(r) = E_0 e^{-r^2/\sigma^2} \tag{5.7a}$$

$$E_{\text{EH}_{1m}}(r) = E_0 J_0(u_{1m} r/a) \tag{5.7b}$$

where σ is the radius or the half-width at the level $1/e$ of the maximum, $0 \leq r < a$,

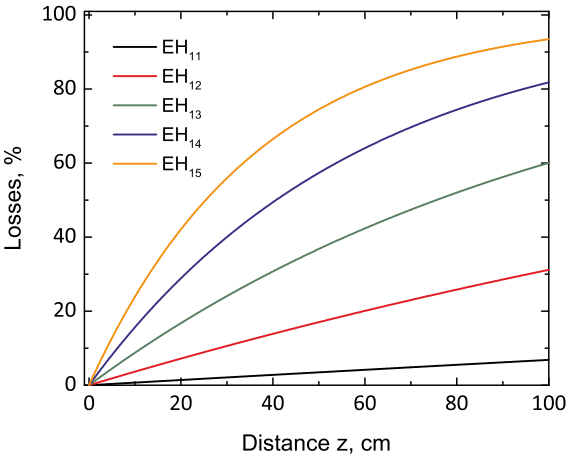

(a) Dependence of total losses in a hollow-fibre on the propagation distance in the case $\lambda = 800\,\text{nm}$, $a = 125\,\mu\text{m}$

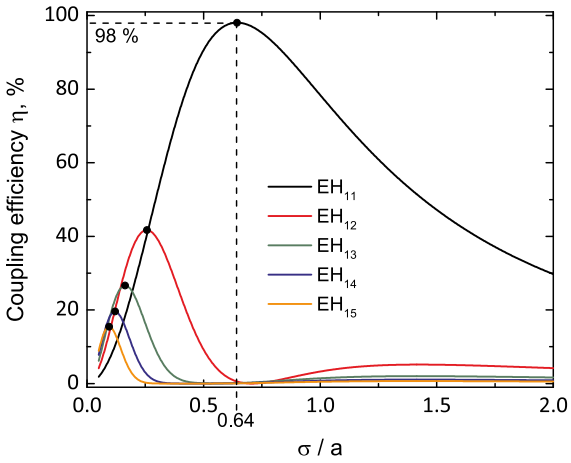

(b) Dependence of the efficiency of the coupling into the hollow-fibre on the ratio between the width of the input beam σ and the core radius a of the fibre for EH_{1m} modes

Figure 5.1: Losses and efficiency of the coupling into a hollow-fibre calculated for EH_{1m} modes and a silicon cladding of the fibre

J_0 is the zero-order Bessel function of the first kind. The coupling efficiency is then

$$\eta_{1m} = \frac{\left(\int_0^a e^{-r^2/\sigma^2} J_0(u_{1m} r/a) r \mathrm{d}r\right)^2}{\int_0^\infty e^{-2r^2/\sigma^2} r \mathrm{d}r \cdot \int_0^a J_0^2(u_{1m} r/a) r \mathrm{d}r} \tag{5.8}$$

Fig. 5.1b illustrates the coupling efficiency for different eigen modes depending on the core radius of the fibre and the input beam radius σ. The optimal coupling efficiency is achieved for the EH_{11} mode when $\sigma/a = 0.64$. As mentioned above, the eigen modes of higher orders experience higher losses and only the lowest mode survives in a long HCF. Taking into account these two facts the high-order modes can be neglected at long length of a HCF and it can be considered as a single-mode fibre [149]. Theoretical transmission of EH_{11} in a HCF can be above 95 % in case of a good input coupling [149, 150]. However, practically it does not usually exceed 70 %.

Ionization [144, 145, 146] and self-focusing in the HCF [13, 142, 28] limit the maximal throughput intensity, i.e., the input energy of the pulses. However, the thresholds for ionization and self-focusing can be increased. Circular polarization decreases the nonlinear response of media [21, 151, 152] and the level of ionization [153, 152, 154]. The ionization threshold needs to be estimated for elliptical polarization, and lies between those for the linear and circular ones [144].

To estimate the critical power of self-focusing one can use equation (1.33):

$$P_{cr} = \frac{\alpha \lambda_0^2}{4\pi n_0 n_2} \tag{5.9}$$

for the EH_{11} beam mode $\alpha = 1.86225$ [28].

It is important to know the ionization level in order to avoid unwanted effects. The ionization rate for linearly polarized light can be estimated using the Ammosov-Delone-Krainov equation [144, 146]:

$$w = \frac{E_p}{\hbar} |C_{n^* l^*}|^2 \frac{(2l+1)(l+|m|)!}{2^{|m|}|m|!(l-|m|)!} \left(\frac{4E_p}{\hbar \omega_t} \right)^{2n^* - |m| - 1} e^{-4E_p/(3\hbar\omega_t)} \tag{5.10a}$$

$$|C_{n^* l^*}|^2 = 2^{2n^*} (n^* \Gamma(n^* + l^* + 1) \Gamma(n^* - l^*))^{-1} \tag{5.10b}$$

$$\omega_t = \frac{e|E(t)|}{\sqrt{2 m_e E_p}} \tag{5.10c}$$

where $n^* = Z(E_p^h / E_p)^{1/2}$ is the effective principal quantum momentum, l is the orbital quantum momentum, m is the magnetic quantum momentum, Z is the charge of the atom residue, E_p is the ionization potential of the level, E_p^h is the ionization potential of hydrogen, $l^* = n^* - 1$ is the effective value of the orbital quantum number, Γ is the Euler gamma function and $E(t)$ is the instantaneous electric field. Using equation (5.10) one can estimate the free-electron density caused by the electric field:

$$n_e = N_0 \left(1 - e^{-\int_{-\infty}^{t} w(t') \mathrm{d}t'} \right) \tag{5.11}$$

where N_0 is the density of neutral atoms which can be obtained using the ideal gas law

$$PV = NkT \tag{5.12}$$

where P is the gas pressure, V is the gas volume, N is the number of atoms, T is the gas temperature and k is the Boltzmann constant.

The ionization threshold can be estimated as the level when the change of the refractive index caused by the electron gas is well below the one caused by the Kerr

effect [143]:

$$\frac{\omega_p^2}{2\omega_0} \ll n_2(p)I \tag{5.13a}$$

$$\omega_p = \sqrt{\frac{e^2 n_e}{m_e \varepsilon_0}} \tag{5.13b}$$

where ω_p is the plasma frequency, e is the charge of the electron and $n_2(p)$ is the nonlinear refractive index of gas. The function $n_2(p)$ is linear.

The pressure gradient of gases can additionally decrease the negative effect of the ionization [155] at the input of a HCF. Ionization at the HCF input leads to energy losses and beam defocussing. This, in turn, leads to a worse input coupling and lower transmission of the HCF. Differential pumping allows the effective nonlinear interaction length to be controlled better. This brings stability to the optical scheme.

Equation (5.14) expresses the evolution of the pressure in the HCF with distance in the case of differential pumping [156, 157].

$$p(z) = \sqrt{p_0^2 + \frac{z}{L}(p_L^2 - p_0^2)} \tag{5.14}$$

with p_0 and p_L the pressures at the entrance and exit of the HCF respectively, L is the length of the HCF, and z is the propagation distance. Since the nonlinear refractive index linearly depends on the gas pressure, the nonlinear refractive index is proportional to the square root of the propagation distance: $n_2(z) \propto \sqrt{z}$.

As it was mentioned in 5.2 noble gases can be considered as the perfect medium for the NER because their Kerr response has only the electronic Kerr contribution. Noble gases provide a significant range of values of n_2 and have a comparatively high first ionization potential because of the closed outer electronic shell (Table 5.1). The values presented in the Table 5.1 are measured for linear polarization.

Medium	n_2, cm^2/W [158]([159])	Ionization potential, eV [160]
Helium	$0.34(0.31) \times 10^{-20}$	24.58
Neon	$0.85(0.87) \times 10^{-20}$	21.56
Argon	$7.96(9.7) \times 10^{-20}$	15.75
Krypton	$18.9(22) \times 10^{-20}$	14.00
Xenon	$54.8(58) \times 10^{-20}$	12.12

Table 5.1: Values of n_2 and the first ionization potentials for noble gases

The dependence of the refractive index on the gas pressure $\mathrm{n}_2(\mathrm{p})$, the intensity

and the propagation length determine the efficiency of temporal filtering as well as the factor of the spectral broadening. The gas pressure allows the effective value of n_2 to be smoothly tuned [161, 162].

5.4 Experimental setup

In this section I am going to describe parameters of a particular implementation of a filtering method for the temporal contrast enhancement. The principle of the scheme of the experiments is presented in Fig. 5.2. A CEP-stabilized front-end laser system (1.3 mJ, 1 kHz, 30 fs) was used as a seed source. The energy of the beam is attenuated by a classic combination of $\lambda/2$ waveplate and polarizer which consists of four reflective polarizers. The latter is also used as a part of the temporal filtering scheme to generate the highly linear polarization required for the improvement of temporal contrast. The nonlinear temporal filtering takes place between two crossed polarizers. Two achromatic $\lambda/4$ waveplates are placed between the polarizers. The first $\lambda/4$ waveplate defines the ellipticity level which at low intensity, when no rotation occurs, is turned back to linear by the second waveplate. A thin broadband polarizer (aligned perpendicular to the first one) selects the high-intensity part of the laser pulse after the re-collimation of the HCF output. The extinction coefficient of the scheme that determines the improvement of the temporal contrast was $> 2.4 \times 10^3$. Ten standard chirped mirrors from Ultrafast Innovations (PC42) and two thin wedges were used to re-compress the pulse and to get an almost Fourier Transform Limited (FTL) pulse duration.

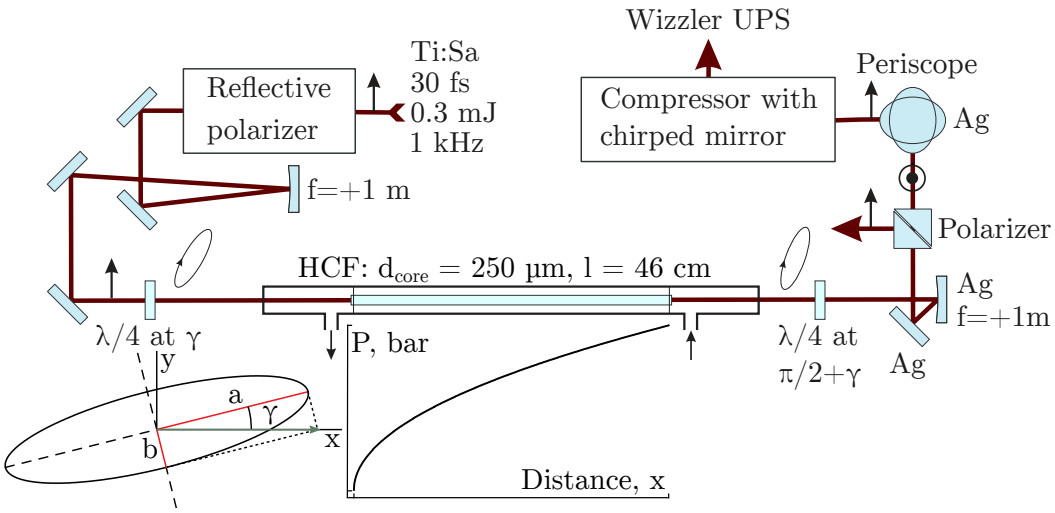

Figure 5.2: Principle of the experimental scheme of the nonlinear filtering method based on elliptical polarization rotation

The laser beam is focused into the HCF ($d_{core} = 250\,\mu$m, $l = 46\,$cm) by a concave mirror(f = +1 m). A pressure gradient was implemented at the coupling plane of the HCF to avoid ionization. It also helps to minimize contamination inside the fibre which appears when the pressure is static. The input of the HCF was pumped down, while the gas was applied at the fibre output. Both, the pump and the gas flow ran permanently creating a constant pressure gradient inside the fibre. It is worth noting that the values of pressure given below represent the the pressure at the exit interface of the HCF (p_L in the equation (5.14)). The experiments were performed with argon gas. The seed energy was limited to $350\,\mu$J because of the relatively low level of the ionization threshold for the HCF that was used in experiments. A longer fibre with larger core radius would allow higher energy throughput.

5.5 Results and discussion

Before presenting the experimental results, it is worth to remind how the NER efficiency can be estimated. The basic theory of this filtering technique was presented in section 1.7.3. In that section, the equation for the conversion efficiency of the NER filtering was presented:

$$\eta(\gamma,\tau,B) = \frac{\cos^2(2\gamma)\int\limits_{-\infty}^{\infty}\sin^2(1/3\cdot B_{peak}e^{-2t^2/\tau^2}\sin(2\gamma))e^{-2t^2/\tau^2}\mathrm{d}t}{\int\limits_{-\infty}^{\infty}e^{-2t^2/\tau^2}\mathrm{d}t} \tag{5.15}$$

This equation is used in this section in order to compare the theoretical estimations with the experimental results. It is important to note that the conversion efficiency only is considered. The experimental conversion efficiency is defined as the ratio of the energy measured after the second polarizer to the energy measured just in front of it. It does not include the energy losses caused by the fibre. These losses must be added to the conversion efficiency in order to see the full picture of total energy losses. In our experiments the HCF transmission was approximately $\approx 56\,\%$.

As well as in section 1.7.3 the ellipticity is expressed through the flattening parameter:

$$f \equiv \frac{a-b}{a} = 1 - \mathrm{tg}|\gamma| \tag{5.16}$$

where a and b are the semi-axes of polarization ellipse and $a > b$; $\gamma = [-\pi/4, \pi/4]$ is the angle between the fast axis of the first $\lambda/4$ wave plate and the polarization plane of the seed. Higher values of the flattening parameter correspond to higher ellipticity. Thus $f = 0$ and $f = 1$ correspond to the circular and linear polarization respectively.

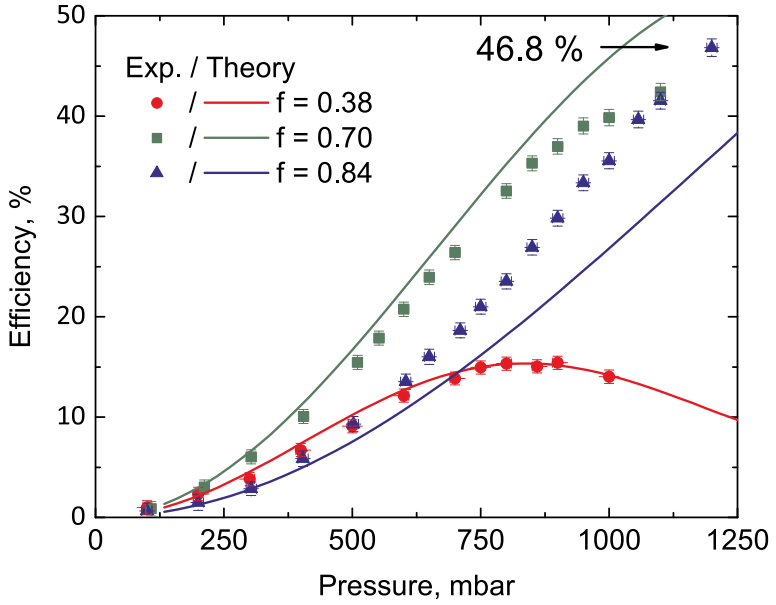

Figure 5.3: Dependence of the efficiency of temporal filtering on the pressure of argon gas (p_L) in the HCF. Dots of different colors correspond to experimental results for different flattening that is indicated in the plot legend. The curves show the corresponding theoretical curves derived accordance with the equation (5.15)

Figure 5.3 shows the experimental data in points and the corresponding theoretical curves derived using the equation (5.15). The pulse duration was taken to be $\tau = 30/\sqrt{2\ln 2}$ fs.

One can see in the Fig. 5.3 that efficiency of NER increases with increasing the ellipticity. In the case of the highest ellipticity, the maximal efficiency was not achieved due to the limits of the experimental setups and chosen parameters of the HCF. Ionization and self-focusing limited the maximal gas pressure and the input pulse energy. Only short fibre ($l = 46$ cm) was available for the experiment. However, a longer fibre with a larger core radius would provide a higher efficiency and flexibility to use other noble gases with a lower n_2. Despite this, a nonlinear filtering efficiency of 46.8 % was achieved in these experiments.

Since the pulses accumulated significant nonlinear phase, self-phase modulation leads to a large spectral broadening. The black curve in Fig. 5.4 represents the broadened spectrum (FWHM ≈ 200 nm) obtained at a pressure of 1100 mbar for argon and highly elliptical polarization (f = 0.84). Rugged structures and spikes in the pulse spectrum that typically accompany SPM broadening [155] are absent and the resulting spectrum is smooth. The seed spectrum (FWHM ≈ 42 nm) is shown in light grey. The polarization rotation with further filtering by a polarizer of the rotated, most intense part of the pulse, plays a key role in obtaining the demonstrated smooth spectrum.

The broadened spectrum was measured after the second polarizer where the low

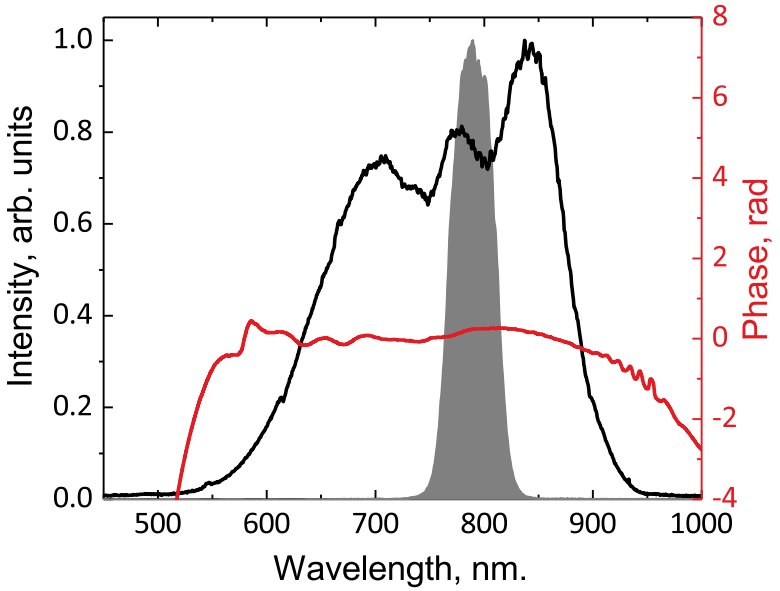

Figure 5.4: Seed spectrum (grey) and 5.5 times broadened (black curve) spectra after NER along with the temporal phase (red curve)

intensity background (non-rotated part) is filtered out. Since the spectral shape is not Gaussian, it is practical to calculate the spectral width through the Root-mean square (RMS) bandwidth by calculating the variance:

$$\text{Variance} = \langle\omega^2\rangle - \langle\omega\rangle^2 = \frac{\int \omega^2 I(\omega)\mathrm{d}\omega}{\int I(\omega)\mathrm{d}\omega} - \left(\frac{\int \omega I(\omega)\mathrm{d}\omega}{\int I(\omega)\mathrm{d}\omega}\right)^2 \tag{5.17}$$

The spectral width can be estimated then as

$$\Delta\omega_{\mathrm{FWHM}} = 2\sqrt{2\ln 2}\cdot \text{Variance} \tag{5.18}$$

The experimental spectra were converted to the frequency domain and then the spectral width was estimated using equations (5.17) and (5.18). The evaluation of spectral broadening of the NER signal as a function of argon gas pressure is presented in Fig. 5.5.

The temporally filtered pulses were then re-compressed to their transform limit. This step is required to show the principal possibility to re-compress the resulting chirped pulses. A Wizzler from Fastlite [84, 85, 86] was used for the characterization of the re-compressed pulses as it allows ultra-short femtosecond pulses to be characterized down to approximately $\tau \approx 4\,\mathrm{fs}$. Measured durations of the re-compressed pulses are shown by the red points in Fig. 5.6. One can see that durations close to the FTL were

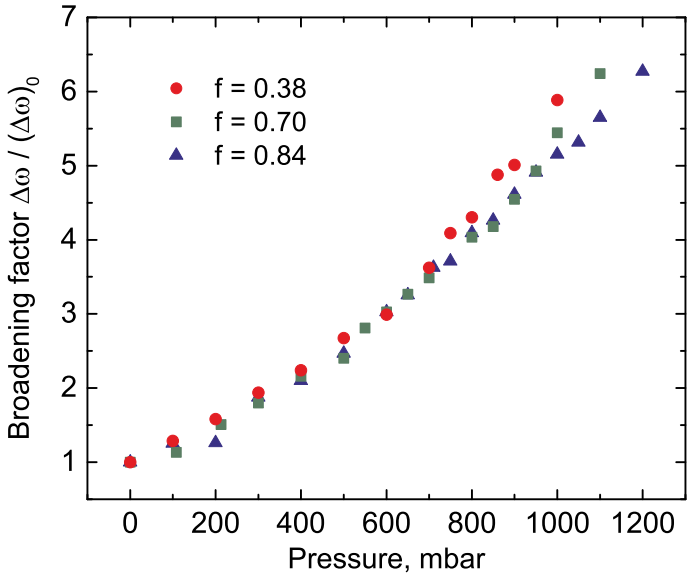

Figure 5.5: The dependence of the spectrum broadening factor on the gas pressure (P_L) for the NER signal. Dots of different colors correspond to different flattening

achieved.

It is obvious, that the shape of the spectral intensity and the spectral phase affect the quality of the re-compressed temporal profile. A more smooth spectral shape allows a better re-compression and higher quality of the re-compressed pulse to be reached. This is visible in Fig. 5.7, where data derived from the Wizzler measurements are presented. The duration of the measured pulses is approximately $\tau_{\mathrm{fwhm}} \approx 5\,\mathrm{fs}$.

It is also worth noting that the few-cycle regime was easily achieved at several levels of ellipticity. The shortest pulse duration at 1 bar pressure in case of two different flattenings was measured to be $\approx 5\,\mathrm{fs}$. The dependence of the re-compressed pulse duration on the gas pressure is shown in Fig. 5.6. In addition, the Fourier Transform Limited (FTL) pulse duration is also shown in the figures.

Currently, there are no devices suitable for high dynamic range characterization of the temporal contrast of few-cycle pulses. Devices such as the Sequoia and Tundra cross-correlators do not support ultra-short pulses and the required spectral width. For instance, it was observed that a substantial part of the pulse spectrum goes through the optics inside a Tundra cross-correlator. Thus, the direct improvement of the temporal contrast was not measured, because it is currently not possible. However, according to the theory of the NER-based filtering technique, the measured extinction coefficient of the cross-polarizers determines the improvement of the temporal contrast. For the demonstrated scheme, the extinction was $> 2.4 \times 10^3$ and thus the improvement of

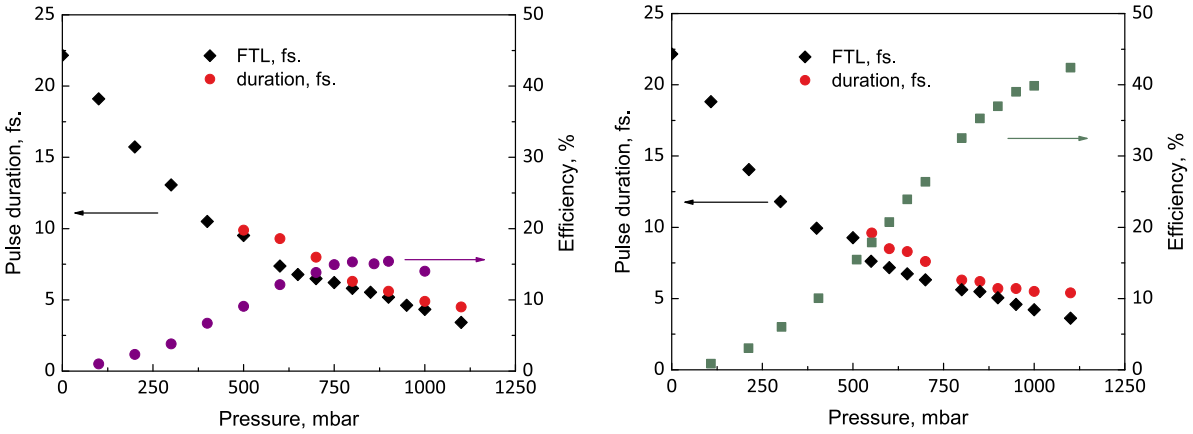

(a) flattening = 0.38

(b) flattening = 0.70

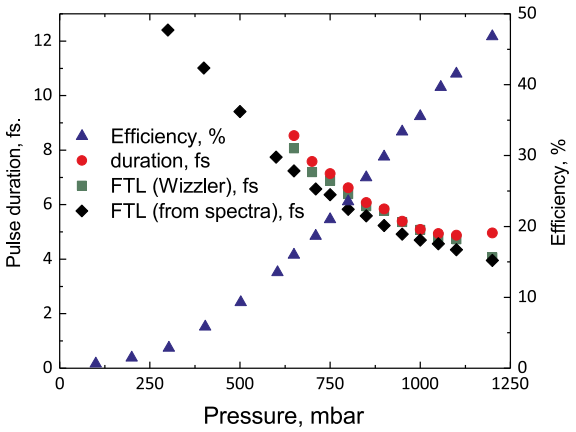

(c) flattening = 0.84

Figure 5.6: Dependence of the pulse duration, FTL and efficiency of NER filtering for different flattening derived from the experimental data

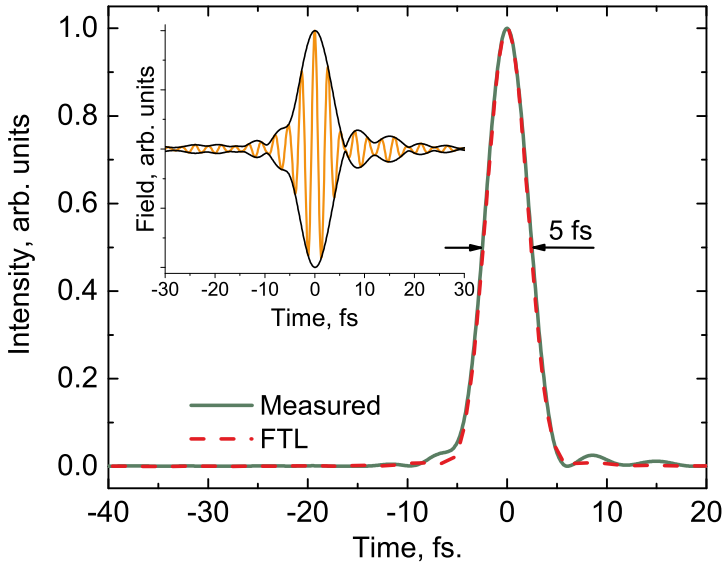

Figure 5.7: Temporal pulse shape reconstruction with (green line) and without (red dashed line) taking into account the spectral phase information for flattening $f = 0.84$ and P = 1100 mbar

the temporal contrast is estimated to be above 3 orders of magnitudes. The spatial parameters of the output beam are improved by the HCF acting as a spatial filter. The spatial intensity distribution shows a perfect Gaussian shape in both directions and a round shape of the output beam mode.

Since the technique is based on a third-order process, it is important to ensure that there is no degradation of the energy stability. The energy stability measured in front of the fibre, after the fibre and after the second polariser (NER signal) are 0.3 %, 0.35 % and 0.53 % RMS respectively.

It is worth noting that NER filtering was applied to pulses with duration of $\tau_{\mathrm{fwhm}} \approx 30$ fs. The resulting pulses have duration 5 fs. This pulse duration is suitable for applications but not for amplification in high-power cascades. Since the temporal filtering is accompanied by significant spectral broadening, one can use longer pulses at the exit of the front-end. Since the longer pulses correspond to a narrower bandwidth, the NER technique might relax the conditions for a millijoule front-end design in terms of the spectrum width which, in its turn, makes the laser system simpler. On the other hand it seems to be more reasonable applying this technology to significantly longer pulses with duration of hundreds of femtoseconds. The NER technique is reasonable to be used with the available fibre-based and thin-disk based lasers with the central wavelength $\lambda_0 = 1030$ nm and a long pulse duration.

To conclude, the technique of temporal filtering by rotation of polarization ellipse in a hollow core fibre filled with noble gases has several advantageous features. Together with a smooth spectral broadening to a level that supports high quality re-compressed pulses of single oscillations, it demonstrates a filtering efficiency of 46%. Taking into account the transmission of the HCF, this value is comparable with the efficiency which can be reached with the commonly used XPW. The filtering efficiency of the NER technique can be improved to above 50 % and the energy level of the seed can be increases to above 1 mJ with a longer HCF. Moreover, the optical scheme does not contain crystal surfaces susceptible to degradation. It is also worth mentioning some disadvantages of the NER comparing to the XPW. The weak side of NER is the input beam coupling with the HCF input. The technique is sensitive to alignment and the filtering efficiency can significantly drop down when the coupling is not accurate.

Conclusions

The signal-to-noise ratio in the time domain of laser pulses is one of the most important laser parameters. The temporal contrast of laser pulses plays a key role in high intensity light-matter interactions involving solid targets. The gradual growth of available laser peak intensities increases the role of pulse contrast and imposes higher requirements for the temporal contrast of ultra-fast pulses used in experiments. The major goal of this work is an investigation of re-compressed laser pulses on the picosecond time scale in the vicinity of the main peak. The current state of the problem with temporal contrast in high peak power laser systems with an emphasis on Ti:Sapphire related technologies has been discussed in details.

A new method for characterization of the coherence within the temporal shape of laser pulses in CPA systems was developed and applied. The diagnostics for high-dynamic range characterization based on a third-order cross-correlator was improved in order to reduce the measurement uncertainty.

A set of commonly used stretcher/compressor configurations were developed and compared aiming to find a possibility to improve the temporal contrast of re-compressed pulses, especially concentrated on steepening the leading front. This includes reflective diffraction grating-based, transmission diffraction grating-based and prisms-based stretcher and compressor schemes. This investigation has identified a coherent pedestal behind the main peak. The coherent pedestal degrades the temporal contrast at the leading edge of the main peak. It was found that it originates from the Ti:Sapphire medium and cannot be cancelled. Moreover, it sets the principal limit of temporal contrast achievable in Ti:Sapphire CPA lasers.

The nonlinear filtering method based on the rotation of the polarization ellipse (NER) in combination with a differentially pumped hollow-core fibre was proposed and investigated. It was found that this method is a good alternative to cross-polarized wave generation (XPW), which is commonly used to improve the temporal contrast.

The new NER technique demonstrates high filtering efficiency of 46%. Simultaneously it allows for a substantial improvement of the temporal contrast to the same level as XPW (10^3-10^4). The NER filtering in a HCF supports a spike-free highly

broadened spectrum and, thus, modulation-free spectral amplitude and phase. This leads to a better re-compression of pulses and improvement of the temporal contrast in the vicinity of the main peak on the femtosecond time scale.

An extension of this method to a longer hollow-core fibre (HCF) may provide an opportunity to use higher input pulse energy (several millijoules and above) and other gases with lower values of the nonlinearity. This may support higher nonlinear filtering efficiency together with even larger broadening, and may allow comparably long pulse of hundreds of femtoseconds to be used as a seed. This relaxes the requirements for the front-end and the technique can be efficiently applied in Yb-based fibre lasers.

Appendix A

Derivation of the formula for the NER efficiency using the Jones matrices

Equation (1.76) describes how to estimate the angle of the ellipse rotation. However it is not enough to understand how the filtering works. In this section I will go through the optical scheme and derive the equation for the formula for the efficiency of the NER technique. This equation was obtained in a collaboration with LOA.

According to the principles of NER shown in Fig. A.1, we take a linearly polarized light, transform it to the elliptic polarization. Then the intensity caused rotation occurs. After that, the second quarter-wave plate compensates back the ellipticity of the polarization for the low intense light, and the vertical polarizer blocks the horizontal component of the polarization.

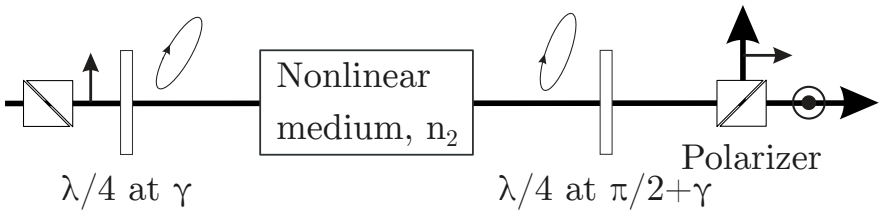

Figure A.1: Principle of nonlinear temporal filtering based on rotation of the polarization ellipse. The first quarter waveplate transforms the linear polarization of the input beam into an elliptical polarization which at low pulse intensity is transformed back into linear polarization by the second quarter waveplate which is crossed with respect to the first one. In case of high intensity and a nonlinear medium between the plates, a polarization rotation will occur resulting in an uncompensated ellipticity at the second waveplate and thus a leak through the polarizer. The input beam must be highly linearly polarized as in the case of XPW

The transformations of the polarization are purely geometric except the rotation of

the ellipse, which is described in section 1.7.3 and therefore one can try to describe the system.

Jones formalism

There is a tool to operate with the polarization components of the complex electric field. This tool is called the Jones calculus [163]. First of all one need to represent our complex field. The Jones formalism suggests to use a matrix for this purpose:

$$E = \begin{pmatrix} E_x \\ E_y \end{pmatrix} = \begin{pmatrix} |E_x|e^{i\varphi} \\ |E_y|e^{i\varphi} \end{pmatrix} \tag{A.1}$$

In order to simulate the polarization change by the optical element one need to calculate the product of the matrix of the corresponding optical element and the matrix describing the orthogonal components of the electric field (A.1). For example let's consider a polarizer. The Jones matrices for the horizontal and vertical polatizers can be expressed as

$$J_{\mathrm{LHP}} = \begin{pmatrix} 1 & 0 \\ 0 & 0 \end{pmatrix}, J_{\mathrm{LVP}} = \begin{pmatrix} 0 & 0 \\ 0 & 1 \end{pmatrix} \tag{A.2}$$

Thus, the change of the polarization state can be derived as

$$\begin{pmatrix} E_x \\ 0 \end{pmatrix} = \begin{pmatrix} 1 & 0 \\ 0 & 0 \end{pmatrix} \cdot \begin{pmatrix} E_x \\ E_y \end{pmatrix} \tag{A.3}$$

One can see that it simply chooses the horizontal component of the polarization. The rotation of the polarization ellipse can be performed by using a rotation matrix:

$$R(\alpha) = \begin{pmatrix} \cos\alpha & -\sin\alpha \\ \sin\alpha & \cos\alpha \end{pmatrix} \tag{A.4}$$

where α is the rotation angle.

The most complicated element in our scheme is the quarter-wave plate. A wave plate can be represented as

$$J_{\mathrm{WP}}(\phi) = \begin{pmatrix} e^{i\phi/2} & 0 \\ 0 & e^{-i\phi/2} \end{pmatrix} \tag{A.5}$$

where ϕ is the introduced phase shift. For instance a half-wave and the quarter-wave plates cause the $\phi = \pi$ and $\phi = \pi/2$ phase shifts, respectively. Since the value of the phase is real $\phi \in \mathbb{R}$ one can use the Euler's formula for the exponential representation

of the complex number and present the equation (A.5) in a different form

$$J_{\mathrm{WP}}(\phi) = \begin{pmatrix} \cos(\phi/2) + i\sin(\phi/2) & 0 \\ 0 & \cos(\phi/2) - i\sin(\phi/2) \end{pmatrix} \tag{A.6}$$

In our case, the quarter-wave plate is aligned to be at the angle γ with respect to the horizontal axis. To obtain a matrix for a rotated optical element, one need to use the rotation matrix (A.4):

$$J_{\mathrm{WP}}(\phi, \alpha) = R(\alpha) \cdot J_{\mathrm{WP}}(\phi) \cdot R^{-1}(\alpha) \tag{A.7}$$

resulting in

$$J_{\mathrm{WP}}(\phi, \alpha) = \begin{pmatrix} \cos(\phi/2) + i\sin(\phi/2)\cos(2\alpha) & i\sin(\phi/2)\sin(2\alpha) \\ i\sin(\phi/2)\sin(2\alpha) & \cos(\phi/2) - i\sin(\phi/2)\cos(2\alpha) \end{pmatrix} \tag{A.8}$$

The quarter-wave plate $\phi = \pi/2$ can be then expressed as

$$J_{\mathrm{QWP}}(\alpha) = \begin{pmatrix} (1 + i\cos(2\alpha))/\sqrt{2} & i\sin(2\alpha)/\sqrt{2} \\ i\sin(2\alpha)/\sqrt{2} & (1 - i\cos(2\alpha))/\sqrt{2} \end{pmatrix} \tag{A.9}$$

Since the first quarter-wave plate is aligned at the angle γ one can simply substitute α by γ. However, in the case of the second quarter-wave plate, the angle $\pi/2 + \gamma$ will lead to the equation

$$J_{\mathrm{QWP}}(\pi/2 + \gamma) = \begin{pmatrix} (1 - i\cos(2\gamma))/\sqrt{2} & -i\sin(2\gamma)/\sqrt{2} \\ -i\sin(2\gamma)/\sqrt{2} & (1 + i\cos(2\gamma))/\sqrt{2} \end{pmatrix} \tag{A.10}$$

To calculate propagation of the electric field through the series of components one need to calculate the product of the corresponding Jones matrices in the reverse order. In the case of NER this leads to

$$E_{\mathrm{NER}} = J_{\mathrm{LVP}} \cdot J_{\mathrm{QWP}}(\pi/2 + \gamma) \cdot R(\theta) \cdot J_{\mathrm{QWP}}(\gamma) \cdot J_{\mathrm{LHP}} \cdot E_{\mathrm{input}} \tag{A.11}$$

One can get

$$E_{\mathrm{NER}} = \begin{pmatrix} 0 \\ -iE_x \sin\theta\cos(2\gamma) \end{pmatrix} \tag{A.12}$$

where θ is the rotation angle of the polarization ellipse caused by the high intensity (1.76) and γ is the rotation angle of the first quarter-wave plate. The intensity of the

field can be found using

$$I = E^{\dagger}E = \begin{pmatrix} E_x^* & E_y^* \end{pmatrix} \cdot \begin{pmatrix} E_x \\ E_y \end{pmatrix} \tag{A.13}$$

Where $E^{\dagger}$ is the conjugate transpose of the field E. This is resulting in

$$I_{\mathrm{NER}} = \sin^2\theta \cos^2(2\gamma)|E_x|^2 \tag{A.14}$$

The input beam is linearly polarized in the horizontal direction $|E_x|^2 = I_{\mathrm{input}}$. Thus, the efficiency can be expressed as

$$\eta = \frac{I_{\mathrm{NER}}}{I_{\mathrm{input}}} = \sin^2\theta \cos^2(2\gamma) \tag{A.15}$$

Bibliography

[1] T. Brabec, ed., *Strong Field Laser Physics*. Springer Series in Optical Sciences, Springer-Verlag New York, 2009.

[2] R. Budriūnas, T. Stanislauskas, J. Adamonis, A. Aleknavičius, G. Veitas, D. Gadonas, S. Balickas, A. Michailovas, and A. Varanavičius, "53 W average power CEP-stabilized OPCPA system delivering 5.5 TW few cycle pulses at 1 kHz repetition rate," *Opt. Express*, vol. 25, pp. 5797–5806, Mar 2017.

[3] W. P. Leemans, A. J. Gonsalves, H.-S. Mao, K. Nakamura, C. Benedetti, C. B. Schroeder, C. Tóth, J. Daniels, D. E. Mittelberger, S. S. Bulanov, J.-L. Vay, C. G. R. Geddes, and E. Esarey, "Multi-GeV Electron Beams from Capillary-Discharge-Guided Subpetawatt Laser Pulses in the Self-Trapping Regime," *Phys. Rev. Lett.*, vol. 113, p. 245002, Dec 2014.

[4] H. Daido, M. Nishiuchi, and A. S. Pirozhkov, "Review of laser-driven ion sources and their applications," *Rep. Prog. Phys.*, vol. 75, no. 5, p. 056401, 2012.

[5] A. Macchi, M. Borghesi, and M. Passoni, "Ion acceleration by superintense laser-plasma interaction," *Rev. Mod. Phys.*, vol. 85, pp. 751–793, May 2013.

[6] M. A. Purvis, V. N. Shlyaptsev, R. Hollinger, C. Bargsten, A. Pukhov, A. Prieto, Y. Wang, B. M. Luther, L. Yin, S. Wang, and J. J. Rocca, "Relativistic plasma nanophotonics for ultrahigh energy density physics," *Nat. Photon.*, vol. 7, pp. 796–800, Oct 2013.

[7] G. A. Mourou, T. Tajima, and S. V. Bulanov, "Optics in the relativistic regime," *Rev. Mod. Phys.*, vol. 78, pp. 309–371, Apr 2006.

[8] S. M. Hooker, "Developments in laser-driven plasma accelerators," *Nat. Photon.*, vol. 7, pp. 775–782, Oct 2013.

[9] W. P. Leemans, B. Nagler, A. J. Gonsalves, C. Tóth, K. Nakamura, C. G. R. Geddes, E. Esarey, C. B. Schroeder, and S. M. Hooker, "GeV electron beams from a centimetre-scale accelerator," *Nat. Phys.*, vol. 2, p. 696, Sep 2006.

[10] M. Kaluza, J. Schreiber, M. I. K. Santala, G. D. Tsakiris, K. Eidmann, J. Meyer-ter Vehn, and K. J. Witte, "Influence of the laser prepulse on proton acceleration in thin-foil experiments," *Phys. Rev. Lett.*, vol. 93, p. 045003, Jul 2004.

[11] P. McKenna, D. Carroll, O. Lundh, F. Nurnberg, K. Markey, S. Bandyopadhyay, D. Batani, and R. Evans, "Effects of front surface plasma expansion on proton acceleration in ultraintense laser irradiation of foil targets," *Laser Part. Beams*, vol. 26, pp. 591–596, 12 2008.

[12] G. Sansone, L. Poletto, and M. Nisoli, "High-energy attosecond light sources," *Nat. Photon.*, vol. 5, pp. 655–663, Nov 2011.

[13] T. Brabec and F. Krausz, "Intense few-cycle laser fields: Frontiers of nonlinear optics," *Rev. Mod. Phys.*, vol. 72, pp. 545–591, Apr 2000.

[14] B. Dromey, D. Adams, R. Hörlein, Y. Nomura, S. G. Rykovanov, D. C. Carroll, P. S. Foster, S. Kar, K. Markey, P. McKenna, D. Neely, M. Geissler, G. D. Tsakiris, and M. Zepf, "Diffraction-limited performance and focusing of high harmonics from relativistic plasmas," *Nat. Phys.*, vol. 5, p. 146, Jan 2009.

[15] C. Thaury and F. Quéré, "High-order harmonic and attosecond pulse generation on plasma mirrors: basic mechanisms," *J. Phys. B*, vol. 43, no. 21, p. 213001, 2010.

[16] S. Kahaly, S. Monchocé, H. Vincenti, T. Dzelzainis, B. Dromey, M. Zepf, P. Martin, and F. Quéré, "Direct Observation of Density-Gradient Effects in Harmonic Generation from Plasma Mirrors," *Phys. Rev. Lett.*, vol. 110, p. 175001, Apr 2013.

[17] M. P. Kalashnikov, E. Risse, H. Schönnagel, and W. Sandner, "Double chirped-pulse-amplification laser: a way to clean pulses temporally," *Opt. Lett.*, vol. 30, pp. 923–925, Apr 2005.

[18] B. Dromey, S. Kar, M. Zepf, and P. Foster, "The plasma mirror—a subpicosecond optical switch for ultrahigh power lasers," *Rev. Sci. Instrum.*, vol. 75, no. 3, pp. 645–649, 2004.

[19] S. Kühn, M. Dumergue, S. Kahaly, S. Mondal, M. Füle, T. Csizmadia, B. Farkas, B. Major, Z. Várallyay, E. Cormier, M. Kalashnikov, F. Calegari, M. Devetta, F. Frassetto, E. Månsson, L. Poletto, S. Stagira, C. Vozzi, M. Nisoli, P. Rudawski, S. Maclot, F. Campi, H. Wikmark, C. L. Arnold, C. M. Heyl, P. Johnsson, A. L'Huillier, R. Lopez-Martens, S. Haessler, M. Bocoum, F. Boehle, A. Vernier, G. Iaquaniello, E. Skantzakis, N. Papadakis, C. Kalpouzos, P. Tzallas, F. Lépine, D. Charalambidis, K. Varjú, K. Osvay, and G. Sansone, "The ELI-ALPS facility: the next generation of attosecond sources," *J. Phys. B: At. Mol. Opt. Phys.*, vol. 50, no. 13, p. 132002, 2017.

[20] S. A. Akhmanov, V. A. Vysloukh, and A. S. Chirkin, *Optics of Femtosecond Laser Pulses*. AIP-Press, 1992.

[21] R. W. Boyd, *Nonlinear Optics (Third Edition)*. Burlington, Vermont: Academic Press, third edition ed., 2008.

[22] R. DeSalvo, M. Sheik-Bahae, A. A. Said, D. J. Hagan, and E. W. V. Stryland, "Z-scan measurements of the anisotropy of nonlinear refraction and absorption in crystals," *Opt. Lett.*, vol. 18, pp. 194–196, Feb 1993.

[23] P. D. Maker, R. W. Terhune, and C. M. Savage, "Intensity-Dependent Changes in the Refractive Index of Liquids," *Phys. Rev. Lett.*, vol. 12, pp. 507–509, May 1964.

[24] P. D. Maker and R. W. Terhune, "Study of Optical Effects Due to an Induced Polarization Third Order in the Electric Field Strength," *Phys. Rev.*, vol. 137, pp. A801–A818, Feb 1965.

[25] J. Davis and W. Clements, "Laser program annual report, 1974," Tech. Rep. UCRL 50021-74, Lawrence Livermore Laboratory, Livermore, CA 94550, March 1975.

[26] S. E. Stokowski, M. J. Weber, R. A. Saroyan, and W. F. Hagen, "Requirements and new materials for fusion laser systems," (United States), 1977.

[27] R. W. Boyd, S. G. Lukishova, and Y. R. Shen, *Self-focusing: Past and Present*. Springer-Verlag New York, 2009.

[28] G. Fibich and A. L. Gaeta, "Critical power for self-focusing in bulk media and in hollow waveguides," *Opt. Lett.*, vol. 25, pp. 335–337, Mar 2000.

[29] L. M. Frantz and J. S. Nodvik, "Theory of pulse propagation in a laser amplifier," *J. Appl. Phys.*, vol. 34, no. 8, pp. 2346–2349, 1963.

[30] C. L. Blanc, P. Curley, and F. Salin, "Gain-narrowing and gain-shifting of ultrashort pulses in Ti:Sapphire amplifiers," *Opt. Commun.*, vol. 131, no. 4, pp. 391 – 398, 1996.

[31] S. Backus, C. G. Durfee III, M. M. Murnane, and H. C. Kapteyn, "High power ultrafast lasers," *Rev. Sci. Instrum.*, vol. 69, no. 3, pp. 1207–1223, 1998.

[32] M. Kalashnikov, K. Osvay, I. Lachko, H. Schönnagel, and W. Sandner, "Suppression of gain narrowing in multi-tw lasers with negatively and positively chirped pulse amplification," *Appl. Phys. B*, vol. 81, pp. 1059–1062, Dec 2005.

[33] T. Damm, M. Kaschke, F. Noack, and B. Wilhelmi, "Compression of picosecond pulses from a solid-state laser using self-phase modulation in graded-index fibers," *Opt. Lett.*, vol. 10, pp. 176–178, Apr 1985.

[34] D. Strickland and G. Mourou, "Compression of amplified chirped optical pulses," *Opt. Commun.*, vol. 55, no. 6, pp. 447 – 449, 1985.

[35] O. E. Martinez, "Grating and prism compressors in the case of finite beam size," *J. Opt. Soc. Am. B*, vol. 3, pp. 929–934, Jul 1986.

[36] O. Martinez, "3000 times grating compressor with positive group velocity dispersion: Application to fiber compensation in 1.3-1.6 μm region," *IEEE J. Quantum Electron*, vol. 23, pp. 59–64, Jan 1987.

[37] W. Koechner, *Solid-State Laser Engineering*. Springer Series in Optical Sciences, Springer-Verlag New York, 2006.

[38] F. Billhardt, M. Kalashnikov, P. Nickles, and I. Will, "A high-contrast psterawatt Nd: glass laser system with fiberless chirped pulse amplification," *Opt. Commun.*, vol. 98, no. 1, pp. 99 – 104, 1993.

[39] D. E. Spence, P. N. Kean, and W. Sibbett, "60-fsec pulse generation from a self-mode-locked Ti:sapphire laser," *Opt. Lett.*, vol. 16, pp. 42–44, Jan 1991.

[40] A. Dubietis, G. Jonušauskas, and A. Piskarskas, "Powerful femtosecond pulse generation by chirped and stretched pulse parametric amplification in BBO crystal," *Opt. Commun.*, vol. 88, no. 4–6, pp. 437 – 440, 1992.

[41] H. Kiriyama, M. Nishiuchi, A. S. Pirozhkov, Y. Fukuda, H. Sakaki, A. Sagisaka, N. P. Dover, K. Kondo, K. snd Nishitani, K. Ogura, M. Mori, Y. Miyasaka, M. Kando, and K. Kondo, "J–KAREN–P Laser Facility producing 10^{22} W/cm^2 at 0.1 Hz," in *The 6th Advanced Lasers and Photon Sources (ALPS'17)*, (Yokohama, Japan), Apr 2017.

[42] A. A. Andreev, R. Sonobe, S. Kawata, S. Miyazaki, K. Sakai, K. Miyauchi, T. Kikuchi, K. Platonov, and K. Nemoto, "Effect of a laser prepulse on fast ion generation in the interaction of ultra-short intense laser pulses with a limited-mass foil target," *Plasma Phys. Contr. Fusion*, vol. 48, no. 11, p. 1605, 2006.

[43] D. Batani, R. Jafer, R. Redaelli, R. Dezulian, O. Lundh, F. Lindau, A. Persson, K. Osvay, C.-G. Wahlström, D. Carroll, P. McKenna, A. Flacco, V. Malka, and M. Veltcheva, "Effects of laser prepulse on proton generation," *Nucl. Instrum. Methods Phys. Res. Sec. A*, vol. 620, no. 1, pp. 76 – 82, 2010.

[44] P. F. Moulton, "Spectroscopic and laser characteristics of Ti:Al_2O_3," *J. Opt. Soc. Am. B*, vol. 3, pp. 125–133, Jan 1986.

[45] O. Svelto, S. Taccheo, and C. Svelto, "Analysis of amplified spontaneous emission: some corrections to the Linford formula," *Opt. Commun.*, vol. 149, no. 4, pp. 277 – 282, 1998.

[46] S. Keppler, A. Sävert, J. Körner, M. Hornung, H. Liebetrau, J. Hein, and M. C. Kaluza, "The generation of amplified spontaneous emission in high-power CPA laser systems," *Laser Photon. Rev.*, vol. 10, no. 2, pp. 264–277, 2016.

[47] M. Kalashnikov, A. Andreev, and H. Schönnagel, "Limits of the temporal contrast for CPA lasers with beams of high aperture," in *Proc. SPIE*, vol. 7501, pp. 750104–750104–9, 2009.

[48] M. P. Kalashnikov and K. Osvay, "High peak power Ti:Sapphire lasers: temporal contrast and spectral narrowing issues," vol. 5975, pp. 59750E–59750E–12, 2006.

[49] A. Offner, "Unit power maging catoptric anastigmat," Jul 1973.

[50] E. Treacy, "Optical pulse compression with diffraction gratings," *IEEE J. Quantum Electron.*, vol. 5, pp. 454–458, Sep 1969.

[51] A. Stingl, C. Spielmann, F. Krausz, and R. Szipöcs, "Generation of 11-fs pulses from a Ti:sapphire laser without the use of prisms," *Opt. Lett.*, vol. 19, pp. 204–206, Feb 1994.

[52] W. Dietel, J. J. Fontaine, and J.-C. Diels, "Intracavity pulse compression with glass: a new method of generating pulses shorter than 60 fsec," *Opt. Lett.*, vol. 8, pp. 4–6, Jan 1983.

[53] G. Cheriaux, P. Rousseau, F. Salin, J. P. Chambaret, B. Walker, and L. F. Dimauro, "Aberration-free stretcher design for ultrashort-pulse amplification," *Opt. Lett.*, vol. 21, pp. 414–416, Mar 1996.

[54] O. E. Martinez, J. P. Gordon, and R. L. Fork, "Negative group-velocity dispersion using refraction," *J. Opt. Soc. Am. A*, vol. 1, pp. 1003–1006, Oct 1984.

[55] R. L. Fork, O. E. Martinez, and J. P. Gordon, "Negative dispersion using pairs of prisms," *Opt. Lett.*, vol. 9, pp. 150–152, May 1984.

[56] F. J. Duarte, "Generalized multiple-prism dispersion theory for laser pulse compression: higher order phase derivatives," *Appl. Phys. B*, vol. 96, pp. 809–814, Sep 2009.

[57] M. Born and E. Wolf, *Principles of Optics*. Cambridge University Press, 1999.

[58] F. Druon, M. Hanna, G. Lucas-Leclin, Y. Zaouter, D. Papadopoulos, and P. Georges, "Simple and general method to calculate the dispersion properties of complex and aberrated stretchers-compressors," *J. Opt. Soc. Am. B*, vol. 25, pp. 754–762, May 2008.

[59] M. P. Kalashnikov, H. Schönnagel, and W. Sandner, "High temporal contrast front end with a CaF_2-based XPW temporal filter for high intensity lasers," *AIP Conf. Proc.*, vol. 1465, no. 1, pp. 13–17, 2012.

[60] S. E. Harris and R. W. Wallace, "Acousto-optic tunable filter∗," *J. Opt. Soc. Am.*, vol. 59, pp. 744–747, Jun 1969.

[61] R. Dixon, "Acoustic diffraction of light in anisotropic media," *IEEE Journal of Quantum Electronics*, vol. 3, pp. 85–93, February 1967.

[62] P. Tournois, "Acousto-optic programmable dispersive filter for adaptive compensation of group delay time dispersion in laser systems," *Opt. Commun.*, vol. 140, no. 4–6, pp. 245 – 249, 1997.

[63] F. Verluise, V. Laude, J.-P. Huignard, P. Tournois, and A. Migus, "Arbitrary dispersion control of ultrashort optical pulses with acoustic waves," *J. Opt. Soc. Am. B*, vol. 17, pp. 138–145, Jan 2000.

[64] D. Kaplan and P. Tournois, "Theory and performance of the acousto optic programmable dispersive filter used for femtosecond laser pulse shaping," *J. Phys. IV France*, vol. 12, no. 5, pp. 69–75, 2002.

[65] Oksenhendler, T. and Kaplan, D. and Tournois, P. and Greetham, G.M. and Estable, F., "Intracavity acousto-optic programmable gain control for ultra-wideband regenerative amplifiers," *Appl. Phys. B*, vol. 83, no. 4, p. 491, 2006.

[66] "Suppression over High Dynamic Range of ASE at the Rising Edge of Ultraintense Femtosecond Pulses (SHARP), HPRI-CT-2001-50037," 2001 – 2004.

[67] A. Jullien, O. Albert, F. Burgy, G. Hamoniaux, J.-P. Rousseau, J.-P. Chambaret, F. Augé-Rochereau, G. Chériaux, J. Etchepare, N. Minkovski, and S. M. Saltiel, "10^{10} temporal contrast for femtosecond ultraintense lasers by cross-polarized wave generation," *Opt. Lett.*, vol. 30, pp. 920–922, Apr 2005.

[68] J. Itatani, J. Faure, M. Nantel, G. Mourou, and S. Watanabe, "Suppression of the amplified spontaneous emission in chirped-pulse-amplification lasers by clean high-energy seed-pulse injection," *Opt. Commun.*, vol. 148, no. 1, pp. 70–74, 1998.

[69] H. C. Kapteyn, M. M. Murnane, A. Szoke, and R. W. Falcone, "Prepulse energy suppression for high-energy ultrashort pulses using self-induced plasma shuttering," *Opt. Lett.*, vol. 16, pp. 490–492, Apr 1991.

[70] C. Thaury, F. Quéré, J.-P. Geindre, A. Levy, T. Ceccotti, P. Monot, M. Bougeard, F. Réau, P. d'Oliveira, P. Audebert, R. Marjoribanks, and P. Martin, "Plasma mirrors for ultrahigh-intensity optics," *Nat. Phys.*, vol. 3, pp. 424–429, Jun 2007.

[71] A. Lévy, T. Ceccotti, P. D'Oliveira, F. Réau, M. Perdrix, F. Quéré, P. Monot, M. Bougeard, H. Lagadec, P. Martin, J.-P. Geindre, and P. Audebert, "Double plasma mirror for ultrahigh temporal contrast ultraintense laser pulses," *Opt. Lett.*, vol. 32, pp. 310–312, Feb 2007.

[72] D. C. Hutchings, J. S. Aitchison, and J. M. Arnold, "Nonlinear refractive coupling and vector solitons in anisotropic cubic media," *J. Opt. Soc. Am. B*, vol. 14, pp. 869–879, Apr 1997.

[73] N. Minkovski, G. I. Petrov, S. M. Saltiel, O. Albert, and J. Etchepare, "Nonlinear polarization rotation and orthogonal polarization generation experienced in a single-beam configuration," *J. Opt. Soc. Am. B*, vol. 21, pp. 1659–1664, Sep 2004.

[74] S. Kourtev, N. Minkovski, L. Canova, A. Jullien, O. Albert, and S. M. Saltiel, "Improved nonlinear cross-polarized wave generation in cubic crystals by optimization of the crystal orientation," *J. Opt. Soc. Am. B*, vol. 26, pp. 1269–1275, Jul 2009.

[75] A. Jullien, L. Canova, O. Albert, D. Boschetto, L. Antonucci, Y.-H. Cha, J. Rousseau, P. Chaudet, G. Chériaux, J. Etchepare, S. Kourtev, N. Minkovski,

and S. Saltiel, "Spectral broadening and pulse duration reduction during cross-polarized wave generation: influence of the quadratic spectral phase," *Appl. Phys. B*, vol. 87, pp. 595–601, Jun 2007.

[76] M. P. Kalashnikov, K. Osvay, G. Priebe, L. Ehrentraut, S. Steinke, and W. Sandner, "Temporal contrast of high intensity laser systems above 10^{11} with double CPA technique," in *American Institute of Physics Conference Series* (K. Osvay, P. Dombi, J. Andras Fülöp, and K. Varjú, eds.), vol. 1462 of *American Institute of Physics Conference Series*, pp. 108–111, Jul 2012.

[77] D. Homoelle, A. L. Gaeta, V. Yanovsky, and G. Mourou, "Pulse contrast enhancement of high-energy pulses by use of a gas-filled hollow waveguide," *Opt. Lett.*, vol. 27, pp. 1646–1648, Sep 2002.

[78] K. Sala and M. C. Richardson, "A passive nonresonant technique for pulse contrast enhancement and gain isolation," *J. Appl. Phys.*, vol. 49, no. 4, pp. 2268–2276, 1978.

[79] M. P. Kalashnikov, E. Risse, H. Schönnagel, A. Husakou, J. Herrmann, and W. Sandner, "Characterization of a nonlinear filter for the front-end of a high contrast double-CPA Ti:sapphire laser," *Opt. Express*, vol. 12, pp. 5088–5097, Oct 2004.

[80] A. Jullien, F. Augé-Rochereau, G. Chériaux, J.-P. Chambaret, P. d'Oliveira, T. Auguste, and F. Falcoz, "High-efficiency, simple setup for pulse cleaning at the millijoule level by nonlinear induced birefringence," *Opt. Lett.*, vol. 29, pp. 2184–2186, Sep 2004.

[81] H. J. Liu, Q. B. Sun, N. Huang, J. Wen, and Z. L. Wang, "Highly efficient pulse cleaner via nonlinear ellipse rotation in liquid CS_2 for ultrashort pulses," *Opt. Lett.*, vol. 38, pp. 1838–1840, Jun 2013.

[82] G. Agrawal, *Nonlinear Fiber Optics*. Optics and Photonics, Elsevier Science, 2001.

[83] R. L. Sutherland, D. G. McLean, and S. Kirkpatrick, *Handbook of Nonlinear Optics*. Boca Raton, Florida: CRC Press, second edition ed., 2003.

[84] T. Oksenhendler, S. Coudreau, N. Forget, V. Crozatier, S. Grabielle, R. Herzog, O. Gobert, and D. Kaplan, "Self-referenced spectral interferometry," *Appl. Phys. B*, vol. 99, pp. 7–12, Apr 2010.

[85] A. Moulet, S. Grabielle, C. Cornaggia, N. Forget, and T. Oksenhendler, "Single-shot, high-dynamic-range measurement of sub-15 fs pulses by self-referenced spectral interferometry," *Opt. Lett.*, vol. 35, pp. 3856–3858, Nov 2010.

[86] S. Grabielle, A. Moulet, N. Forget, V. Crozatier, S. Coudreau, R. Herzog, T. Oksenhendler, C. Cornaggia, and O. Gobert, "Self-referenced spectral interferometry cross-checked with SPIDER on sub-15fs pulses," *Nucl. Instrum. Methods Phys. Res. A*, vol. 653, no. 1, pp. 121 – 125, 2011.

[87] T. Oksenhendler, P. Bizouard, O. Albert, S. Bock, and U. Schramm, "High dynamic, high resolution and wide range single shot temporal pulse contrast measurement," *Opt. Express*, vol. 25, pp. 12588–12600, May 2017.

[88] S. Luan, M. H. R. Hutchinson, R. A. Smith, and F. Zhou, "High dynamic range third-order correlation measurement of picosecond laser pulse shapes," *Meas. Sci. Technol.*, vol. 4, no. 12, p. 1426, 1993.

[89] T. Feurer, S. Niedermeier, and R. Sauerbrey, "Measuring the temporal intensity of ultrashort laser pulses by triple correlation," *Appl. Phys. B*, vol. 66, no. 2, pp. 163–168, 1998.

[90] K. Osvay, I. Ross, J. Lister, and C. Hooker, "High dynamic range measurement of temporal shape and contrast of ultrashort UV pulses," *Appl. Phys. B*, vol. 69, no. 1, pp. 19–23, 1999.

[91] "Sequoia cross-correlator, http://www.amplitude-technologies.com," 2018.

[92] "Thundra cross-correlator, http://www.ultrafast-innovations.com," 2018.

[93] C. Dorrer, J. Bromage, and J. D. Zuegel, "High-dynamic-range single-shot cross-correlator based on an optical pulse replicator," *Opt. Express*, vol. 16, pp. 13534–13544, Sep 2008.

[94] Y. Wang, J. Ma, J. Wang, P. Yuan, G. Xie, X. Ge, F. Liu, X. Yuan, H. Zhu, and L. Qian, "Single-shot measurement of $>10^{10}$ pulse contrast for ultra-high peak-power lasers," *Sci. Rep.*, vol. 4, Jan 2014.

[95] A. Kon, M. Nishiuchi, H. Kiriyama, K. Ogura, M. Mori, H. Sakaki, M. Kando, and K. Kondo, "High-dynamic-range cross-correlator for shot-to-shot measurement of temporal contrast," *JAPAN J. Appl. Phys.*, vol. 56, no. 1, p. 012701, 2017.

[96] Amplitude Technologies, *Sequoia. High dynamic third order cross correlator. User's manual.*

[97] J. Bohus, J. Budai, M. Kalashnikov, and K. Osvay, "An all-reflective polarization rotator," in *Proc. SPIE*, pp. 10238 – 10238 – 9, 2017.

[98] T. Ditmire, A. M. Rubenchik, D. Eimerl, and M. D. Perry, "Effects of cubic nonlinearity on frequency doubling of high-power laser pulses," *J. Opt. Soc. Am. B*, vol. 13, pp. 649–655, Apr 1996.

[99] C. Hooker, Y. Tang, O. Chekhlov, J. Collier, E. Divall, K. Ertel, S. Hawkes, B. Parry, and P. P. Rajeev, "Improving coherent contrast of petawatt laser pulses," *Opt. Express*, vol. 19, pp. 2193–2203, Jan 2011.

[100] S. K. Lee, J. H. Sung, H. W. Lee, T. M. Jeong, and C. H. Nam, "Pre-pedestal generation by post-pedestal in high power CPA lasers," in *International Conference on Ultrahigh Intensity Lasers*, (Goa, India), Oct 2014.

[101] Y. Tang, C. Hooker, O. Chekhlov, S. Hawkes, J. Collier, and P. P. Rajeev, "Transmission grating stretcher for contrast enhancement of high power lasers," *Opt. Express*, vol. 22, pp. 29363–29374, Dec 2014.

[102] Y. Huang, C. Zhang, Y. Xu, D. Li, Y. Leng, R. Li, and Z. Xu, "Ultrashort pulse temporal contrast enhancement based on noncollinear optical-parametric amplification," *Opt. Lett.*, vol. 36, pp. 781–783, Mar 2011.

[103] A. B. Sharba, G. Nersisyan, M. Zepf, N. H. Stuart, R. A. Smith, M. Borghesi, and G. Sarri, "Generation of high contrast and high spatial quality idler from a low-gain optical parametric amplifier," *Appl. Opt.*, vol. 55, pp. 9341–9346, Nov 2016.

[104] J. Ma, P. Yuan, J. Wang, Y. Wang, G. Xie, H. Zhu, and L. Qian, "Spatiotemporal noise characterization for chirped-pulse amplification systems," vol. 6, p. 6192, Feb 2015.

[105] Z. Li, S. Tokita, S. Matsuo, K. Sueda, T. Kurita, T. Kawasima, and N. Miyanaga, "Scattering pulse-induced temporal contrast degradation in chirped-pulse amplification lasers," *Opt. Express*, vol. 25, pp. 21201–21215, Sep 2017.

[106] K. F. Wall, R. L. Aggarwal, M. D. Sciacca, H. J. Zeiger, R. E. Fahey, and A. J. Strauss, "Optically induced nonresonant changes in the refractive index of Ti:Al_2O_3," *Opt. Lett.*, vol. 14, pp. 180–182, Feb 1989.

[107] I. H. Malitson and M. J. Dodge, "Refractive index and birefringence of synthetic sapphire," *J. Opt. Soc. Am.*, vol. 62, Nov 1972.

[108] W. J. Tropf and M. E. Thomas, "Aluminum Oxide (Al_2O_3) Revisited," in *Handbook of Optical Constants of Solids* (E. D. Palik, ed.), pp. 653 – 682, Burlington: Academic Press, 1997.

[109] N. Khodakovskiy, M. Kalashnikov, E. Gontier, F. Falcoz, and P.-M. Paul, "Degradation of picosecond temporal contrast of Ti:sapphire lasers with coherent pedestals," *Opt. Lett.*, vol. 41, pp. 4441–4444, Oct 2016.

[110] N. Didenko, A. Konyashchenko, A. Lutsenko, and S. Tenyakov, "Contrast degradation in a chirped-pulse amplifier due to generation of prepulses by postpulses," *Opt. Express*, vol. 16, pp. 3178–3190, Mar 2008.

[111] D. N. Schimpf, E. Seise, J. Limpert, and A. Tünnermann, "The impact of spectral modulations on the contrast of pulses of nonlinear chirped-pulse amplification systems," *Opt. Express*, vol. 16, pp. 10664–10674, Jul 2008.

[112] C. Dorrer and J. Bromage, "Impact of high-frequency spectral phase modulation on the temporal profile of short optical pulses," *Opt. Express*, vol. 16, pp. 3058–3068, Mar 2008.

[113] O. Morice, "Miró: Complete modeling and software for pulse amplification and propagation in high-power laser systems," *Opt. Eng.*, vol. 42, no. 6, pp. 1530–1541, 2003.

[114] P. Donnat, G. Gallice, N. L'Hullier, O. Morice, D. Nassiet, T. Porcher, X. Ribeyre, V. Rivoire, and C. Treimany, *MIRÓ V5$_\epsilon$ Reference manual*. Commissariat à l'Energie Atomique (CEA/CESTA), 2002.

[115] F. Arecchi and R. Bonifacio, "Theory of optical maser amplifiers," *IEEE J. Quantum Electron.*, vol. 1, pp. 169–178, Jul 1965.

[116] "SCHOTT Technical Information. Advanced Optics. TIE-28 Bubbles and Inclusions in Optical Glass," May 2016.

[117] G. Cheriaux, G. Rey, S. Ferre, F. Auge, J. P. Chambaret, and P. D'Oliveira, "ASE contrast improvement in CPA ultra-intense laser chain," in *Lasers and Electro-Optics, 2002. CLEO '02. Technical Digest. Summaries of Papers Presented at the*, pp. 51–52 vol.1, May 2002.

[118] A. Verhoef, J. Seres, K. Schmid, Y. Nomura, G. Tempea, L. Veisz, and F. Krausz, "Compression of the pulses of a Ti:sapphire laser system to 5 femtoseconds at 0.2 terawatt level," *Appl. Phys. B*, vol. 82, no. 4, pp. 513–517, 2006.

[119] H. Kiriyama, M. Mori, Y. Nakai, T. Shimomura, M. Tanoue, A. Akutsu, S. Kondo, S. Kanazawa, H. Okada, T. Motomura, H. Daido, T. Kimura, and T. Tajima, "High-contrast, high-intensity laser pulse generation using a nonlinear preamplifier in a Ti:sapphire laser system," *Opt. Lett.*, vol. 33, pp. 645–647, Apr 2008.

[120] H. Kiriyama, M. Mori, Y. Nakai, T. Shimomura, H. Sasao, M. Tanoue, S. Kanazawa, D. Wakai, F. Sasao, H. Okada, I. Daito, M. Suzuki, S. Kondo, K. Kondo, A. Sugiyama, P. R. Bolton, A. Yokoyama, H. Daido, S. Kawanishi, T. Kimura, and T. Tajima, "High temporal and spatial quality petawatt-class Ti:sapphire chirped-pulse amplification laser system," *Opt. Lett.*, vol. 35, pp. 1497–1499, May 2010.

[121] T. J. Yu, S. K. Lee, J. H. Sung, J. W. Yoon, T. M. Jeong, and J. Lee, "Generation of high-contrast, 30 fs, 1.5 PW laser pulses from chirped-pulse amplification Ti:sapphire laser," *Opt. Express*, vol. 20, pp. 10807–10815, May 2012.

[122] A. Fernandez, L. Zhu, A. J. Verhoef, D. Sidorov-Biryukov, C. H. Liu, K. H. Liao, A. Galvanauskas, S. Kane, A. Pugzlys, and A. Baltuška, "Versatile Yb-fiber-amplifier-based CEP-stable front-end for OPCPA," in *CLEO/Europe - EQEC 2009 - European Conference on Lasers and Electro-Optics and the European Quantum Electronics Conference*, pp. 1–1, June 2009.

[123] G. Cerullo, A. Baltuška, O. Mücke, and C. Vozzi, "Few-optical-cycle light pulses with passive carrier-envelope phase stabilization," *Laser Photon. Rev.*, vol. 5, no. 3, pp. 323–351, 2011.

[124] R. B. unas, T. Stanislauskas, and A. Varanavičius, "Passively CEP-stabilized frontend for few cycle terawatt OPCPA system," *Journal of Optics*, vol. 17, no. 9, p. 094008, 2015.

[125] E. T. J. Nibbering, G. Grillon, M. A. Franco, B. S. Prade, and A. Mysyrowicz, "Determination of the inertial contribution to the nonlinear refractive index of air, N_2, and O_2 by use of unfocused high-intensity femtosecond laser pulses," *J. Opt. Soc. Am. B*, vol. 14, pp. 650–660, Mar 1997.

[126] A. M. Zheltikov, "An analytical model of the rotational Raman response function of molecular gases," *J. Raman Spectrosc.*, vol. 39, no. 6, pp. 756–765, 2008.

[127] B. F. Gächter and J. A. Koningstein, "Zero phonon transitions and interacting Jahn-Teller phonon energies from the fluorescence spectrum of $\alpha-Al_2O_3:Ti^{3+}$," *J. Chem. Phys.*, vol. 60, no. 5, pp. 2003–2006, 1974.

[128] M. Yamaga, Y. Gao, F. Rasheed, K. P. O'Donnell, B. Henderson, and B. Cockayne, "Radiative and non-radiative decays from the excited state of Ti^{3+} ions in oxide crystals," *Appl. Phys. B*, vol. 51, no. 5, pp. 329–335, 1990.

[129] S. García-Revilla, F. Rodríguez, R. Valiente, and M. Pollnau, "Optical spectroscopy of $Al_2O_3:Ti^{3+}$ single crystal under hydrostatic pressure. The influence on the Jahn-Teller coupling," *J. Phys. Condens. Matter*, vol. 14, no. 3, p. 447, 2002.

[130] H. Kuzmany, *Solid-State Spectroscopy*. Springer-Verlag Berlin Heidelberg, 2009.

[131] "HORIBA, Ultra Low Frequency Raman Module for LabRAM HD Evolution, http://www.horiba.com/uk/scientific/products/raman-spectroscopy/accessories/ultra-low-frequency-raman-module/," 2017.

[132] E. Speiser, N. Esser, S. Wippermann, and W. G. Schmidt, "Surface vibrational Raman modes of In:Si(111)(4×1) and (8×2) nanowires," *Phys. Rev. B*, vol. 94, p. 075417, Aug 2016.

[133] M. Kadleíková, J. Breza, and M. Veselý, "Raman spectra of synthetic sapphire," *Microelectronics J.*, vol. 32, no. 12, pp. 955 – 958, 2001.

[134] S. P. S. Porto and R. S. Krishnan, "Raman effect of corundum," *J. Chem. Phys.*, vol. 47, no. 3, pp. 1009–1012, 1967.

[135] B. Henderson and G. F. Imbusch, *Optical Spectroscopy of Inorganic Solids*. Monographs on the physics and chemistry of materials, Oxford University Press, 1989.

[136] Y.-X. Yan, E. B. Gamble, and K. A. Nelson, "Impulsive stimulated scattering: General importance in femtosecond laser pulse interactions with matter, and spectroscopic applications," *The Journal of Chemical Physics*, vol. 83, no. 11, pp. 5391–5399, 1985.

[137] Y.-X. Yan and K. A. Nelson, "Impulsive stimulated light scattering. i. general theory," *The Journal of Chemical Physics*, vol. 87, no. 11, pp. 6240–6256, 1987.

[138] T. E. Stevens, J. Kuhl, and R. Merlin, "Coherent phonon generation and the two stimulated raman tensors," *Phys. Rev. B*, vol. 65, p. 144304, Mar 2002.

[139] T. Dekorsy, G. Cho, and H. Kurz, "Coherent phonons in condensed media," in *Light Scattering in Solids VIII. Topics in Applied Physics, vol. 76* (M. Cardona and G. Güntherodt, eds.), ch. 4, pp. 169–209, Berlin, Heidelberg: Springer, 2000.

[140] R. Merlin, "Generating coherent THz phonons with light pulses," *Solid State Commun.*, vol. 102, no. 2, pp. 207 – 220, 1997. Highlights in Condensed Matter Physics and Materials Science.

[141] A. Ricci, A. Jullien, J.-P. Rousseau, Y. Liu, A. Houard, P. Ramirez, D. Papadopoulos, A. Pellegrina, P. Georges, F. Druon, N. Forget, and R. Lopez-Martens, "Energy-scalable temporal cleaning device for femtosecond laser pulses based on cross-polarized wave generation," *Rev. Sci. Instrum.*, vol. 84, no. 4, p. 043106, 2013.

[142] G. Tempea and T. Brabec, "Theory of self-focusing in a hollow waveguide," *Opt. Lett.*, vol. 23, pp. 762–764, May 1998.

[143] C. Vozzi, M. Nisoli, G. Sansone, S. Stagira, and S. De Silvestri, "Optimal spectral broadening in hollow-fiber compressor systems," *Applied Physics B*, vol. 80, pp. 285–289, Mar 2005.

[144] M. V. Ammosov, N. B. Delone, and V. P. Krainov, "Tunnel ionization of complex atoms and of atomic ions in an alternating electromagnetic field," *Sov. Phys. JETP*, vol. 64, pp. 1191–1194, Dec 1986.

[145] M. V. Ammosov, P. A. Golovinsky, I. Y. Kiyan, V. P. Krainov, and V. M. Ristic, "Tunneling ionization of atoms and atomic ions in an intense laser field with a nonhomogeneous space–time distribution," *J. Opt. Soc. Am. B*, vol. 9, pp. 1225–1230, Aug 1992.

[146] P. B. Corkum, "Plasma perspective on strong field multiphoton ionization," *Phys. Rev. Lett.*, vol. 71, pp. 1994–1997, Sep 1993.

[147] L. P. Ramirez, D. Papadopoulos, M. Hanna, A. Pellegrina, F. Friebel, P. Georges, and F. Druon, "Compact, simple, and robust cross polarized wave generation source of few-cycle, high-contrast pulses for seeding petawatt-class laser systems," *J. Opt. Soc. Am. B*, vol. 30, pp. 2607–2614, Oct 2013.

[148] E. A. J. Marcatili and R. A. Schmeltzer, "Hollow metallic and dielectric waveguides for long distance optical transmission and lasers," *The Bell System Technical Journal*, vol. 43, pp. 1783–1809, July 1964.

[149] R. K. Nubling and J. A. Harrington, "Launch conditions and mode coupling in hollow-glass waveguides," *Opt. Eng.*, vol. 37, no. 9, pp. 2454–2458, 1998.

[150] M. Mohebbi, "Transmission characteristics of femtosecond optical pulses in hollow-core fibers," *Opt. Commun.*, vol. 253, no. 4, pp. 290 – 300, 2005.

[151] D. N. Schimpf, T. Eidam, E. Seise, S. Hädrich, J. Limpert, and A. Tünnermann, "Circular versus linear polarization in laser-amplifiers with Kerr-nonlinearity," *Opt. Express*, vol. 17, pp. 18774–18781, Oct 2009.

[152] X. Chen, A. Jullien, A. Malvache, L. Canova, A. Borot, A. Trisorio, C. G. Durfee, and R. Lopez-Martens, "Generation of 4.3 fs, 1 mj laser pulses via compression of circularly polarized pulses in a gas-filled hollow-core fiber," *Opt. Lett.*, vol. 34, pp. 1588–1590, May 2009.

[153] A. Husakou, *Nonlinear phenomena of ultrabroadband radiation in photonic crystal fibers and hollow waveguides*. PhD thesis, Freie Universität Berlin, Kaiserswerther Str. 16-18, 14195 Berlin, Germany, 2002.

[154] S. Petit, A. Talebpour, A. Proulx, and S. Chin, "Polarization dependence of the propagation of intense laser pulses in air," *Opt. Commun.*, vol. 175, no. 4, pp. 323 – 327, 2000.

[155] F. Böhle, M. Kretschmar, A. Jullien, M. Kovacs, M. Miranda, R. Romero, H. Crespo, U. Morgner, P. Simon, R. Lopez-Martens, and T. Nagy, "Compression of CEP-stable multi-mJ laser pulses down to 4 fs in long hollow fibers," *Laser Phys. Lett.*, vol. 11, no. 9, p. 095401, 2014.

[156] M. Nurhuda, A. Suda, K. Midorikawa, M. Hatayama, and K. Nagasaka, "Propagation dynamics of femtosecond laser pulses in a hollow fiber filled with argon: constant gas pressure versus differential gas pressure," *J. Opt. Soc. Am. B*, vol. 20, pp. 2002–2011, Sep 2003.

[157] J. Robinson, C. Haworth, H. Teng, R. Smith, J. Marangos, and J. Tisch, "The generation of intense, transform-limited laser pulses with tunable duration from 6 to 30 fs in a differentially pumped hollow fibre," *Appl. Phys. B*, vol. 85, pp. 525–529, Dec 2006.

[158] C. Bree, A. Demircan, and G. Steinmeyer, "Method for Computing the Nonlinear Refractive Index via Keldysh Theory," *IEEE J. Quantum Electron.*, vol. 46, pp. 433–437, Apr 2010.

[159] J. K. Wahlstrand, Y.-H. Cheng, and H. M. Milchberg, "High Field Optical Nonlinearity and the Kramers-Kronig Relations," *Phys. Rev. Lett.*, vol. 109, p. 113904, Sep 2012.

[160] F. A. Cotton, G. Wilkinson, C. A. Murillo, and M. Bochmann, *Advanced Inorganic Chemistry*. Wiley-Interscience, 6th ed., 1999.

[161] A. Börzsönyi, Z. Heiner, A. Kovács, M. P. Kalashnikov, and K. Osvay, "Measurement of pressure dependent nonlinear refractive index of inert gases," *Opt. Express*, vol. 18, pp. 25847–25854, Dec 2010.

[162] D. Wang, Y. Leng, and Z. Xu, "Measurement of nonlinear refractive index coefficient of inert gases with hollow-core fiber," *Appl. Phys. B*, vol. 111, pp. 447–452, May 2013.

[163] R. C. Jones, "A New Calculus for the Treatment of Optical SystemsI. Description and Discussion of the Calculus," *J. Opt. Soc. Am.*, vol. 31, pp. 488–493, Jul 1941.

List of publications

Articles:

1. N. Khodakovskiy, M. Kalashnikov, E. Gontier, F. Falcoz, and P.-M. Paul, "Degradation of picosecond temporal contrast of Ti:sapphire lasers with coherent pedestals," *Optics Letters*, vol. 41, pp. 4441–4444, Oct 2016

2. N. G. Khodakovskiy, M. P. Kalashnikov, V. Pajer, A. Blumenstein, P. Simon, M. M. Toktamis, M. Lozano, B. Mercier, Z. Cheng, T. Nagy, and R. Lopez-Martens, "Generation of few-cycle laser pulses with high temporal contrast via nonlinear elliptical polarisation rotation in a hollow fibre compressor," *Laser Physics Letters*, vol. 16, p. 095001, Aug 2019

Conferences (presented by the author):

1. M. P. Kalashnikov and N. Khodakovskiy, "Investigation of a Picosecond Pedestal of Recompressed CPA Pulses," in *International Conference on Ultrahigh Intensity Lasers (ICUIL)*, (Goa, India), October 2014

2. N. Khodakovskiy and M. P. Kalashnikov, "Picosecond Contrast of Recompressed CPA Pulses," in *CLEO/Europe 2015*, (Munich, Germany), June 2015

3. N. Khodakovskiy and M. P. Kalashnikov, "Investigation of a Picosecond Pedestal of Recompressed CPA Pulses," in *4th DoKDoK, doctoral conference on optics*, (Eisenach, Germany), October 2015

4. M. P. Kalashnikov and N. Khodakovskiy, "Picosecond Contrast in Ti:sapphire CPA Laser Systems," in *ICONO/LAT 2016*, (Minsk, Belarus), September 2016

5. N. Khodakovskiy, M. Kalashnikov, A. Blumenstein, P. Simon, T. Nagy, M. M. Toktamis, M. Lozano, B. Mercier, and R. Lopez-Martens, "Generation of high-contrast few-cycle pulses via nonlinear ellipse rotation in a differentially pumped hollow-fiber," in *International Conference on Ultrahigh Intensity Lasers (ICUIL)*, (Lindau, Germany), September 2018

Conferences (presented by co-authors):

1. M. P. Kalashnikov and N. Khodakovskiy, "Picosecond pedestals of recompressed Ti:Sapphire laser pulses," in *The 6th Advanced Lasers and Photon Sources (ALPS'17)*, (Yokohama, Japan), pp. ALPS5–4, April 2017

2. M. P. Kalashnikov and N. Khodakovskiy, "Picosecond temporal contrast of Ti:Sapphire lasers (Conference Presentation)," in *SPIE Optics+Optoelectronics*, p. 10238, June 2017

3. M. P. Kalashnikov and N. Khodakovskiy, "Picosecond Contrast of Recompressed Ti:Sapphire Laser Pulses," in *Conference on Lasers and Electro-Optics*, p. STu1O.6, Optical Society of America, May 2017

4. N. Khodakovskiy, M. Kalashnikov, A. Blumenstein, P. Simon, T. Nagy, M. M. Toktamis, M. Lozano, B. Mercier, and R. Lopez-Martens, "Generation of high-fidelity few-cycle pulses via nonlinear ellipse rotation in a stretched hollow-fiber compressor," in *Conference on Lasers and Electro-Optics*, p. SM1N.8, Optical Society of America, May 2018

Eidesstattliche Erklärung

Ich versichere hiermit an Eides Statt, dass diese Arbeit von niemand anderem als meiner Person verfasst worden ist. Alle verwendeten Hilfsmittel wie Berichte, Bücher, Internetseiten oder ähnliches sind im Literaturverzeichnis angegeben, Zitate aus fremden Arbeiten sind als solche kenntlich gemacht. Die Arbeit wurde bisher in gleicher oder ähnlicher Form keiner anderen Prüfungskommission vorgelegt und auch nicht veröffentlicht.

Berlin, February 13, 2020 Nikita Khodakovskiy

Abstract

The temporal contrast of optical pulses produced by high-peak power laser systems is important for laser-matter applications, such as table-top particle accelerators and sources of attosecond pulses in the extreme ultraviolet and X-ray ranges. Currently available laser technologies cannot provide a temporal shape of an ultra-short pulse at high energy which is absolutely pre-pulse free. This work is dedicated to issues of the temporal shape of light pulses generated by Chirped Pulse Amplification (CPA) lasers based on the widely-used Ti:Sapphire technology. This analysis is performed at the low picoseconds time scale around the main pulse and in a dynamic range of intensity $> 10^{10}$. An overview of the current state of the problem is presented as well as a detailed discussion of the many related aspects including the characterization of laser pulses over a high dynamic range and the technologies for nonlinear temporal filtering that are required for the suppression of pre-pulses and improvement of the leading front of the laser pulse.

The most commonly used diagnostics for characterization of laser pulses over a high dynamic range, including third-order cross-correlators, have been considered in detail. It has been shown that this method can introduce artefacts into the measured traces. An improvement to the optical scheme of the commercial Sequoia cross-correlator has been suggested. A method to indicate coherent parts of laser pulses has also been proposed.

Commonly used schemes for optical stretchers and compressors with different dispersive optics have been compared and investigated. It was shown and proved, for the first time that the nonlinear processes occurring during propagation of a stretched pulse result in the generation of a ragged pre-pedestal from the post-pedestal which is coherent to the main pulse. The key role of the ragged post-pedestal as well as its coherence have also been highlighted for the first time in this work. An explanation for the observed phenomena is given. It has also been shown that the post-pedestal is the key limiting factor of the picosecond temporal contrast in CPA Ti:Sapphire-based laser technology.

Highly efficient nonlinear filtering technology based on rotation of the polarization ellipse in gases and a post-compression technique have been combined to to improve the temporal shape of laser pulses on the femtosecond and picosecond time scales.

Zusammenfassung

Der zeitliche Kontrast von Laserpulsen ist für viele Anwendungen mit Verwendung von intensiven Laser Pulsen bedeutsam. Mit gegenwärtig verfügbaren Technologien können keine Ultrakurzzeitpulse mit hoher Energie erzeugt werden, deren zeitliche Form frei von Vorpulsen ist. In dieser Arbeit wird die Problematik des zeitlichen Kontrastes von Lichtpulsen untersucht, welche von Lasern basierend auf der weit verbreiteten Ti:Saphir Technologie mit Chirped Pulse Amplification (CPA) erzeugt werden. Diese Untersuchung wird innerhalb des Picosekundenbereiches um den Hauptpuls und mit einem Dynamikbereich von $> 10^{10}$ durchgeführt. Es wird ein Überblick über den gegenwärtigen Stand der Problematik gegeben, sowie eine detaillierte Diskussion von vielen verwandten Aspekten, einschließlich von Methoden zur Charakterisierung mit hohem Dynamikbereich und zeitlich nicht-linearen Filtern, welche zur Unterdrückung von Vorpulsen und der Verbesserung der führenden Flanke des Laserpulses notwendig sind.

Die am häufigsten verwendete Charakterisierungsmethode mit hohem Dynamikbereich durch Kreuzkorrelation in dritter Ordnung wurde im Detail betrachtet. Es wurde gezeigt, dass Charakterisierung mit hohem Dynamikbereich zu "Artefakten" in den Messkurven führen kann. Eine Verbesserung des optischen Aufbaus von "Sequoia" Kreuzkorrelatoren wurde vorgeschlagen. Ebenso wurde eine Technik zur Identifizierung kohärenter Anteile in Laserpulsen vorgestellt.

Schemata von Aufweitern und Kompressoren mit unterschiedlichen dispersiven Optiken wurden verglichen und untersucht. Erstmalig wurde gezeigt, dass die nichtlinearen Prozesse, welche während der Propagierung eines gestreckten Impulses entstehen, einen struckturierten Vorsockel aus dem Nachsockel generieren, der kohärent zum Hauptimpuls ist. Die Schlüsselrolle des strukturierten Nachsockels sowie seiner Kohärenz wurden in dieser Arbeit zum ersten Mal aufgezeigt. Eine Erklärung der beobachteten Erscheinungen wird präsentiert. Es wurde ebenfalls gezeigt, dass der Nachsockel ein Schlüsselfaktor in der Begrenzung des zeitlichen Kontrastes im Pikosekundenbereich von CPA Ti:Saphir basierter Lasertechnologie ist.

Hocheffiziente nicht-lineare Filtertechnologie basierend auf einer Drehung der Polarisation in Gasen und eine Nachkompressionstechnik wurden kombiniert um die Pulsdauer auf wenige optische Zyklen zu verringern und den zeitlichen Verlauf der Laserpulse zu verbessern.